



UNIVERSITÀ DEGLI STUDI DI PADOVA

Sede Amministrativa: Università degli Studi di Padova

Dipartimento di Fisica

SCUOLA DI DOTTORATO DI RICERCA IN: SCIENZA ED INGEGNERIA DEI
MATERIALI

CICLO XXI

Capillary condensation in nanostructured surfaces

Direttore della scuola: Prof. Gaetano Granozzi

Supervisore: Prof. Giampaolo Mistura

Co-Supervisore: Dr. Massimo Tormen

Dottorando: Alessandro Pozzato

Abstract

The subject of this thesis is the study of the capillary condensation phenomenon in nanostructured surfaces. The main motivation behind this work was to test recent scaling theories about the capillary filling in capped capillaries. Adsorption isotherms of Argon were measured at a temperature slightly above its triple-point with a torsional microbalance. A key element for this kind of experiments was the availability of surfaces patterned with an array of very regular structures (e.g. rectangular wells or cylindrical holes). To fabricate these substrates was fundamental to develop a new fabrication methodology based on advanced lithographic techniques. The optimized methodology relied on nanoimprint lithography (NIL), wet etching (Buffered Oxide Etch solution) and plasma etching in an Inductively Coupled Plasma (ICP). With our process we were able to pattern extended surface areas of about 1 cm^2 with a regular array of rectangular channels or hemispherical holes of nanometric size. In particular, we realized channels of two different widths (90 and 200 nm) and characteristic depths varying from 0.5 to 2 μm . Adsorption isotherms taken with these samples showed sharp and reversible jumps related to the capillary condensation of liquid argon in the channels. Their location was found to vary with the channel width, wider channels displaying the transition closer to bulk liquid-vapor condensation. A quantitative analysis of these positions in terms of the classical Kelvin equations yielded results which were in good agreement with the sample morphology deduced by electron microscopy. The precise shape of the capillary rise is currently under investigation to check whether it confirms the scaling predictions. The fabrication of the samples has been realized in the TASC-INFM Laboratory in Trieste under the supervising of Dr. Massimo Tormen, whereas the measurement runs of adsorption isotherms were carried out in the laboratory of Prof. Giampaolo Mistura in Padova.

Sommario

Il tema di questa tesi è lo studio dello studio dei fenomeni di condensazione capillare in superfici nano strutturate. La motivazione principale a sostegno di questo lavoro è la verifica di recenti teorie che descrivono il riempimento di capillari chiusi ad una estremità. Le isoterme di assorbimento dell'argon sono state misurate a temperature leggermente superiori al suo punto triplo con l'uso di una micro bilancia torsionale. Un elemento chiave per questo tipo di esperimenti è la disponibilità di superfici strutturate con una distribuzione periodica di elementi regolari (ad esempio canali rettangolari o cavità cilindriche). Per costruire substrati di questo genere, è stato necessario sviluppare una metodologia fabbricativa innovativa, basata su tecniche di litografia avanzata. La metodologia ottimizzata si basa sulla cosiddetta nanoimprint lithography (NIL), su etching in ambiente liquido (uso di soluzioni BOE per l'etching di ossido di silicio) ed etching con uso di plasma gassosi in macchine di tipo ICP (Inductively Coupled Plasma). Con il nostro processo siamo in grado di strutturare superfici con area di estensione fino a 1 cm^2 con distribuzione regolare di canali a sezione rettangolare o cavità di forma emisferica, entrambi con dimensioni caratteristiche nel range dei nanometri. In particolare abbiamo realizzato canali di due differenti larghezze (90 e 200 nm) e profondità caratteristica variabile tra 0.5 e 2 μm . Isotherme di adsorbimento misurate con questo tipo di campioni mostrano transizioni nette e reversibili correlabili con la condensazione capillare di argon liquido. La posizione di queste transizioni varia col variare della larghezza dei canali: canali più larghi evidenziano una transizione più vicina alla condensazione liquido-vapore in fase bulk. L'analisi quantitativa di questi risultati, in termini della classica equazione di Kelvin, mostra previsioni in buon accordo con la caratterizzazione diretta dei campioni tramite immagini al SEM. La definizione precisa del profilo della parete del canale è ancora sotto analisi per la conferma delle previsioni teoriche. La fabbricazione dei campioni è stata condotta presso il laboratorio nazionale TASC-INFN in Trieste sotto la supervisione del Dr. Massimo Tormen, mentre la misurazione delle isoterme di adsorbimento è stata condotta nel laboratorio del Prof. Giampaolo Mistura all'Università di Padova.

*ai miei genitori
mamma Rosi e papà Luigi*

Contents

1	Introduction	1
2	Introduction to the wetting	3
2.1	Wetting transition	3
2.2	Wetting on structured surfaces	7
2.3	Capillary condensation	10
3	Thermal Nanoimprint Lithography	15
3.1	Introduction to Nanoimprint Lithography	15
3.2	Stamp	20
3.3	Resist	28
3.4	Polymer flow and imprint process	31
4	The plasma etching process	37
4.1	Gas Discharge Plasmas	37
4.2	Dry-Etching Processes	46
5	Fabrication of the samples	53
5.1	Rectangular channels with a period of 4 micron	53
5.2	Rectangular channels with a period of 500 nm and 180 nm	59
6	Experimental results	73
6.1	The experimental setup	73
6.2	Data analysis	76
7	Conclusions and perspectives	85
A	Curriculum vitae	91
	Bibliography	95

Acronyms

CC	capillary condensation
EBL	electron beam lithography
ICP	inductively coupled plasma
NIL	nanoimprint lithography
PL	Photolithography
PMMA	poly-methylmethacrylate
RIE	reactive ion etching
SAM	self-assembled monolayer
SEM	scanning electron microscope
T_g	glass transition temperature

Chapter 1

Introduction

It is well known that the geometry of the substrate strongly affects the growth of an adsorbed film. This problem has been studied for many years both for its technological applications and for its interest in the statistical mechanics of the interfaces. Recent progresses in the fabrication of micropatterned substrates for microfluidic applications have stimulated the study of fluid adsorption at tailored surfaces. The study of the wetting behavior of liquid films in wedges has shown a rich variety of novel phase transitions that are extremely sensitive to the shape of the confining geometry [1, 2], some of those were also observed in adsorption experiments [3, 4].

In particular, it was found that complete wetting of substrates patterned by periodic arrays of rectangular wells and quadratic lattices of cylindrical pits, both of same depths, exhibits a new example of geometrical covariance [1]. It was also predicted that capillary condensation in a rectangular well is a continuous critical phenomenon exhibiting observable critical singularities which are intimately related to several other surface phase transitions [5]. These theoretical predictions should be verifiable in adsorption experiments that employ a torsional microbalance to monitor the variation of the liquid mass condensed into regular arrays of nanochannels [6]. The experimental setup developed in the Laboratory of Surface and Interface Physics at Padua University has been optimized to measure samples with a patterned surface area of about 1 cm^2 . It was therefore necessary to employ high throughput lithographic techniques which allowed to pattern extended areas. The substrates used in this Ph.D. thesis have been produced by the optimization of a fabrication methodology based on UV-lithography, thermal nanoimprint lithography and plasma dry etching. The resulting sample surfaces were patterned with rectangular wells (i.e. capped capillaries) characterized by a width of $1.6 \mu\text{m}$, 200 nm and 90 nm . The uniformity of the channels dimension and their quality (i.e. roughness of the surfaces, slope of the walls) were some of the key issues in the fabrication process.

Adsorption isotherms taken with these samples showed sharp and reversible jumps related to the capillary condensation of liquid argon in the channels. Their location

was found to vary with the channel width, wider channels displaying the transition closer to bulk liquid-vapor condensation. A quantitative analysis of these positions in terms of the classical Kelvin equations yielded results which were in good agreement with the sample morphology deduced by electron microscopy. The precise shape of the capillary rise is currently under investigation to check whether it confirms the scaling predictions. This thesis is organized as follows: the first chapter shows a brief introduction to the wetting phenomenology and an overview of recent scaling theories about the influence of a regular pattern on the film growth, specifically the case of rectangular wells and cylindrical pits; the lithography techniques used for the substrate patterning will be outlined in chapters 3-4 . The substrate fabrication and the measurement of adsorption isotherms with the torsional microbalance will be described in detail in chapters 5-6 respectively. Finally, the data analysis of the measured adsorption isotherms will be presented in chapter 7.

Chapter 2

Introduction to the wetting

The study of wetting phenomena on surfaces is important for the design and fabrication of many innovative and advanced systems, like extended superhydrophobic areas (e.g. antifouling glasses) or micro and nanofluidic devices (e.g. micro reactors for chemical reactions). The first studies about wetting have been realized by Young in the 1805 [7]. Cahn's prediction in the 1977 of the wetting transition was a landmark study which stimulated many works in this field until now.

More recently, the studies about the influence of roughness on the adsorption of gas and liquid on planar surfaces were a starting point for understanding the role of a regular patterning on the substrate. The advances in the statistical mechanical theory and computer simulation of fluid interfaces, allowed to formulate new theories regarding the wetting and capillary condensation in structures with micrometric and nanometric size, showing a rich microscopic behavior of the confined gas or liquid closely connected to the size and geometry of the structures on the substrate.

This chapter briefly introduces the wetting phenomena with a particular attention to the wetting transition on planar solid substrate which is fundamental to understand the wetting behavior of structured surface and specifically the condensation in capped capillaries, which is the subject of this thesis.

2.1 Wetting transition

Let us consider a collection of N identical atoms enclosed in a box of volume W [8]. The box is maintained at a temperature T and chemical potential μ . For the sake of simplicity, the box walls are considered inert, i.e. unaffected by any thermodynamical change of the surrounding environment. Each atoms interacts with the surface via a potential $U(z)$, where z is the distance atom-surface, and with other atoms via a potential $V(r)$, where r indicates the interatomic separation. For rare gasses, $V(r)$ is

generally assumed to be a *Lennard-Jones potential* of the form:

$$V(r) = v \left[\left(\frac{\sigma}{r} \right)^{12} - \left(\frac{\sigma}{r} \right)^6 \right] \quad (2.1)$$

where σ is the atomic radius and v is the strength of the potential.

The corresponding atom-substrate potential is usually assumed to be of the van der Waals form:

$$U(z) \equiv uf(z) = \frac{4C_3^3}{27D^2z^9} - \frac{C_3}{z^3} \quad (2.2)$$

Where D is the well depth and C_3 is the coefficient of the van der Waals tail and u is the strength of the potential that coincides with C_3 for large z .

Because of the van der Waals attraction, a film may cover the surface of the walls. When the film is in equilibrium with the surrounding vapour, its thickness d depends only on μ and T for a given combination surface/adsorbate. Let us imagine to keep T constant and to slowly increase μ to its saturated value μ_0 . The film thickness can behave in two different ways: either d remains finite at saturation (*incomplete wetting*) or it can continuously increase as μ is brought towards μ_0 (*complete wetting*). An extreme case of incomplete wetting is when no film covers the surface, e.g. $d = 0$. Incomplete wetting is usually observed at low temperatures, for example below the adsorbate triple point. At higher temperatures the film generally completely wets a surface. The transition between these two growth modes is called *wetting transition*.

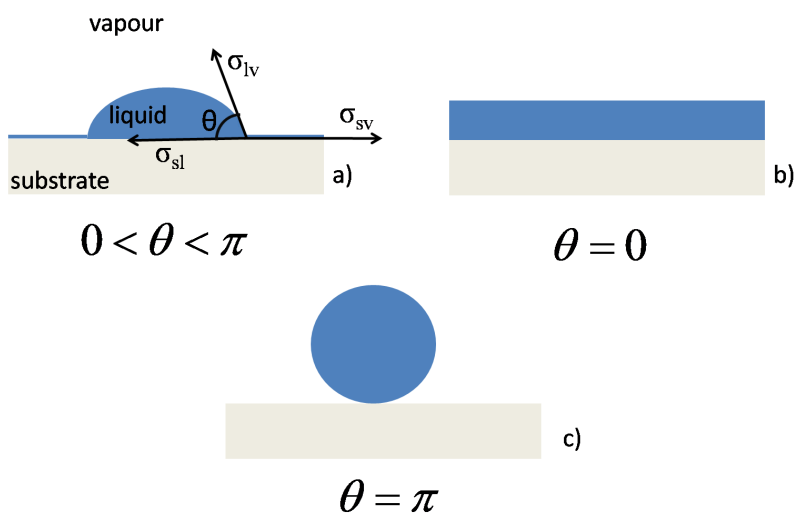


Figure 2.1: Contact angle and wetting classification. In the non-wet case (A) a microscopic film covers that part of the substrate not beneath the drop. For a dry substrate this thin layer is missing [8].

The driving mechanism of such a transition is best understood in terms of the

Young's equation. A saturated film that incompletely wets the surface can be visualized as a droplet (a crystallite below T_t) on top of a microscopic film a few layers thick (see Fig. 2.1). Mechanical equilibrium requires (Young's equation):

$$\sigma_{sv} = \sigma_{sl} + \sigma_{lv} \cos\theta \quad (2.3)$$

where θ is the contact angle and σ_{ij} is the surface tension at the ij interface. The contact angle permits a simple classification of the wetting phenomenology: for $\theta = 0$ the substrate is said to be completely wet by the adsorbate and for $\theta < \pi$ incompletely wet. The angle θ may vary owing to a change in the chemical composition of the droplet and/or a temperature variation. It is a well known fact that, in approaching the liquid-vapour critical point T_c , the difference between the liquid and the vapour phase disappears and so does σ_{lv} . Sufficiently near T_c , one finds:

$$\sigma_{lv} \approx \left(\frac{T_c - T}{T_c} \right)^\mu \equiv t^\mu \quad (2.4)$$

Where the critical exponent μ is equal to ≈ 1.26 ($\mu = 3/2$ in the mean field theory) and t is the reduced temperature.

In 1977 Cahn [9] conjectured that, in approaching T_c , the difference $|\sigma_{sv} - \sigma_{sl}|$ vanishes as the difference $\rho_l - \rho_v$ in bulk densities and therefore scale as t^β , with $\beta = 0.32$ ($1/2$ in mean field). This implies $\cos\theta \sim t^{\beta-\mu}$, which diverges near the critical point in contradiction to $|\cos\theta| \leq 1$. Cahn concluded that if a liquid film incompletely wets a surface at low temperatures, it must undergo a wetting transition as the temperature is raised towards T_c so that $\theta > 0$ for $T < T_w$ and $\theta = 0$ for $T \geq T_w$.

This transition can be either continuous or first order. In the former case, also known as critical wetting, adsorption isotherms measured at different temperatures below T_w have the shape schematically shown in Figs. 2.2(a)-(b). If the $\mu - T$ plane is cut along a path of constant $\mu = \mu_0$, the coverage d will continuously increase as T_w is approached from below (see Figs. 2.2(c)-(d)). A similar thermodynamic path taken across a first-order wetting point is shown in Figs. 2.2(g)-(h). In this case, d jumps from a finite value at T_w^- to a macroscopic value (ideally infinite) at T_w^+ . Away from coexistence, this jump becomes finite (see Fig. 2.2(h)). The wetting point is the beginning of a first-order line called the prewetting line which separates the thin-film from the thick-film regions. Isothermal paths cutting across this line are shown in Figs. 2.2(e)-(f). The prewetting line ends at a prewetting critical point where the distinction between thin film and thick film disappears.

The order of the wetting transition depends on the strength and the range of the film interactions in a very subtle way. In 1982, Pandit et al. [10] studied a lattice gas model in which adatoms occupy the sites of a cubic lattice spanning the half-space $z > 0$ and have a nearest neighbour attraction v . The substrate attracts the adatoms sitting in the

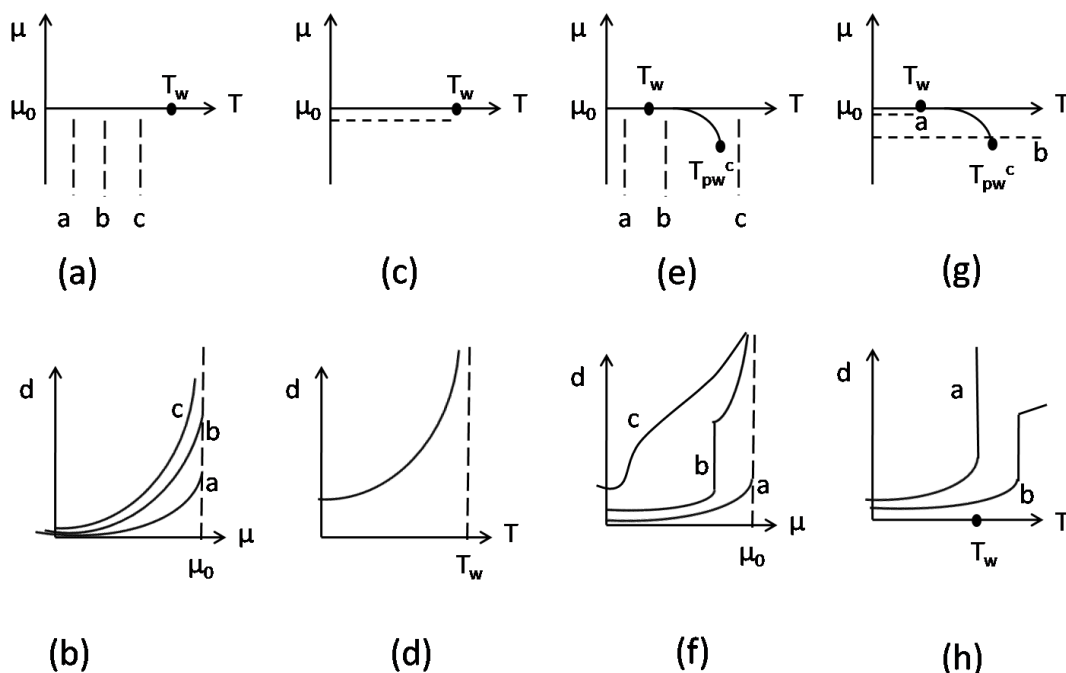


Figure 2.2: The film coverage along several typical thermodynamical paths. The axis $\mu = \mu_0$ is the bulk liquid-vapour coexistence line. The cases (a)-(d) correspond to a continuous wetting transition. The other ones represent a 1st order prewetting line [8].

first layer next to the substrate with a constant potential u . The mean field numerical analysis of such a model shows that the whole wetting phenomenology of Figs. 2.1 can be reproduced by simply varying the ratio u/v . For $u/v > 1$, the substrate is so strong that $T_w = 0$. In the intermediate case $0.7 \leq u/v \leq 0.9$, the wetting transition is first order. If the substrate is further weakened, T_w increases towards T_c and one has critical wetting for $0.5 < u/v < 0.7$. In the range $0 \leq u/v < 0.5$ the corresponding drying transition occurs. Numerical analysis of model with potential U and V which decay exponentially exhibit a similar wide variety of different wetting behaviours. The particular results, however, are very sensitive to the details of the potentials and approximations employed. First order wetting is instead very common in systems with long-range interactions which decay according to a power law, although it is possible, by accurate selection of the parameters, to observe critical wetting.

For a temperature fixed between the wetting temperature and the critical temperature of the coexistence liquid-vapor ($T_w < T < T_c$) the liquid wets the substrate and forms a molecularly thick layer. The increasing of the pressure towards coexistence, or as well, the increasing of the chemical potential towards coexistence value (μ_0) produces a monotonous growth of the layer thickness (see Fig. 2.3a). Theoretical predictions, confirmed by several experiments, have shown that the thickness l_π of the adsorbed layer diverges when it approaches coexistence with a non-universal exponent β_{co} which is dependent on physical interactions (e.g. for non-retarded van der Waals

forces, $\beta_{co} = \frac{1}{3}$) of the adsorbed particles (solid-fluid and fluid-fluid) involved in the system, where:

$$l_\pi \approx |\Delta\mu|^{-\beta_{co}} \quad (2.5)$$

$$\Delta\mu = \mu - \mu_{co}$$

The $\Delta\mu$ for dilute gasses is related to the partial pressure by the following:

$$\Delta\mu = k_B T \log \left(\frac{p}{p_{co}(T)} \right) \quad (2.6)$$

where k_B is the Boltzmann's constant, T is the temperature and P_0 is the coexistence pressure.

The prediction of the film growth 2.5 has been developed for planar and homogeneous solid substrates; however, in most experimental and technological situations the substrate is both rough and inhomogeneous. For this reason the influence of substrate roughness and chemical disorder has been investigated theoretically [11] and experimentally.

Approaching coexistence, the heterogeneity and roughness of the solid substrate in conjunction with long-range van der Waals interactions cause equilibrium undulations of the surface of the growing liquid film and the surface tension reduces the amplitude of undulations for thicker films. If a flat substrate is not covered with a macroscopic liquid layer as coexistence is approached, a roughness above a certain threshold allows, for the same substrate and temperature, the complete coverage of the surface. Moreover, the roughness-induced wetting disappears for very large amplitudes of the roughness [12, 11].

2.2 Wetting on structured surfaces

After the studies about the role of roughness on the wetting behavior of a surface, Rascón and Parry [2] presented a theoretical model which showed that the shape of a channel can exert a profound influence on the adsorption isotherms of liquid, allowing the possibility of tailoring the adsorption properties of solid substrates by sculpting their surface shape.

One of the simplest geometrical configurations beyond the planar wall is a parallel slit geometry comprising two planar substrates at distance L from each other. For this system, a different phenomenon occurs called capillary condensation. By increasing the chemical potential at a constant temperature $T > T_w$, the thickness of the adsorbed liquid layers on either wall grows according to a law similar to that for the planar system. However, when the chemical potential reaches a certain value $\Delta\mu^* < 0$, the space between the walls fills up with liquid, even though that phase is not thermodynamically

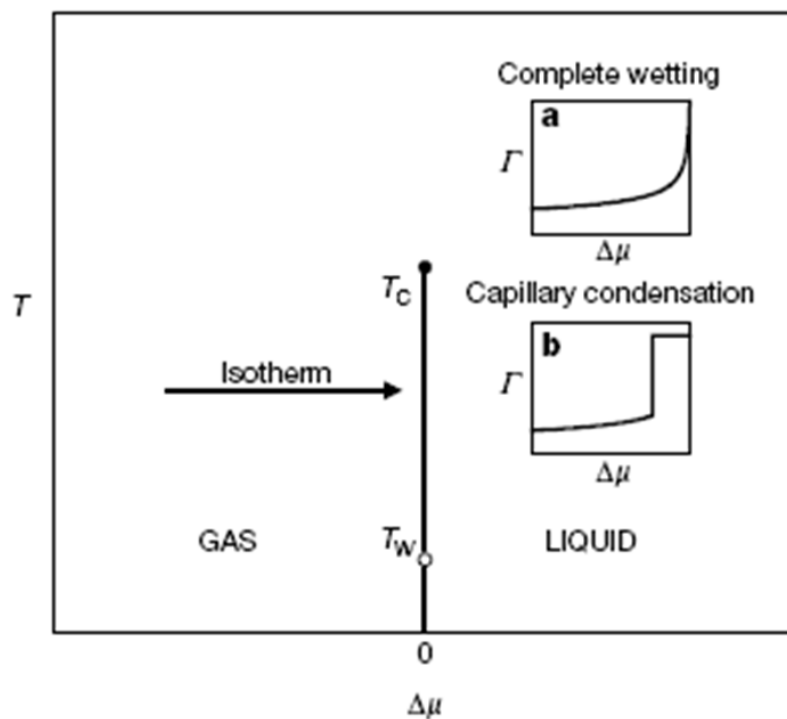


Figure 2.3: Schematic bulk phase diagram of a fluid showing the coexistence between gas and liquid phase. The gas phase is placed in contact with a solid substrate at a temperature between the critical temperature T_c and the wetting temperature T_w . As we approach coexistence, a liquid layer of increasing thickness is adsorbed on the substrate. Insets, adsorption isotherms are sketched for a planar substrate (a) and for a parallel slit (b) [2]

stable in bulk. The location of this first-order phase transition is given, for sufficiently large values of L , by the Kelvin's equation:

$$\Delta\mu^* = -\frac{2\sigma}{(\rho_L - \rho_G)L} \quad (2.7)$$

where ρ_L and ρ_G are the densities of the liquid and the gas respectively and σ is the surface tension between these phases.

This simple comparison reveals the influence of geometry on adsorption isotherms: the continuous divergence dominated by the microscopic details of the interaction with the substrate, embodied in the exponent β_{co} , in the case of a planar wall, is transformed into a discontinuous jump at a value of the chemical potential $\Delta\mu^*$ in the case of the slit (see Fig. 2.3).

Although the full phenomenology of wetting is best understood with the help of effective interfacial models, capillarity condensation is more effectively described by density functional methods. Rascón and Parry showed, with a purely geometrical model, that there is a wealth of adsorption phenomena induced by different wall geometries, which smoothly interpolates between wetting and capillary condensation [2]. The model, which is exact in the macroscopic limit, is not intended to be a microscopic description of these phenomena; instead, it should capture the essential features of geometrically dominated adsorption, which, owing to the lack of adequate models, remains largely unexplored.

In their model, a wide range of geometries has been investigated using a shape function 2.8 which describes the cross-section of generalized solid wedges. The function is developed in the x direction and L is a length associated with the dimensions of the wall.

$$\Psi(x) = \frac{|x|^\gamma}{L^\gamma - 1} \quad (2.8)$$

where the exponent γ is comprised from 0 and $+\infty$. The case $\gamma = 0$ corresponds to the case of a planar surface and $\gamma = +\infty$ represents a capillary slit formed by two parallel planar surfaces at distance L from each other. Others particular intermediate cases are the linear ($\gamma = 1$) and parabolic ($\gamma = 2$) wedges as shown in Fig. 2.4. The model shows the existence of different regimes in the adsorption isotherms varying the parameter γ (i.e. the shape of structures cross-section) when $\Delta\mu \rightarrow 0$:

- a planar regime PL , for $\gamma < \gamma^*$;
- a first geometrically dominated regime (G_1), for $\gamma^* < \gamma < 1$;
- a second geometrically dominated regime (G_2), for $\gamma > 1$;
- an intermediate regime (GP) between the planar regime and a geometrically dominated regime.

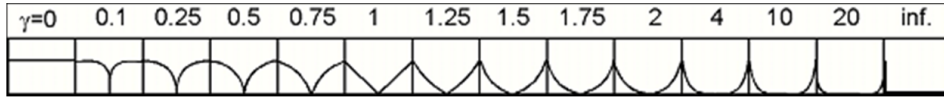


Figure 2.4: The evolution of the cross-section with the parameter γ ranging from planar wall ($\gamma = 0$) to a capillary slit ($\gamma = \infty$) [2].

If the system is in the PL regime, the wetting is due to interaction forces between adsorbate-adsorbate and between adsorbate-substrate; β_{co} , as just seen, is the exponent for the wetting on planar surfaces.

$$\gamma^* \equiv \frac{2\beta_{co}}{1 + \beta_{co}} \quad (2.9)$$

and the thickness of the adsorbed layer grows as l_π with the exponent β_{co} :

$$l_0 \approx l_\pi \approx |\Delta\mu|^{-\beta_{co}} \quad (2.10)$$

In the case of the system is in G_1 regime, the growth of the layer thickness is characterized by a divergence that depends only on the shape of the channel through the formula:

$$l_0 \approx |\Delta\mu|^{-\frac{\gamma}{2-\gamma}} \quad (2.11)$$

Instead, if we have the G_2 regime, the thickness of the growing layer diverges according to the formula:

$$l_0 \approx |\Delta\mu|^{-\gamma} \quad (2.12)$$

Therefore, it is clear that the shape and the dimension of the structures present on the surface have an important role in the growth of the adsorbed film. Experimental studies carried out with surfaces nanostructured with curved microscopic channels [4] or linear wedge [6, 3] essentially confirmed some of these predictions.

2.3 Capillary condensation

The limit $\gamma = +\infty$ of the previous model corresponds to a rectangular well. Adsorption in such a geometry is characterized by the phenomenon of capillary condensation (CC). This is central to understand the confined fluids and has received much attention over the last few decades [5]. As is well known, vapour confined in a slit of width L condenses at a pressure $p_{co}(L)$, less than the value p_{sat} at bulk saturation, given by the

macroscopic *Kelvin's equation*:

$$p_{sat} - p_{co}(L) = \frac{2\sigma \cos\theta}{L} + \dots \quad (2.13)$$

where σ is the liquid-vapour surface tension and θ the contact angle.

Studies of *CC*, based on Landau or modern density functional methods, usually consider confining walls of infinite area and assume translational invariance parallel to these. In this case, *CC* is certainly a first order transition and mean-field treatments yield adsorption isotherms with a van der Waals loop.

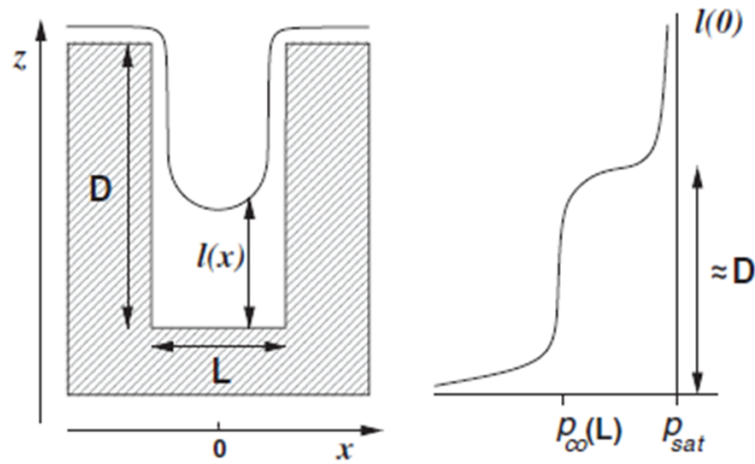


Figure 2.5: Schematic cross section (left) of a capped capillary of depth D and width L that shows the local interfacial height $l(x)$. The capped slit is infinitely long in the y direction. A typical adsorption isotherm is sketched (right) showing the rapid but continuous rise in the midpoint height near *CC* for $p \approx p_{co}(L)$ and the complete wetting as saturation is approached [5].

Far less attention has been given to *CC* in slits of finite-depth D which are capped at one end and open into a reservoir (see Fig. 2.5). Three numerical studies [13, 14, 1], restricted to complete wetting ($\theta = 0$), have reported the same basic finding that in a finite capillary, *CC* is a sharp but continuous transition (Fig. 2.5) and adsorption isotherms do not exhibit van der Waals loops for any finite D . However, the physical reason behind this striking change and the quantitative aspects of the transition have not been elucidated.

CC in such capped capillaries is a continuous interfacial critical phenomenon that exhibits observable critical singularities. For instance, in three dimensions, adsorption and desorption in a deep capillary correspond to the continuous unbinding of the meniscus from the bottom and top, respectively, and map onto two-dimensional complete wetting with relevant scaling field $\Delta p = p_{co}(L) - p$. The divergence of the

average meniscus height on these branches is described by the respective critical singularities:

$$\langle l \rangle \sim \Delta p^{-\beta_A},$$

$$D - \langle l \rangle \sim |\Delta p|^{-\beta_D}$$

which are, in general distinct. In particular, for dispersion forces, $\beta_A = 1/4$ while $\beta_D = 1/3$ implying that the adsorption isotherm is steeper than the desorption. For a finite-depth capillary, the meniscus has large-scale fluctuations at $p = p_{co}$ equivalent to those of an interface in a 2D infinite capillary with opposing walls for which there are long-standing predictions.

Further, in a 2D capped slit (or a 3D capillary pore), CC can be related to the critical-wetting transition occurring at 2D planar substrates. This connection is an extension of the geometrical covariance known for the filling of wedges, cones and apexes and implies that some (universal) interfacial properties in very different geometries are identical. These relations of covariance imply that different confining potentials can lead to identical local interfacial properties once external fields are suitably rescaled.

For instance a geometrical covariance is predicted by Tasinkevych and Dietrich [1] in the case of complete wetting for substrates patterned by periodic arrays of rectangular grooves or quadratic lattice of cylindrical pits (see Fig. 2.6), both of depths D .

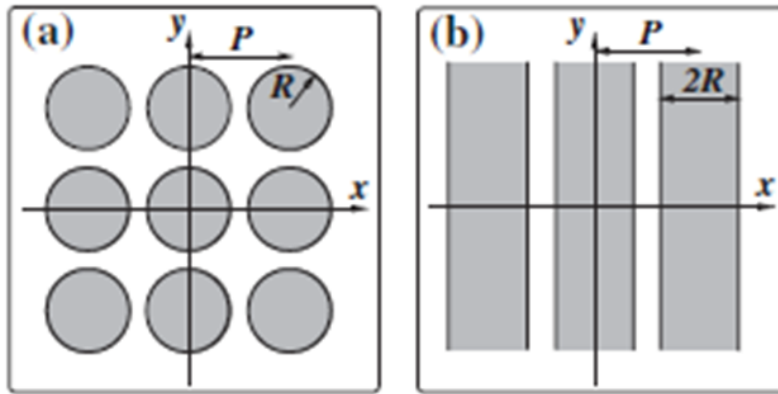


Figure 2.6: Substrates patterned with two different geometries. (a) Quadratic lattice of identical pits (cylinders or paraboloids). (b) Periodic array of grooves (rectangular or parabolic). All cavities have finite depths D [1].

As it is shown in the inset of Fig. 2.7, in such geometries and for D/R large enough, a continuous filling of the cavities takes place at

$$\Delta\mu = \Delta\mu_{fil}^{p,g} \quad (2.14)$$

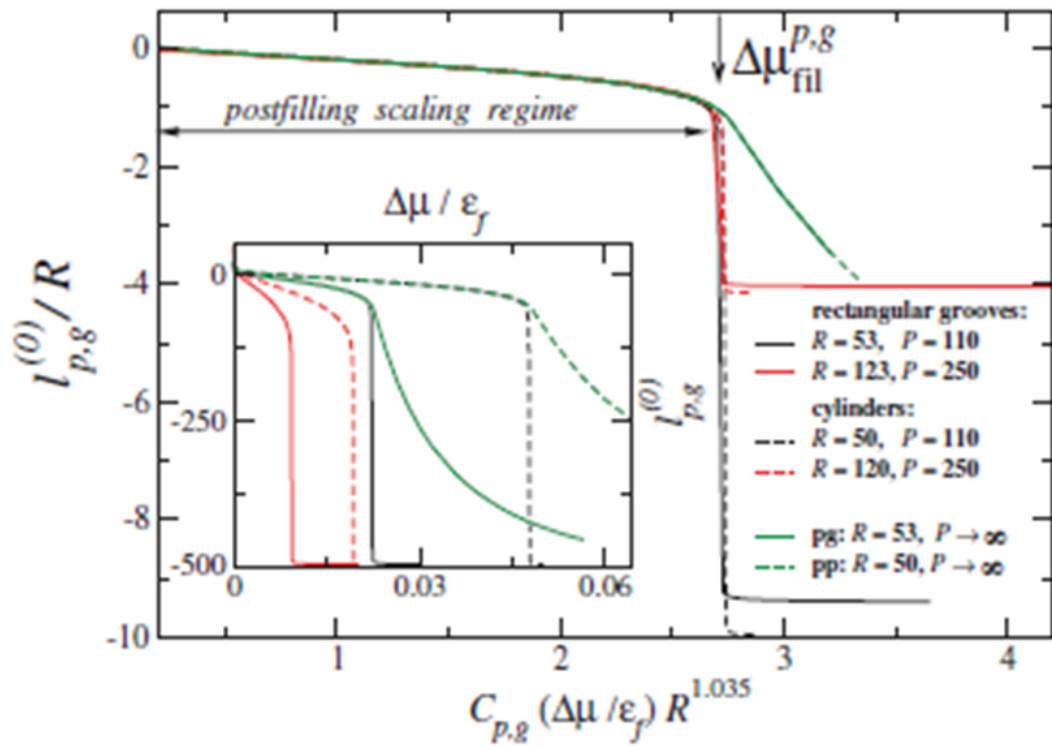


Figure 2.7: Typical interfacial heights $l_{p,g}^{(0)}$ (measured from the plane $z = 0$) at the middle of the cylindrical and parabolic pits, $l_p^{(0)}$ (dashed lines), and of the rectangular and parabolic grooves, $l_g^{(0)}$ (solid lines), as a function of $\Delta\mu$ with $C_p = 1$ and $C_g = 2$. The depth of the cavities is $D = 500 \text{ nm}$ and $pp(g)$ denotes parabolic pits (grooves). All lengths are measured in units of σ [1].

where the superscripts p, g are referred to pits and grooves respectively. The inset of Fig. 2.7 shows typical interfacial heights $l_{p,g}^0$ at the middle of the cylindrical and parabolic pits, l_p^0 , and of the rectangular and parabolic grooves, l_g^0 , as a function of $\Delta\mu$. If the isotherms for the grooves and pits are rescaled according to the equation:

$$l_{p,g}^0(\Delta\mu, R, P, D) = R\Lambda_{p,g} \left(\left(\frac{\Delta\mu}{\epsilon_f} \right) \left(\frac{R}{\sigma} \right)^{1+\delta} \right) \quad (2.15)$$

where ϵ_f is a molecular energy, σ is a length scale and $\Lambda_p(x) = \Lambda_g\left(\frac{x}{2}\right)$, the rescaled isotherms nicely collapse into a single curve as shown in the same Fig. 2.7, where $C_p = 1$ and $C_g = 2$.

These recent scaling theories and the condensation in capped capillaries have not been tested experimentally yet; the goal of this thesis is to test such theories by measuring of adsorption isotherms on substrates nanostructured with rectangular channels and cylindrical pores characterized by small width, less than 500 nm and a depth of at least 500 nm.

Chapter 3

Thermal Nanoimprint Lithography

3.1 Introduction to Nanoimprint Lithography

In the last two decades, a number of fabrication methods broadly referred to "nanotechnology" have been developed with the purpose of fabricating nanostructures in a variety of materials with control down to the nanometre scale and often to the atomic scale. These techniques are required to meet both the stringent nanofabrication specifications, ease of manufacturability and costs considerations of high-tech industries (e.g. electronic industry) as well as the flexibility and accessibility needed in experiments and investigations in materials science, organic optoelectronics, nano-optics and life sciences. Often techniques that offer striking performances on one specific aspect, are weak considered from other points of view. For instance, the scanning probe techniques (AFM, STM, MFM,...), which are employed in many research areas mainly for morphological studies but also as lithographic tools, are a clear example of the difficulty to combine high resolutions with a high throughput, moderate costs and user-friendly operation.

The emerging nanofabrication technique, which will be discussed in this chapter, have a combination of characteristics that makes it among the strongest candidates for the industrialization nanotech applications. Their classification depends on whether the nature of the patterning is chemical or physical, or its modality in time is parallel or sequential, or a hard or a soft stamp is used, etc. These techniques are micro-contact printing [15], nanoimprint-based lithography technique [16], dip pen lithography [17], nanoplotting [18], and stenceling [19].

In particular, this chapter deals with the technology named nanoimprint lithography; it is considered a cost-efficient parallel fabrication technique for nanostructuring with resolution down and below 10 *nm*, by which devices can be fabricated in single or multiple patterning steps [20]. The role of the components involved in the nanoimprint lithography (NIL) technique will be discussed such as stamp, polymer, anti-sticking coating. Further, the fluid mechanics will be outlined in order to describe the squeez-

ing flow of the polymer during the imprinting process.

A brief history of nanoimprint lithography

Different varieties of micromolding of thermoplastics, such as hot embossing or injection molding, which had been used for more than 30 years in industry [21], inspired the first article about thermal nanoimprint lithography published by Stephen Y. Chou et al. [22] in 1995. It outlined the essential elements of this technique, such as stamp manufacturing, process parameters, polymer flow, polymer adhesion and pattern transfer.

In the proof of principle, as stamp was employed a silicon substrate with a silicon dioxide layer patterned by electron beam lithography (EBL) and reactive ion etching (RIE). The pattern was an array of pillars with a diameter of 25 nm and a period of 120 nm. The stamp was imprinted at a pressure of ≈ 131 bar and a temperature of 200° C into a 55 nm thick poly-methylmethacrylate (PMMA) layer deposited on silicon. After system cooling below the glass transition temperature (T_g), the stamp and substrate were separated. The patterned PMMA was exposed to an oxygen plasma in RIE in order to remove the polymer residual layer in the holes imprinted by the pillars of the stamp uncovering the silicon beneath. 5 nm of titanium and 15 nm of gold was subsequently deposited on the surface followed by the lift off in acetone of the polymer. The resulting pattern was a uniform array of *Ti/Au* dots on the silicon substrate. The dots had the same dimension and period of the pillars array on the stamp as shown in Fig. 3.1.

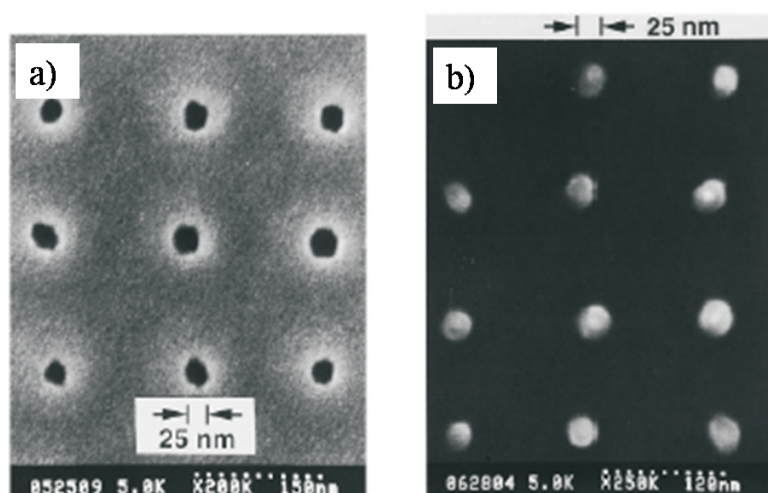


Figure 3.1: a) : SEM image of holes with a diameter $D = 25$ nm and a period $L = 120$ nm imprinted into PMMA. b) SEM image of dots fabricated by lift-off. [22].

After the first publications by Chou and collaborators others followed by several research groups coming from Wuppertal University (1998)[23], Wurzburg University

(1999)[24] and Micro Resist Technology (1999)[25] in Germany, CNRS in France (1999)[26], Seoul University (1999) in Korea[27], PSI in Switzerland (1999)[28] and Lund University in Sweden (1999)[29].

In 2003, the International Technology Roadmap for Semiconductor (ITRS) introduced NIL into semiconductor industry roadmap as "next generation lithography" candidate for the 32 nm node and beyond, scheduled for industrial manufacturing in 2013. The importance of nanoimprint has been recognized by the EU, that financed and coordinated the research in Europe in this field through projects as SPINUP project, Nanotech (Development of Nanoimprinting technique suitable for large area mass production of nm-scale patterns), which ran 1997-1999, CHANIL (CHances for NanoImprint Lithography), which ended in 2002 and NAPA (Emerging Nanopatterning Methods), which ran until 2008, followed by NaPanil, a project on nanopatterning, production and applications based on nanoimprinting lithography.

Nanoimprint is not exclusive domain of academic research, but given the large industrial interest has involved tools developers, stamps and polymers producers represented by companies such as Obducat in Sweden, Molecular Imprints and Nanonex in USA, Jenoptik and Micro Resist Technology in Germany, NIL Technology in Denmark and others.

Concept of Thermal Nanoimprint Lithography

In a recent review H. Schift[30] defines NIL as a parallel patterning method in which a surface pattern of a stamp is replicated into a material coated on a hard substrate by mechanical contact and 3D material displacement, to be used in fields until now reserved to electron beam lithography (EBL) and Photolithography (PL).

In the following, in order to make easier the reading of the chapter, the thermal nanoimprint lithography will be referred to as nanoimprint lithography (NIL), and only when other techniques are mentioned, their specific name will be used.

In thermal nanoimprint lithography a hard stamp, typically obtained from a silicon wafer, is pressed into a thin thermoplastic polymer film heated at least 70° – 90° C above its glass transition temperature (T_g) (see Fig 3.2).

A widely used thermoplastic polymer is PMMA which has a T_g of 100° – 110° C depending on the molecular weight. When PMMA is heated to temperatures above 170° C it behaves as a viscous liquid, and when the stamp is pressed against the polymer film the nanostructures can be easily indented into it. The stamp and substrate with the polymer are kept at constant pressure and temperature for the time necessary to complete the process (see Fig. 3.3); then, they are cooled keeping the stamp in contact under constant pressure in order to avoid polymer reflow (Fig. 3.4). When the system is below the glass transition temperature the stamp can be removed leaving the pattern frozen into the polymer (Fig. 3.5).

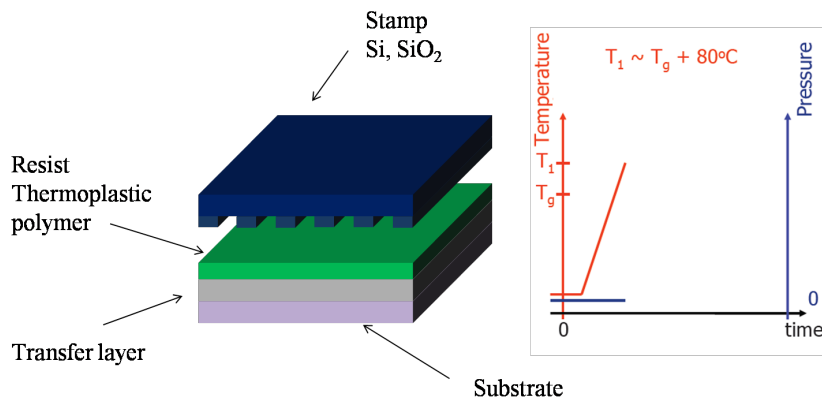


Figure 3.2: Sketch of a thermal nanoimprint lithography process (left) and of the temperature-pressure temporal sequence (right).

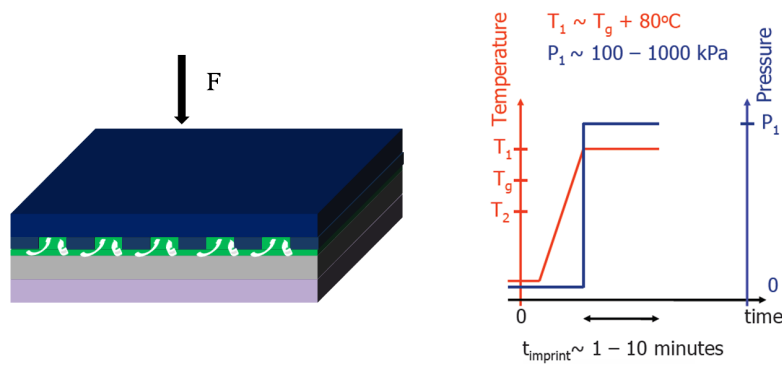


Figure 3.3: The stamp and the substrate with the polymer are kept at constant pressure and temperature for the time necessary to obtain the complete filling of the cavities and the optimal residual layer thickness.

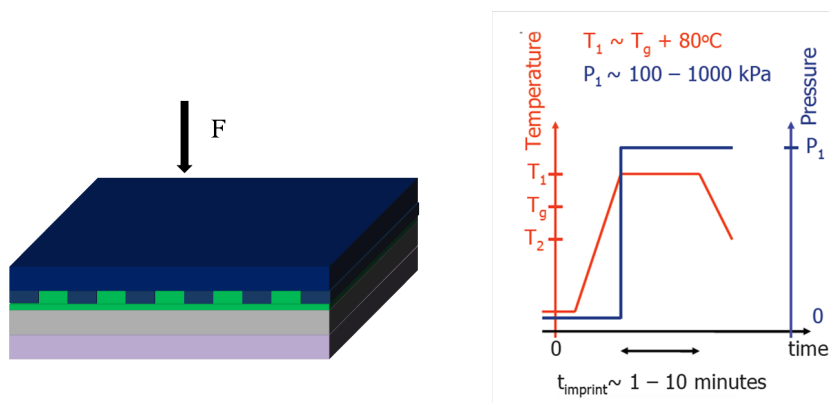


Figure 3.4: During the system cooling the stamp is kept under constant pressure in order to avoid polymer reflow.

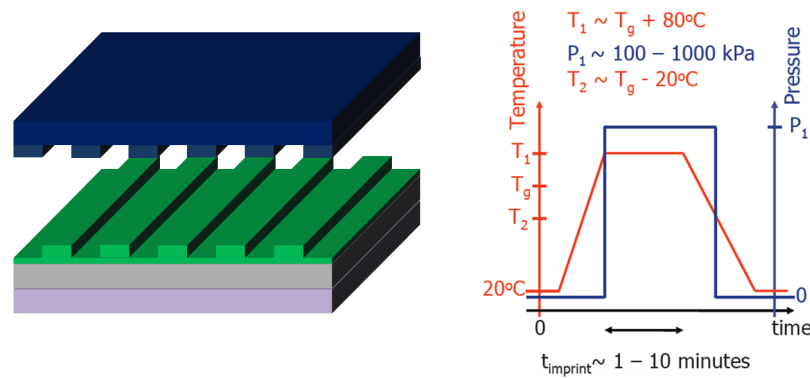


Figure 3.5: The stamp is separated (or demolded) when the system reaches a temperature at least of 20° below T_g and a glassy state.

Generally, the patterned polymer is etched in an oxygen plasma for removal of the residual polymer layer always remaining at the bottom of the imprinted features exposing the substrate beneath as shown in Fig. 3.6. This is an essential step in order to be able to transfer the pattern into a transfer layer, or in most cases directly into the substrate.

After residual layer removal, the pattern can be used as etching mask in the case the resist shows to withstand sufficiently the erosion and damage due to the dry etching process; otherwise, after being coated with a metallic layer (e.g. nickel), which can be either evaporated or sputtered, the sample undergoes to a lift-off process removing the metallic mask on the surface of the polymer (resist) (see Fig. 3.7). Generally a nickel mask allows to obtain high aspect ratio structures in the substrate with a well defined profile because of its high prolonged withstanding to dry etching processes in fluorine or chlorine based plasma used for the silicon etching.

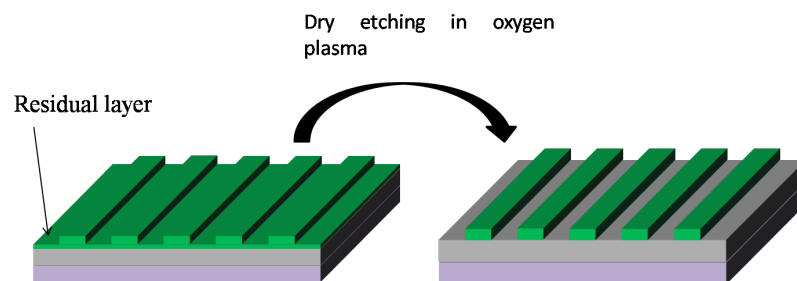


Figure 3.6: The patterned polymer can be processed using a oxygen plasma in order to remove the residual layer exposing the transfer layer beneath.

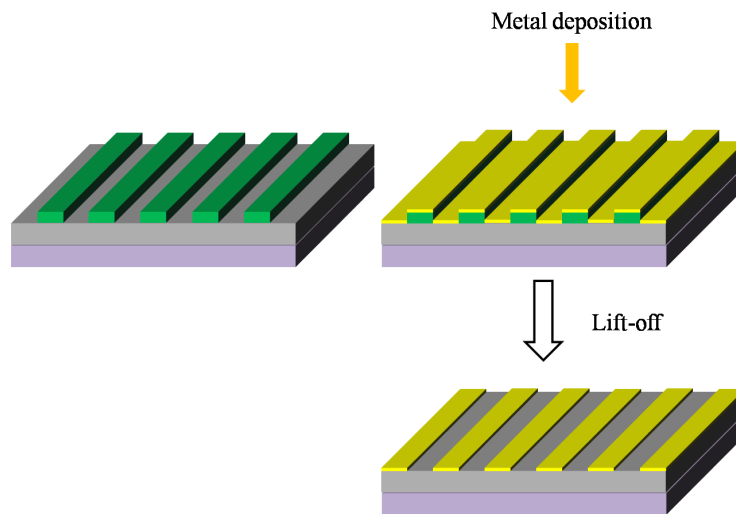


Figure 3.7: The sample surface can be coated with a metallic layer and then the polymer removed by stripping in a remover solution. The lift-off process reveals a metallic mask on the surface.

3.2 Stamp

Nanoimprint lithography is based on the use of a stamp (or mold) with nanostructured surface relieves. The origination of the pattern of the stamps has to be obtained by other lithographic techniques such as EBL, laser writing or any other technique capable of originating a pattern from a CAD design. The stamps are generally made in silicon, or other silicon-based material (e.g. silicon dioxide or silicon nitride), metals (e.g., nickel), or polymeric materials that have a high mechanical strength and durability. These properties are essential for producing nanoscale features avoiding patterns distortion, buckle, or collapse during imprinting, or breaking of nanostructures during separation, in order to preserve the shape and aspect ratio as well as the pattern definition at size scales of 10 nm and below.

Mold Fabrication

The materials for mold fabrication are selected considering aspects such as the compatibility with traditional microfabrication processing and their applications, the surface energy and availability of a method for surface functionalization in order to reduce the adhesion towards polymer. Furthermore, mechanical properties are critical issues such as the Young's modulus, that is a measure of the material stiffness, give the response of the stamp under stress during the imprinting. Deformations of the mold can be the result of a low Young's modulus.

In thermal nanoimprint lithography, thermal expansion and Poisson's effects make difficult the alignment, unless the same material for the sample substrate and the stamp

is chosen for compensate the mechanical and thermal expansion effects of the pattern with the same expansion of the substrate on which the pattern has to be replicated. In the case of a silicon stamp, the material has a coefficient of thermal expansion of $2.6 * 10^{-6} \text{ } ^\circ\text{C}^{-1}$, a Young's modulus of 107 GPa and a Poisson's coefficient of 0.3. At a temperature of 160°C and pressure of 5 MPa as imprinting conditions the diameter of a 4 in wafer would be $36.5 \text{ }\mu\text{m}$ larger than at room temperature and without load (the thermal and elastic contribution are $35.1 \text{ }\mu\text{m}$ and $1.4 \text{ }\mu\text{m}$, respectively). A diameter variation of this entity can entail an insufficient alignment for imprinting features in the nanometer scale.

Material	Young's modulus (<i>GPa</i>)	Vicker's hardness (<i>MNm⁻²</i>)	Coefficient of thermal expansion ($^\circ\text{C}^{-1}$)	Melting point ($^\circ\text{C}$)
<i>Si</i>	107	-	$2.6 * 10^{-6}$	1414
<i>SiO₂</i>	94	-	$7.0 * 10^{-6}$	1728
<i>Si₃N₄</i>	-	1600	$3.3 * 10^{-6}$	1900
<i>SiC</i>	450	2850	$3.3 * 10^{-6}$	2700
<i>Ni</i>	214	638	$13.4 * 10^{-6}$	1455
<i>Al₂O₃</i>	370	1400-2100	-	2054
<i>TiN</i>	2300	600	$9.4 * 10^{-6}$	2930
<i>WC</i>	670	1300-2200	-	2850
<i>Cr</i>	279	131	-	1860

Table 3.1: Properties of some materials just used for stamp in nanoimprint based lithography or studied for a possible application such as *Al₂O₃*, *WC* and *Cr* (*Unpublished results from NAPA project*).

Typical materials are silicon, silicon dioxide, silicon nitride, silicon carbide, nickel, sapphire and diamond film. Generally, *Si* and *SiO₂* (Fig. 3.8(a,b)) are used in thermal nanoimprint lithography because they combine a sufficient hardness and durability properties with reasonable costs and flexibility of fabrication; moreover, various surface treatments have been tested for these materials obtaining optimal results with self-assembled monolayer (SAM) of silane molecules as will be described later. Nickel stamps are generally used in roll-to-roll NIL as seen in Fig. 3.8c and they can be used in other nanoimprint based lithography (Fig. 3.8d). *Al₂O₃* has been reported only in preliminary tests and not extensively investigated as material for stamps (perhaps for the difficulty of its etching and the lack of a good technical solution for the antiadhesion coating).

Generally, the scheme of fabrication of a stamps consists of the following steps:

- a resist material is spin-coated onto the flat mold surface;
- the resist is patterned by UV lithography for microscale and large features or electron-beam lithography for very small features, interference lithography for

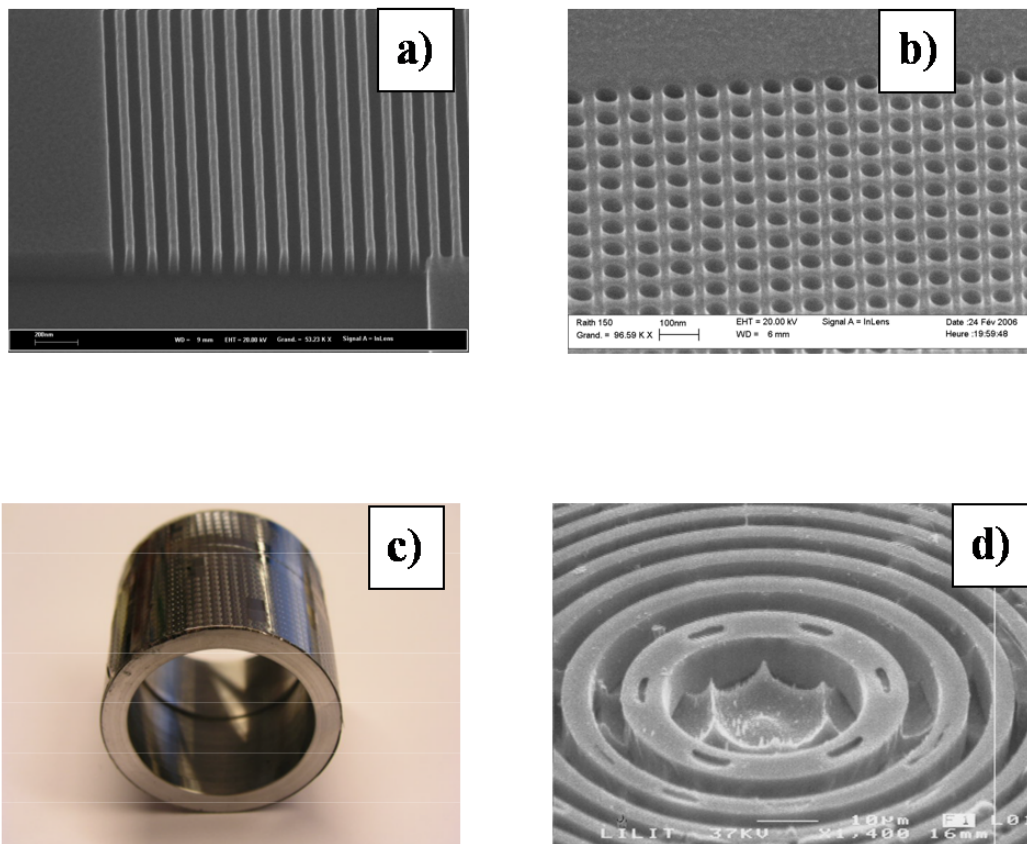


Figure 3.8: Arrays of silicon lines (a) (pitch 100 nm) and 80 nm silicon anti-dots (b) etched using a dry etching process in an inductively coupled plasma tool and PMMA resist as etching mask. (c) Nickel test stamp wrapped on an imprint roll for roll-to-roll machine at VTT; (d) 3D master in nickel ($100\mu\text{m}$ thick) obtained inverting an imprinted PMMA structure by nickel electroplating.

large-area periodic features, or NIL itself;

Then, the resist can be used as etching mask in a dry etching process if its resistance allows to transfer the pattern into the substrate without loss of control of the feature size (or critical dimension, CD) and verticality of walls (Fig. 3.9); otherwise, a metal mask can be used as mask for pattern transfer (Fig. 3.10):

- a metal (e.g. nickel) is deposited over the patterned resist template, with a directional control in order to coat only the top of the polymer features and the bottom of the holes but not the vertical walls;
- by dissolving in liquid solution the polymer, the metal on top of it is lifted-off, while remaining on the bottom of the features, anchored to the substrate. This process, called lift-off, requires the absence of continuity between the metal on top of polymer and that on the bottom of the features in order to take place reliably. A lift-off process removes the coated resist template leaving on the Si substrate a patterned metallic mask layer;
- a dry etching process is used for removing anisotropically the Si material in the unmasked region, producing the surface relief structures required for NIL.

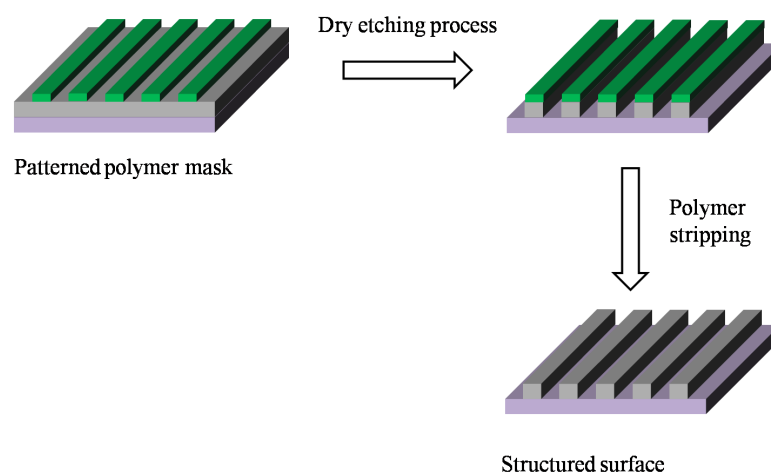


Figure 3.9: The polymer is used as a mask for a dry etching process to transfer the pattern into the substrate.

Some examples of molds, which have been obtained with the above described processes, are shown in Fig. 3.11(4) such as mold with high resolution lines etched into a thermal oxide layer on silicon or with periodical features fabricated by double imprinting with orientations of 90° with respect to each other, followed by metal lift-off and

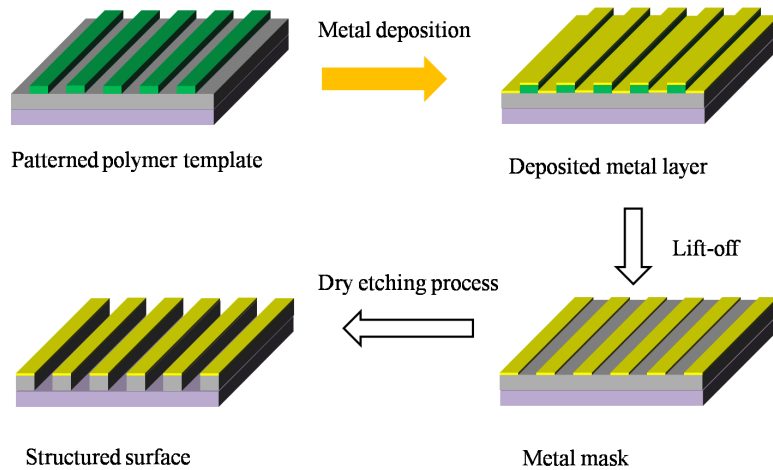


Figure 3.10: In the case the polymer does not resist to the dry etching process, a metallic layer is deposited on the sample surface following by the lifting-off of the polymer. A nickel metal mask has an optimal etch resistance to fluorine or chlorine based plasma etching and it allows the fabrication of high aspect ratio structures into silicon and other silicon-based materials.

reactive ion etching. For the fabrication of molds without patterning an intermediate sacrificial polymer film, a possibility is represented by the use of focused ion beam (FIB) technology to directly mill desired mold features: this possibility is particularly interesting for the fabrication of 3D structures that would be very difficult to produce involving multiple process steps, if not impossible.

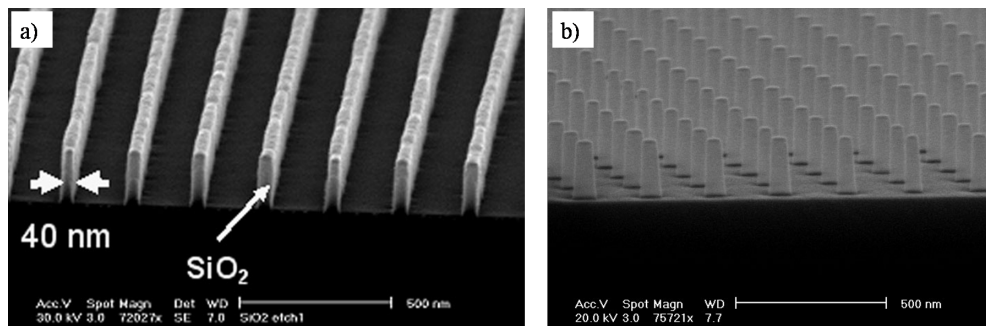


Figure 3.11: a) SEM image of a patterned silicon dioxide layer on silicon substrate, b) SEM image of a stamp fabricated by using a grating mold and performing NIL twice, at orientations of 90° with respect to each other [31].

Mold Surface Functionalization

A critical issue in nanoimprint lithography is the separation of the stamp from the imprinted polymer because of the adhesive force between the two surfaces (see Fig. 3.13); the high density of nanoscale protrusions on stamp surface increases the total area of contact, leading to strong adhesion. This can lead to tearing off the molded polymeric features during separation, as shown in Fig. 3.12.

During the release, the vertical slipping movement of the stamp should not be impeded by frictions at the interfaces and nanoscopic interlocking of structures caused by sidewall roughness should be elastically absorbed by the molded material. The polymer film must have good adhesion to the substrate while the adhesion to the stamp surface has to be minimized in order to allow demolding without pattern damage. If the stamp material does not exhibit sufficient anti-adhesion properties (fact that is linked to the surface energy of the stamp) to the molded material, the stamp or the polymer have to be properly modified:

- incorporating an internal release agent into the resist formulation;
- applying a low-surface energy coating (anti-sticking layer) to the mold to reduce its surface energy [32, 33].

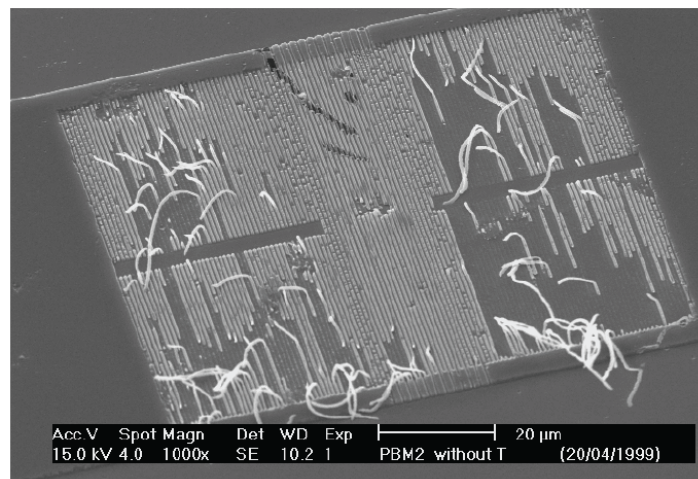


Figure 3.12: Unsuccessful results of a nanoimprinting process caused by problems during the separation of the stamp from the imprinted thin polymer film; this example shows how the release of the mold can represent a critical step in nanoimprint lithography [34].

The stamps are generally fabricated in silicon and on account of this the most widely adopted approach is to form a SAM of a fluorosilane release agent on the mold surface (e.g. 1H,1H,2H,2H-perfluorodecyl-trichlorosilane), either by a solution-phase or a vapour-phase reaction called silanization (see Fig. 3.13). The solution-phase deposition can be performed by immersion in a solution of silane and organic solvent such

as toluene or iso-octane with a concentration typically of 1 – 10 *mM*. The vapour-phase deposition can be performed by chemical vapour deposition (CVD), either at ambient pressure by heating the silane on a hot plate or by applying a moderate vacuum of some mbar. The vapour deposition method is not affected by the ability of a surface to be wet by the solution, so that it is suitable for stamps with extremely small nanostructures.

The anti-adhesive coating has to be chemically inert and hydrophobic, but at the same time it has to allow the filling of the mold cavities when the polymer is in its viscous state; the SAMs have characteristics suitable for the use as release agent. A SAM is an organized layer of molecules composed of a reactive head group, a lipophilic long chain and a functional tail group, that can be hydrophilic or hydrophobic. The SAMs are produced by the chemisorption of the head groups onto a substrate from either the vapor or liquid phase followed by an organization of the chains due to van der Waals interactions. The molecules adsorb readily because they lower the surface energy of the substrate and are stable due to the strong chemisorption of the head groups which form covalent bonds with the superficial hydroxyl groups of the oxides or silicon previously soaked in an oxidizing solution such as piranha solution ($H_2SO_4 : H_2O_2$). In the case of perfluorodecyl-trichlorosilane, the reaction entails the elimination of hydrochloric acid and the production of covalent $-Si-O-Si-$ bonds between the SAM molecules and the substrate surface as shown in Fig. 3.13. Fluorinated trichlorosilanes with different carbon chain lengths are commonly used due their property of forming SAMs with very low surface energy, of being rather inert and stable and high resistance against temperature and pressure. They support multiple long embossing sequences with repeated temperature cycles higher than 200°C. The low surface energy release layer on stamp surfaces improve imprint qualities and also increases the stamp lifetime significantly by preventing or reducing surface contamination.

Using atomic force microscope, ellipsometry, IR spectroscopy and contact angle measurement, Jung et al [35] compare coatings deposited by the two different processes concluding that in vapour-phase the resulting coating provides superior surface-release properties. Stamps, which have been previously treated with fluorosilane, can be used to imprint also thousand times before their anti-sticking properties degrade and a new coating is required.

A further solution for improving the detachment is to choose a mold material with an intrinsically low surface energy and a sufficient mechanical strength in order to avoid features deformation. Teflon AF2400 ($T_g = 240^\circ\text{C}$), as demonstrated by Lee et al [36] is a suitable material for stamps; it is a copolymer of 2,2-bis(trifluoromethyl)-4,5-difluoro-1,3 dioxole and tetrafluoroethylene. It has a high tensile modulus of ca. 1.6 *GPa* compared to 1 – 10 *MPa* of elastomeric materials such as polydimethylsiloxane (PDMS) used in soft-lithography. Furthermore, it has a surface energy lower than PDMS (15.6 *dyncm*⁻¹ vs. 19.6 *dyncm*⁻¹). Therefore, Teflon stamps are stiff enough

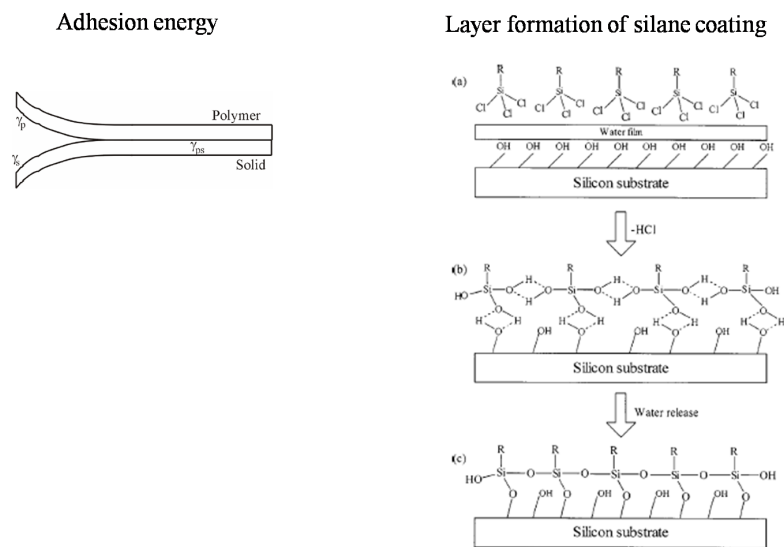


Figure 3.13: The adhesion energy between the polymer surface and stamp surface determines the releasing of the stamp (left); a) The reaction between the silane head group and the silicon surface is in need of a thin layer of water on surface, b) the hydroxyl groups of water substitute for chloro anions, hydrochloric acid is eliminated and hydrogen bonds bind the surface-silane hydroxyl groups and silane-silane hydroxyl groups, c) after water condensation the silane molecules result chemisorbed on the surface and binded to other molecules [34].

for patterning small features without deformation and the low surface energy allows an easy de-molding after the imprinting. This kind of stamps has some practical advantages with respect to silicon, which are observed during the fabrication and the imprint process. They are produced either by casting the fluoropolymer solutions over a template and drying off the solvent [37] or by imprinting of the polymer at $350^\circ C$ under high pressure without dry etching processes as in silicon stamps fabrication. In the imprint process, a polymeric mold, that is more flexible than silicon, can provide a better conformal contact with the substrate to be patterned reducing the pressure needed during the imprinting step.

3.3 Resist

The nanoimprint lithography consists of embossing a resist material in order to make the conformal replica of the pattern fabricated on the stamp's surface. The resist must have properties suitable for imprinting:

- a Young's modulus lower than that of the mold during imprinting;
- the minimal pressure required to perform the imprint should be higher than the shear modulus of the polymer;
- a sufficiently low viscosity at the imprinting temperature to allow the NIL process within a practical time frame.

The last requirement will be described in detail in the section 3.4 considering the flow (often called "squeeze flow") of a Newtonian liquid between the features of the stamp and the surface substrate. The material in addition to the previous properties can be characterized by a high etch resistance in order to be used as mask in a etching process of the substrate.

Thermoplastic Resists

The resist, used in the thermal nanoimprint lithography, is a thermoplastic polymer which meets the requirements concerning the Young's modulus and viscosity. As the system, composed by mold, substrate and polymer, is taken to a temperature of $70^\circ - 90^\circ C$ above the glass transition temperature (T_g), both Young's modulus and the zero shear viscosity (η_0) (Fig. 3.14) drop by several orders of magnitude compared to their respective values at room temperature. At these working temperatures the polymer material reaches a viscous flow state; in a process window of $10^3 - 10^7 Pa \cdot s$, the polymer viscosity is low enough for efficient squeeze flow at high pressure. After the system cooling to a temperature below T_g the polymer reaches a sufficient stiffness to preserve the imprinted pattern after de-molding. The viscosity is a measure of the

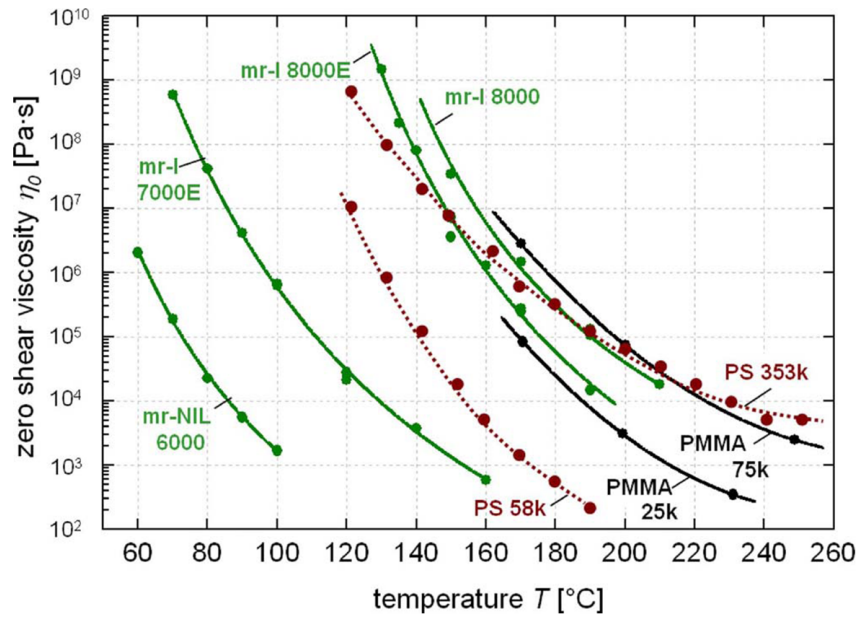


Figure 3.14: Zero shear viscosity at temperature above T_g for some standard resists used in thermal nanoimprint lithography for different polymers, taken from different sources: PMMA with M_w of 25 and 75 kg/mol , PS with M_w of 58 and 353 kg/mol and the commercial resists mr-I 7000E, 8000, 8000E, and mr-NIL6000 (Micro resist technology) [30].

resistance of a fluid to flow which requires being deformed by either shear stress or normal stress. It describes a fluid's internal resistance to flow and may be thought of as a measure of fluid friction. The motion of polymer chains is allowed at temperatures above the T_g ; this temperature characteristic of the material is determined by several factors such as the strength of intermolecular forces, the intrachain steric hindrance due to crosslinking and branching, the presence of bulky and stiff side groups. T_g can be defined as the temperature at which the viscosity reaches a value of $10^{12} Pa \cdot s$ [16]; only few degrees below this temperature the flow process in the fluid becomes extremely slow and the polymer responds as a solid to external forces or deformations except for very long times.

Generally, as resists for NIL are chosen polymers with rather low T_g in order to allow working at low temperature reducing the process time; on the other hand, the stability of the polymer nanostructures after de-molding cannot be guaranteed if the T_g is close to room temperature or to the temperature reached in dry etching plasma processes resulting in the change of the shape and dimension of the imprinted features. During de-molding also the stress build-up due to the applied pressure at a temperature below T_g can affect the stability and integrity of the imprinted features [38].

In addition to glass transition temperature the polymer molecular weight (M_w) is affecting the viscosity versus temperature dependence; for the PMMA shown in Fig.

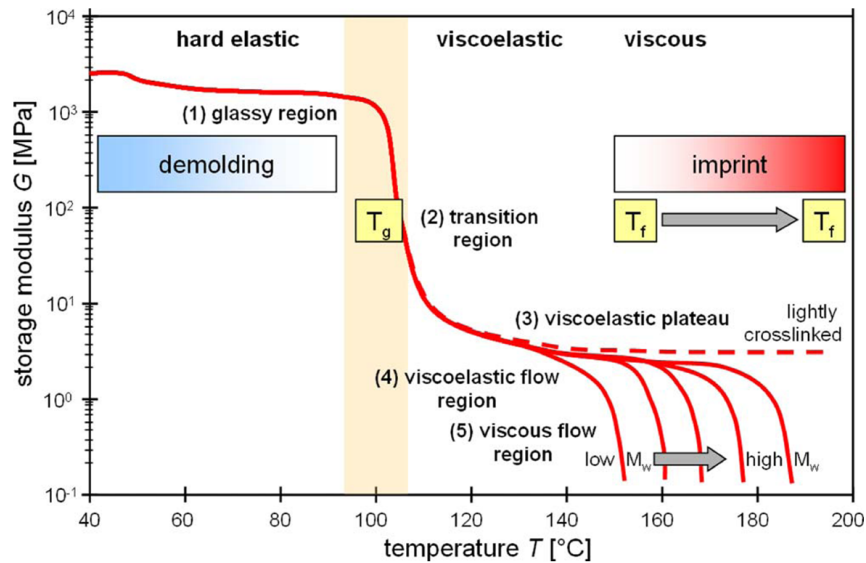


Figure 3.15: The graphic shows schematically the behaviour of storage modulus (G) depending on temperature, molecular weight, and cross-linking for a polymer with a T_g around 100°C . The NIL process is promoted by large drop of G at two temperatures, T_g and T_f [30].

3.14 with 25, 75 and 353 Kg/mol of M_w the T_G are very close, i.e. 105, 98 and 95°C respectively, while the zero shear viscosity curves are strongly dependent on the molecular weight.

The so-called critical molecular weight (M_c) of a given polymer is the molecular weight at which a temporary network of entanglements reaches macroscopic dimensions increasing the viscosity; for PMMA, M_c is 3 Kg/mol . Polymers with $M_w < M_c$ can be imprinted at lower temperatures, lower pressures, or within shorter times; but the absence of such a network of entanglements can make the material so brittle to incur fractures of imprinted polymer features during the mold-separation step.

To choice of a thermoplastic polymer for NIL and its imprinting temperature requires the knowledge not only of T_g but rather of the η_0 dependence on the temperature. In Fig. 3.15 is shown the relationship between the storage modulus (G) and the temperature; G in viscoelastic solids measures the stored energy, representing the elastic portion while the loss modulus measures the energy dissipated as heat, representing the viscous portion. G is nearly constant between the viscoelastic and flow state and forms a plateau because the chain segments between entanglements can move in linear amorphous polymers. G at a specific temperature T_f (flow temperature) drops again rapidly. The width of the plateau is determined by M_w and M_c .

The mechanical, thermal and chemical properties of material required in the thermal nanoimprint lithography make polymers suitable for the processing because their properties can be tailored by synthesis in order to improve their mechanical response,

to lower their temperature of process and to enhance their etch resistance.

3.4 Polymer flow and imprint process

Previously it has been shown as NIL entails the patterning of a polymer layer at a temperature largely above T_g by means of a stiff stamp structured on surface. The sum of times needed for the heating and cooling cycle, for the complete filling of the stamp cavities and for obtaining the optimum residual layer determines the required process time and the throughput of this technique. Further than the viscosity of the material at the process temperature, also the applied pressure, the thickness of the polymer and the distances over which the material has to flow to fill the cavities affect the required time.

The applied pressure must both allow a complete patterning of the polymer in the shortest possible time and be low enough to ensure that the stamp withstands several imprinting cycles without damages. The lifetime of the stamp is a critical issue because of the high cost for its fabrication. Moreover, high applied pressure can result in cracks in the substrate, in presence of small dust particles, which produce concentrated stresses at the stamp/surface interface.

The role of transport distances for polymer flow is shown by the different time required for filling cavities stamps in case of protrusions with different sizes under identical imprinting conditions of temperature and pressure.

Large, isolated and elevated features in polymer surrounded by emptied areas require long time for filling with respect to small periodic structures with a ratio 1 : 1 between width and spacing.

These considerations derived from several experiments, find a theoretical justification in the analysis of the squeeze flow of a Newtonian fluid between parallel disks as shown in Fig. 3.16. The system is composed of two parallel disks separated by a distance $h(t)$ corresponding to the thickness of a fluid layer placed within. A force applied to a disk leads to the flow of the fluid layer. The Stefan equation (3.1) expresses the applied force in terms of the disk radius R , the motion of both disks of same magnitude but opposite sign ($\pm dh/dt$) and the shear zero viscosity η_0 of the fluid as:

$$F = -\frac{3\pi R^4}{2h(t)^3} \frac{dh}{dt} \eta_0 \quad (3.1)$$

The Stefan equation shows the dependence of the force on:

- viscosity $\longrightarrow F \propto \eta_0$
- disk radius $\longrightarrow F \propto R^4$
- fluid film thickness $\longrightarrow F \propto h_0^{-3}$

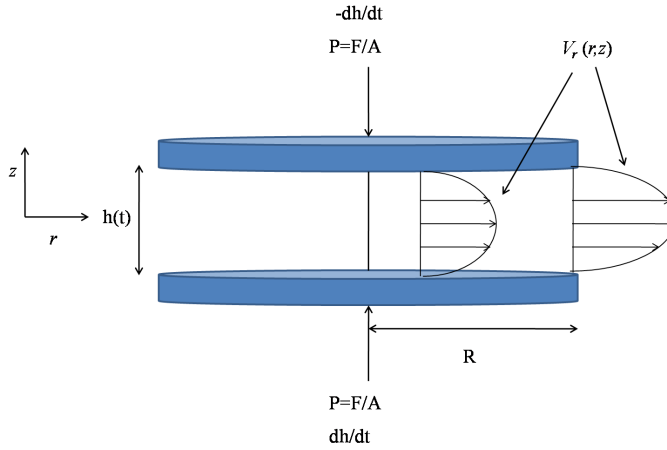


Figure 3.16: Schematic representation of a squeeze flow of a Newtonian liquid placed in the gap between two parallel disks (radius R) separated by a distance $2h_0$ under an applied force F . The flow is maintained against the atmospheric pressure p_a .

The force linearly depends on viscosity that decreases by various order of magnitude with increasing temperature (see Fig. 3.17) while it does not depend on the shear rate in this model based on a Newtonian liquid. This assumption is valid also in the case of low shear rate; whereas an increasing of the shear rate entails the changing towards a non-linear flow behaviour and the viscosity would depend on the shear rate as shown in Fig. 3.18 where the viscosity rapidly decreases for higher shear rates. A lower η_0 entails a reduction of the process time under the same conditions of F , R and h_0 .

The dependence of viscosity on temperature for polymer that have a glass transition temperature is, usually, determined by the William-Landel-Ferry model (WLF):

$$\mu(T) = \mu_0 \exp\left(\frac{-C_1(T - T_r)}{C_2 + T - T_r}\right) \quad (3.2)$$

where T , C_1 , C_2 , T_r and μ_0 are empiric parameters.

The polymer viscosity decreases at higher temperatures because of the increasing ability of the chains to move freely. A truncated power law model can describe the dependence of the viscosity on the shear for a typical material as PMMA that is considered to a good approximation as a purely viscous fluid (see Fig: 3.18).

$$\check{\eta}(\dot{\gamma}) = \begin{cases} \eta_0 & , \dot{\gamma} < \dot{\gamma}_0 \\ \eta_0 \left(\frac{\dot{\gamma}}{\dot{\gamma}_0}\right)^{\frac{1-k}{k}} & , \dot{\gamma} > \dot{\gamma}_0 \end{cases}$$

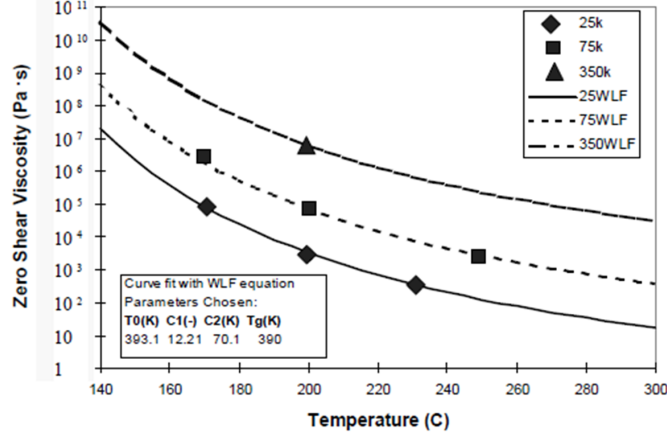


Figure 3.17: The graphic shows the dependence of η_0 of PMMA on temperature for three different molecular weights. The plots have been obtained by fitting of experimental data with the WLF equation [34].

η_0 is the zero shear viscosity, with the limiting value:

$$\eta_0 = \lim_{\dot{\gamma} \rightarrow 0} \check{\eta}(\dot{\gamma}_0) \quad (3.3)$$

$\dot{\gamma}_0$ is the limiting shear velocity, at which the approximated stationary shear viscosity changes over from the constant value η_0 to a power law model, and k is a constant.

The quadratic dependence of the force on the transport distance is obtained considering the flow velocity and the contribute due to the shear stress. The stamp design defines the transport distance and in the case of the flat disk of radius R (FIG. 3.16), the fluid flows radially from the disk centre outwards to its circumference. Considering the conservation of momentum for an incompressible liquid and fulfilling the conditions of continuity, the velocity increases with the radial distance as:

$$v_r(r, z) = -\frac{3}{4} \frac{dh}{dt} r \left[1 - \left(\frac{2z}{h(t)} \right)^2 \right] \quad (3.4)$$

In z-direction, the velocity profile is parabolic; the velocity has the maximum value for $z = 0$ at half distance between the disks, while for $z = \pm h(t)/2$ at the interfaces, the velocity is zero if we suppose, as it is typically the case, that no slipping of the fluid takes place at the interfaces between stamp and substrate. The region between these two boundary points is divided into some layers in base of their velocity; the different

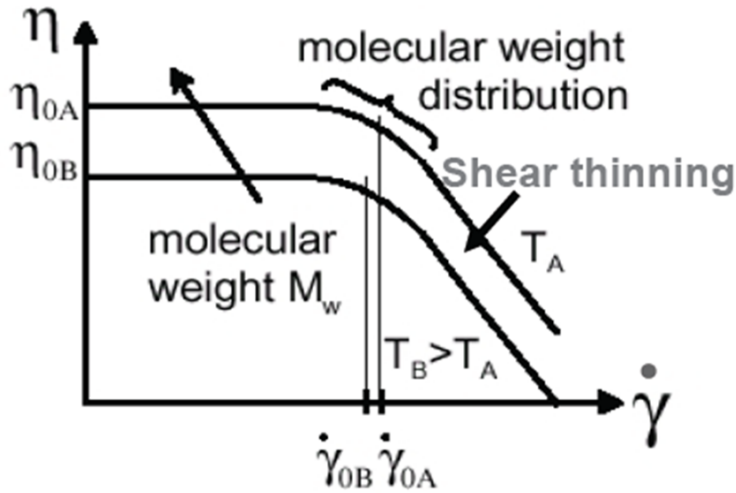


Figure 3.18: The graphic shows schematically the dependence of the viscosity on the shear for two temperatures T_A and T_B ; $\dot{\gamma}$ is the shear velocity and η is the shear viscosity [34].

velocity causes shear stresses acting between the layers. The integration over these shear stresses leads to the quadratic dependence of the force on the transport distance.

The dependence of the force on the polymer thickness is examined considering the time required for thinning the fluid layer of initial thickness h_0 to a thickness $h(t)$ lower. Integrating the Stefan equation with respect to dh/dt it is obtained:

$$\frac{1}{h(t)^2} = \frac{1}{h_0^2} + \frac{4Ft}{3\pi R^4 \eta_0} \quad (3.5)$$

The time required for obtaining a residual layer with a final thickness $h_f \equiv h(t_f)$ is:

$$t_f = \frac{3\pi\eta_0 R^4}{4F} \left(\frac{1}{h_f^2} - \frac{1}{h_0^2} \right) \quad (3.6)$$

The Stefan equation can be applied also to other pattern geometries in order to determine the imprinting time necessary to obtain a defined residual layer. In the case of grating stamp composed of lines characterized by a width s and a length L as in Fig. 3.19, the time required to obtain a residual layer with a final thickness $h_f \equiv h(t_f)$, is:

$$t_f = \frac{\eta_0 L s^3}{2F} \left(\frac{1}{h_f^2} - \frac{1}{h_0^2} \right) \quad (3.7)$$

The constant pressure, that is applied to the stamp with lines to the polymer, is obtained considering the force and the features dimensions: $p = F/(sL)$. The equation

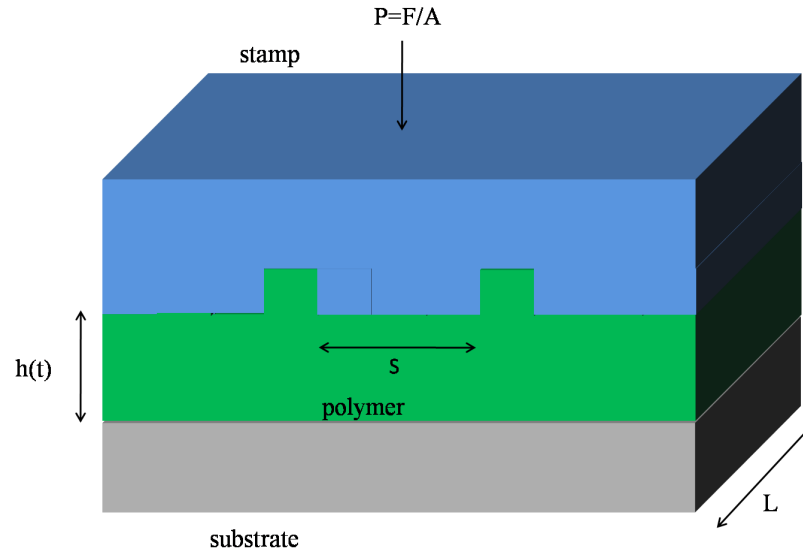


Figure 3.19: Imprinting of a polymer layer, h_0 thick, with a grating stamp of lines characterized by a width s and a length L .

3.7 in function of the pressure is:

$$t_f = \frac{\eta_0 s^2}{2p} \left(\frac{1}{h_f^2} - \frac{1}{h_0^2} \right) \quad (3.8)$$

The dependence of the imprinting time on the s^3 highlights the fact that features characterized by smaller dimensions are imprinted in much shorter time under the same conditions (i.e. applied force until a given residual layer is reached). After complete filling of the cavities, the process of stamps indentation into polymer slows down. As shown in Fig. 3.20 the residual layer under the stamp features is thinned at a much slower rate because the polymer can flow only towards the stamp borders increasing the transport distances.

The model of polymer squeeze flow is used for determining the imprinting time to obtain a well defined polymeric pattern; furthermore, the development of a dry etching process of the polymer needs thin residual layer and its thickness can be previously predicted by the model. Others aspects that must be considered in the imprinting process and will not be treated here are related to:

- the presence of dust particles of some μm diameter at the interface between the polymer layer and the stamp that cause a non-conformal contact and consequently the structures in the vicinity of the particles are not imprinted;
- the need of equilibration mechanism, generally a thin layer of silicone behind either the stamp and the substrate, in order to achieve a conformal contact between

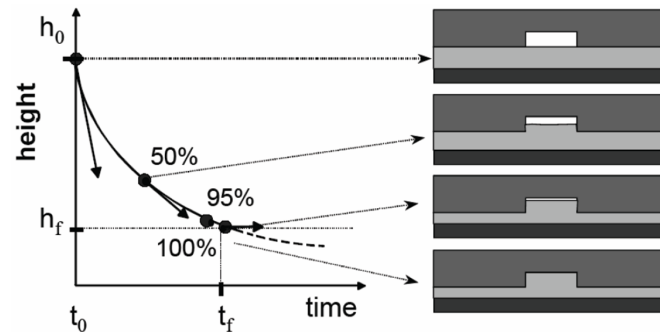


Figure 3.20: The graphic shows the decreasing of the residual layer due to a constant applied force. When the stamp feature are fully inserted in the polymer, the residual layer is thinned at a much slower rate [34].

stamp and polymer layer and to obtain a uniform applied pressure;

- the air inclusion in the cavities during the features imprinting; the air is compressed and can facilitate the demolding of the stamp, but at the same time can deform the polymeric features if demolding is performed before the polymer has reached the glassy state;
- in the demolding the vertical movement of the stamp can damage or deform the polymer features (Fig. 3.21).

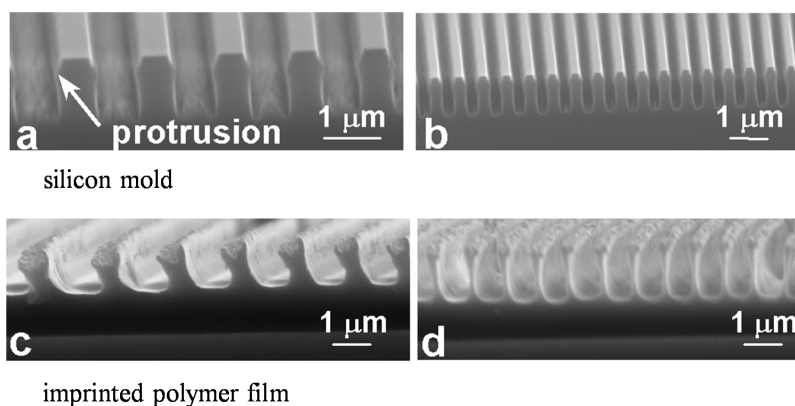


Figure 3.21: Stamps with a grating pattern on the surface, a) line 600 nm wide, 1 μm deep; b) 250 nm wide, 1 μm deep. The polymer pattern obtained has been distorted (c) or stretched (d) during demolding [16].

Chapter 4

The plasma etching process

The fabrication of substrates for wetting measurements has required a fine optimization of plasma etching processes, used to transfer a pattern from a structured polymer or metal layer, acting as a mask into a substrate of silicon or of other material.

The development of etching methods based on plasmas is an ongoing applied research activity since decades, aimed at improving various aspects of the systems and of the processing conditions, such as density of plasma, throughput, etching anisotropy, uniformity over larger and larger substrates, etc.

Many tools have been produced for the silicon dry etching; for instance reactive ion etching (RIE), sputter etching, ion beam etching (IBE), focused ion beam etching (FIB) and inductively coupled plasma (ICP). Inductively coupled plasma etching tools are those of major interest for our work and are characterized by high etch rates due to the dense plasma that can be produced and accurate slope control of sidewall. In this chapter I outline the basic technology concepts of the gas discharge plasmas and their application in dry etching processes; in particular I treat the ICP tool, which is at the basis of the work described in the present thesis.

4.1 Gas Discharge Plasmas

Plasma is considered the fourth state of matter and in nature it is observable in the stars or in phenomena such as Auroras Borealis, near the earth poles or St. Elmo's fire, that is an electrical weather phenomenon typically associated to thunderstorms.

Plasmas or gas discharges are also relevant from a technological standpoint, and are used for example in spectrochemistry for the quantitative determination of chemical species or as the medium to modify the aspect or the behaviour of a material by sputtering deposition or by dry etching processes.

Plasmas hold a fundamental role in micro and nanotechnologies as a fundamental component of the fabrication of micro and nanodevices in silicon based or other classes of materials. The gas discharges are produced by applying a static electric and

magnetic fields, and/or electromagnetic fields that provide the excitation energy to dissociate a gas or a mixture of gasses forming neutral, energetic ions, photons, electrons and high reactive radicals. The charged particles can be accelerated by an electric field toward a substrate target bombarding its surface inducing outgoing fluxes of neutrals, ions, photons and electrons; further, the radicals can react with the substrate material forming reaction products which desorb from the surface into the gas phase.

In this chapter I will describe the physical and chemical principles of the etching technology based on reactive plasmas, introducing first a simple system, the so-called dc-diode glow discharge, and then moving to the rf-discharges with capacitively and inductively coupled discharges [39, 40].

Direct Current (dc) Glow Discharges

A constant potential difference applied to conductive electrodes produces the plasma and a continuous current flows through the discharge, giving rise to a *direct current (dc) glow discharge*. In this configuration, also called (dc) diode system, the role of the cathode is important because it sustains the plasma with the emission of secondary electrons. The voltage for electrical breakdown of a gas placed between two parallel electrodes depends on the geometry of the electrode gap, the gas and the pressure. The relationship is described by the *Paschen's law* [41],

$$V = f(P \times d)$$

where P is the pressure, d the gap distance and f is a function of the form $f(x) = \frac{ax}{\ln x + b}$ and a and b depend upon the composition of the gas. As seen in Fig. 4.1, if the pressure or gap is reduced, the breakdown voltage (V) decreases slowly to a minimum and then rises steeply. Because the number of molecules within the volume between the electrodes is proportional to $P \times d$, when the pressure is too low or the space is too small, most electrons reach the anode without colliding with any gas molecule so the voltage required to obtain the breakdown is higher.

As a self-sustaining plasma is formed, the potential difference applied is generally not equally distributed between the electrodes: the potential of the plasma glow region is almost constant and slightly positive whereas it drops in front of the electrodes in the so-called plasma sheaths. The cathode is at a lower potential than the anode, that is grounded generally (Fig. 4.2).

The asymmetric voltage distribution between the electrodes is due to the different mobility of the ions and electrons; the electrons are accelerated away from the cathode more rapidly than at the anode, and also the ions are accelerated toward the cathode more rapidly than at the anode since the cathode is more negative than the anode with respect to the uniform potential of the glow. Therefore, the concentration of ions is greater than that of electrons in the cathode dark space resulting in a larger field com-

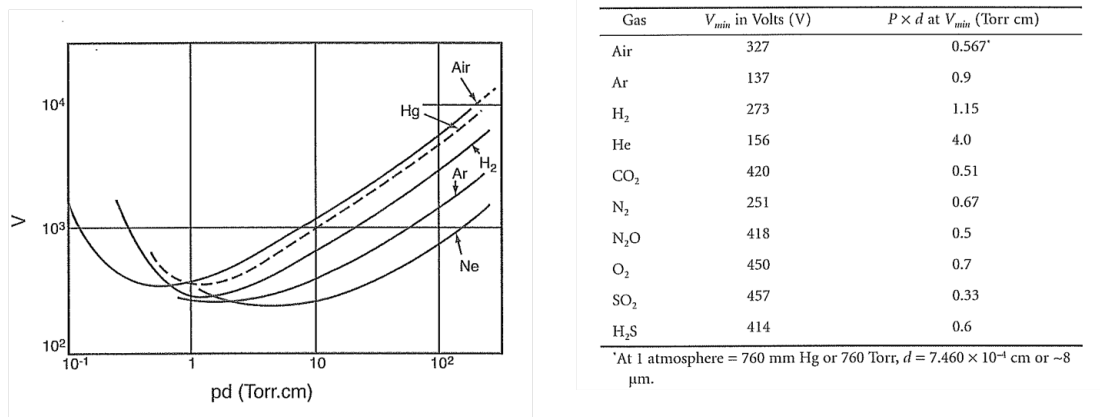


Figure 4.1: Paschen's curves determined experimentally for air and other gases (left); minimum breakdown voltage and Pressure/Distance product at the minimum voltage for some gasses obtained from the Paschen's law (right) [41].

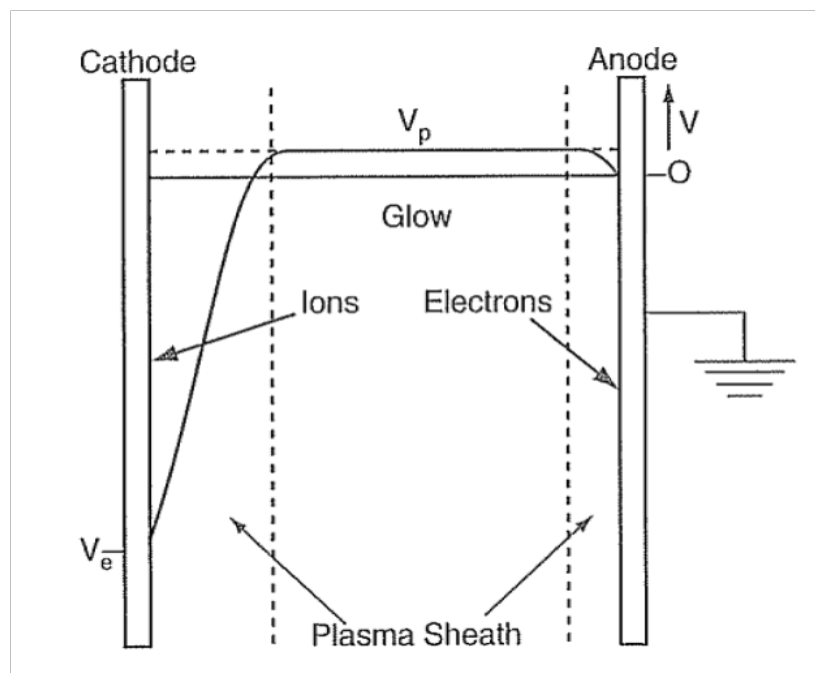


Figure 4.2: Voltage distribution in a (dc) glow discharge. The cathode (left) has a negative potential and the anode (right) is grounded [41].

pared to that of the anode dark space. As seen in Fig. 4.3 the glow discharge can be subdivided into several regions between the electrodes, summarized below:

- the cathode dark space also called Crookes dark space;
- the negative glow (NG):
- the Farady dark space (FDS);
- the positive column (PC);
- the anode dark space.

The discharge regions vary in radiation intensity, potential and electrical field distribution, space charge and current density; their position and wideness depend on the parameters such as pressure and kind of gasses, voltage, current and distance between the electrodes.

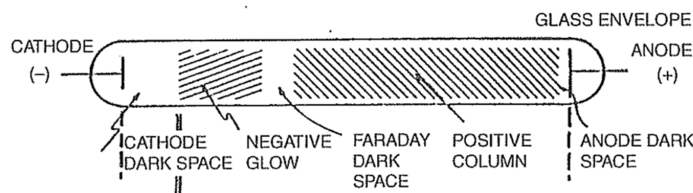


Figure 4.3: The regions between the electrodes in a (dc) glow discharge in equilibrium [41]

Capacitively Coupled (cc) Radio-Frequency (rf) Discharges

A time-varying potential difference is applied to the electrodes producing the plasma and a time-varying electric field giving rise to a *capacitively coupled (cc) radio frequency (rf) discharge*. The role of the electrodes as source of secondary electrons is less important than in (dc) glow discharge because the electrons are constrained to oscillate between the electrodes. Electrons oscillating in the (rf) field acquire sufficient energy to cause ionization for sustaining the plasma also at lower pressure than in a (dc) plasma (e.g. 10 vs 40 *mTorr*). As for (dc) glow discharge, the *Paschen's law* describes the minimum voltage required for the gas breakdown, replacing the gap between electrodes with the mean free path of electrons λ_e . As shown in Fig. 4.4, a typical reactor for ion etching or sputtering deposition is composed of a grounded anode and a cathode, which is applied the (rf) power.

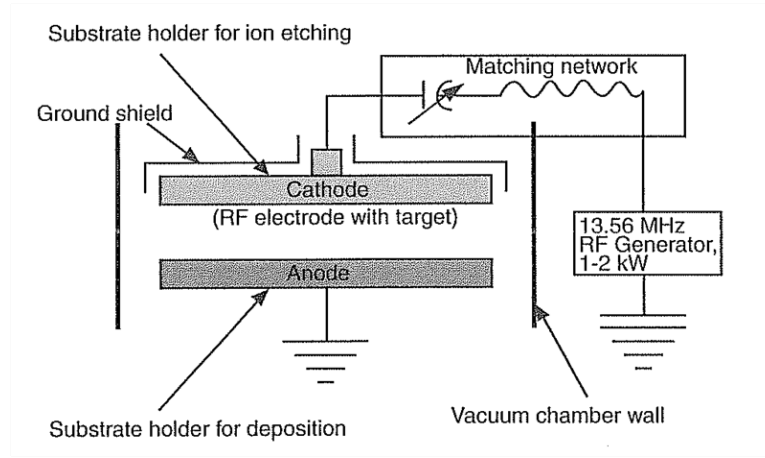


Figure 4.4: Two-electrode setup for RF ion sputtering or sputtering deposition [41].

The electrodes can be non-conductive because applying an alternating voltage, each electrode acts alternately as cathode and anode, indeed the charged accumulated during one half-cycle is at least partially neutralized by the opposite charge accumulated during the next half-cycle. The frequency of the voltage should be high enough so that half the period of the alternating voltage is less than the time during which the electrode would charge up. This class of discharge is called capacitively coupled because the electrodes and their sheaths form a kind of capacitor during the process of power supplying to the plasma.

The typical frequencies are in the radiofrequency range (rf): $1\text{ KHz} - 10^3\text{ MHz}$; in many applications (e.g. ICP machine) the adopted frequency is 13.56 MHz because it is allotted by the international communications authorities, in fact this frequency does not interfere with telecommunications.

The masses of electrons and ions induce a different behaviour when they are subjected to the (rf) voltage. Indeed the electrons, which are lighter, change their direction quickly when the direction of the electric field changes. The electron plasma frequency is given by the following equation, where the electron density n_e is expressed in cm^{-3} :

$$\omega_{pe} = \sqrt{\frac{n_e e^2}{m_e \epsilon_0}} \quad (4.1)$$

$$f_{pe} = 9000 \sqrt{n_e} \text{ (Hz)}$$

Typically the range of electron density is from 10^{10} to 10^{13} cm^{-3} and consequently, the plasma frequency varies from 9×10^8 to $3 \times 10^{10}\text{ Hz}$; so the plasma frequency is much higher than the 13.56 MHz frequency of many plasma applications. The ion plasma frequency is inversely proportional with square root of the mass as expressed in 4.1; therefore light ions, which have an ion plasma frequency higher than the (rf) frequency, follow the variation of the rf electric field, whereas the heavy ions are es-

entially subjected to the only time-averaged electric field. The difference between the electron plasma frequency and ion plasma frequency, produces a potential difference known as *self-bias* between the two electrodes.

Self-Bias

The self-bias is a time-averaged negative (dc)-bias at the (rf) powered electrode and it is less relevant at the grounded electrode; the electrode capacitively coupled to the rf generator becomes the cathode with respect to the other electrode.

Considering the simplified case of a rectangular pulse (Fig. 4.5a) the initial positive voltage that is applied to the capacitor formed by the electrodes and their sheaths is equivalent to the voltage of the discharge plasma. The electrons are accelerated by the electric field toward the electrode and charge up that one; so the discharge voltage drops to a lower value (Fig. 4.5b). After one half-cycle, the changing in polarity of the applied voltage switches the polarity of the discharge plasma. The ion current charges up the capacitor and the voltage drops again, but the difference in mass between electrons and ions produces a different mobility of the two species and so the ion current modifies the electrode potential voltage by a lower absolute value than electron current. At the next half-cycle, the applied potential and the voltage of the plasma change polarity. Because the capacitor is again charged up by the electron flux, the discharge voltage drops more rapidly. Finally the capacitor is sufficiently negatively charged so that the ion and electron fluxes, integrated over one (rf) cycle, are equal to each other. The result is a time-averaged (dc) negative self-bias.

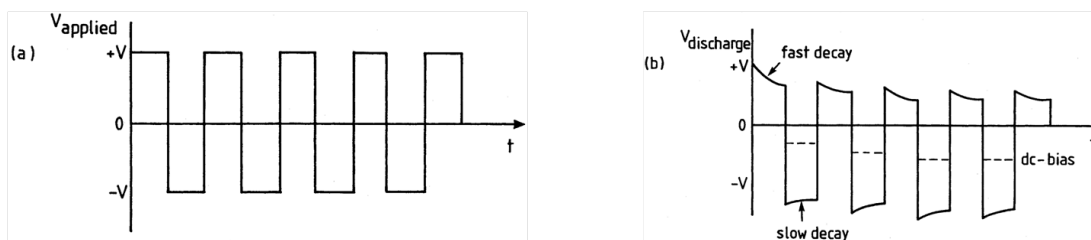


Figure 4.5: Self-bias in a (rf) discharge. (a) applied voltage; (b) resulting voltage over the discharge [40].

Therefore, the ions in the plasma are accelerated by the negative bias toward the (rf) powered electrode (cathode) making it possible to sputter even non-conductive material placed above it. The energy of the charged particles, which bombard the surface, is determined by the contribution of the time-average plasma potential V_p (i.e. the potential of the glow region), the dc cathode potential (self-bias potential) V_{DC} and the peak-to-peak rf voltage $(V_{RF})_{pp}$ applied to the cathode (Fig. 4.6), for which an

approximate relationship exists [41]:

$$2V_p \sim \frac{(V_{RF})_{pp}}{2} - |V_{DC}| \quad (4.2)$$

The maximum energy of the positive ions colliding with the cathode is given by:

$$E_{max} = e(|V_{DC}| + V_p) = eV_T \quad (4.3)$$

with $V_T = |V_{DC}| + V_p$. E_{max} can assume typically values of the order of several hundreds of eV ($\sim 300 eV$). Whereas a substrate placed on the grounded anode is subjected to a flux of ions with a maximum energy $E_{max} = eV_p$, of generally less of $20 eV$ as value. As in a (dc) glow discharge the plasma is divided in different regions and the inner processes are similar.

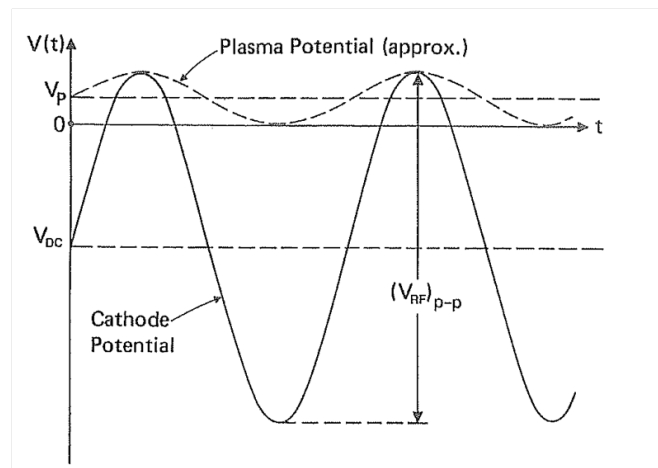


Figure 4.6: Potential distribution in rf glow discharge plasmas where V_p is the potential of the glow region, $(V_{RF})_{pp}$ the voltage applied to the cathode and V_{DC} is the self-bias potential at the cathode [41].

Magnetron Discharges

In a *magnetron discharge* a crossed magnetic field is applied to a glow discharge in addition to a dc or rf potential difference (or crossed electric field). There are three different type of magnetron configurations: cylindrical, circular and planar magnetrons. In a *balanced planar magnetron* an axisymmetric magnetic field (generally in the range of $0.01 - 0.1 Tesla$) is applied with a permanent magnet behind the cathode, in such away that the magnetic field lines start and return at the magnet. As seen in Fig. 4.7, the electrons, which are accelerated away from the cathode by the electric field, are trapped by a magnetic ring, that is formed at the cathode surface, with average radius R and width w . The electrons move in helice, due to the magnetic field, and travel

a longer path-length in the plasma than in a conventional glow discharges. Therefore, there is an increase of the ionization collision rate and, consequently, the ion fluxes are higher compared to conventional glow discharges. An higher ion bombardment of the cathode produces more secondary electron emission. Because of the enhanced ionization and secondary electron emission, the magnetron generally operates at higher currents (e.g. 1 A), lower voltages (~ 500 V) and pressure (~ 1 Pa) compared to a conventional glow discharge. The *magnetron discharges* are generally employed for sputtering deposition, because of the higher ion fluxes, which bombard the cathode, and the low pressure. In these working conditions there are less scattering collisions in the plasma and the deposition is more directed to the substrate placed at the grounded electrode.

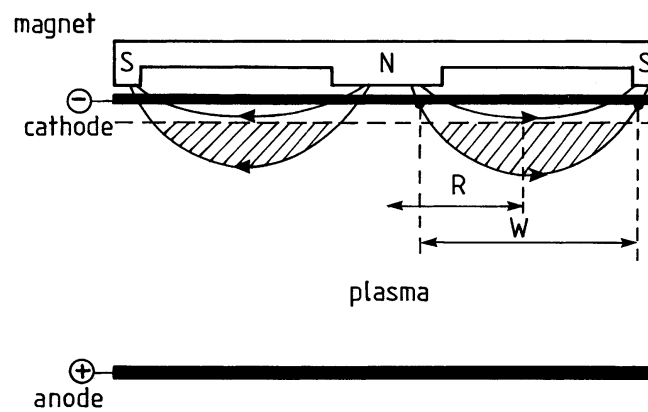


Figure 4.7: Schematic representation of a planar magnetron discharge (From Ref. [40]).

Inductive Discharges

An improvement in the etching and deposition processes with respect to the capacitive (rf) discharges has been obtained with the development of tools working at low pressure and high plasma density. One of the disadvantages of capacitive (rf) discharges is that it is not allowed to control independently the BIAS voltage and current. Therefore, the flux and the energy of the ions bombarding the surface cannot be varied independently, except for systems for which different (rf) frequencies can be applied, but this is the case for very expensive tools found in microelectronic industries and not in academic research laboratory.

The issue is that for obtaining a suitable ion flux the sheath voltage at the driven electrode must be high; this entails the bombardment of the sample surface placed on the driven electrode by high energetic ions, resulting in possible undesirable damage of the surface. Furthermore, the working condition determined by low ion flux and high ion energy leads to a relatively narrow process window for many applications; for

instance, the low ion flux in a (rf) capacitive discharge produces lower process rates and consequently low throughput. The development of systems can control independently the flux and the energy of the ions has become primary and some solutions have been produced:

- rf-triode systems;
- low pressure and high density plasma sources.

In the so-called rf-triode system the sample is placed on the undriven electrode which is applied a second rf-source resulting in an bias independent from the self-bias of the driven electrode. However the process rates are low when working at low pressure even if magnetically enhanced for achieving greater plasma densities.

A different choice has been done with the so-called low pressure and high density plasma sources characterized by a pressure typically in the order of $10 - 50 \text{ mTorr}$ and by a plasma density of about $10^{10} - 10^{13} \text{ cm}^{-3}$ with higher ion fluxes than that of capacitive rf discharges at the same pressure. The main difference with respect to rf capacitively coupled system is that the power furnished by microwave or rf is coupled to the plasma across a dielectric window, rather than by direct connection to an electrode in the plasma. In this way, low voltages across all plasma sheaths at electrode and reactor's wall surface are achieved; generally, the ions are accelerated by low bias dc of $20 - 30 \text{ V}$ toward the walls. Instead, applying a capacitively coupled rf source to the electrode on which the wafer is placed, it is obtained the control of the ion energies. For this reason, the fluxes of ions and radicals are determined by the source power applied to the plasma independently from the ion energies due to the self bias produce by the power applied to electrode under the wafer.

The issues and disadvantages connected with these kind of plasma sources are that it is more difficult to achieve the required process uniformity over large surface areas (e.g. diameter of $20 - 30 \text{ cm}$) with cylindrical geometry of the sources; along the radial direction in fact the plasma formation and the transport phenomena are non-uniform. Moreover, also the efficiency of the power transfer (i.e. the coupling) across the dielectric window must be controlled over a wide range of plasma operating conditions. The reproducibility of the processes is also restricted by the degradation and deposition of material on the dielectric window because of bias at the wall, that accelerate the ions toward the walls, that even if with low energies, produce a deposition of residuals requiring frequent cleaning cycles. The most important high density plasma sources are showed in Fig. 4.8 and generally, they are classified on the basis of the type of coupling of the power to the plasma:

- in the electron cyclotron resonance sources (ECR) electrons travel in a magnetic field and an electric field at microwave frequency, by matching the electron cyclotron resonance frequency (which depends on the magnetic field intensity);

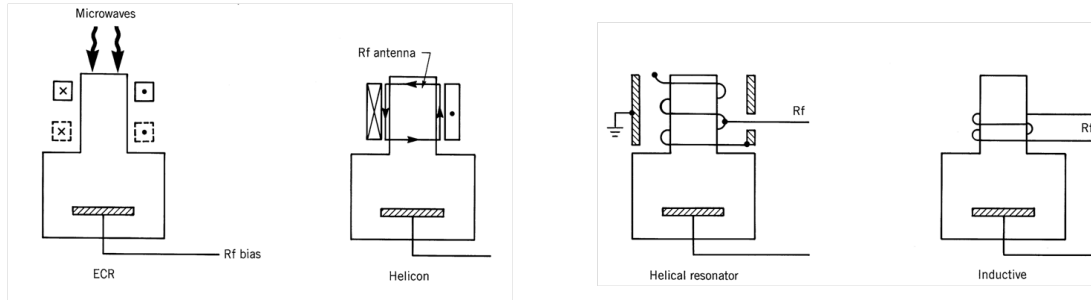


Figure 4.8: Schematic representations of some high density plasma sources [40].

- in the helicon sources the discharge is achieved by rf waves propagating along the plasma;
- the helicon resonator sources use a resonant structure for an efficient plasma generation;
- the inductively coupled plasma sources employ a coil for the plasma generation.

Inductively Coupled Plasmas

The inductively coupled plasma sources (ICPs) is characterized by the coupling between the rf magnetic flux generated by a rf current flowing in a coil placed around the plasma chamber and the solenoidal rf electric field induced by the time-varying magnetic flux density according to the Faraday's law (Fig. 4.9) [42]:

$$\nabla \times \vec{E} = -\frac{\partial \vec{B}}{\partial t}$$

The latter electric field accelerates the free electrons which produce a self-sustaining discharge; as in the other high density and low pressure sources the rf power applied to the electrode, so-called platen, where the samples is placed, generates the self-bias which determines the energy of the bombarding ions. Generally, the electron density in an ICP ($10^{11} \leq n_0 \leq 10^{12} \text{ cm}^{-3}$) with respect to that in a capacitive (rf) discharge is 10 times higher at the same pressure ($\sim 1 \text{ Pa}$).

4.2 Dry-Etching Processes

Lithography techniques, such as UV-photolithography (UVL), E-Beam Lithography (EBL) and nanoimprint lithography (NIL), precede or follow several subtractive and additive process steps. Materials are either removed from or added to a substrate, transferring, for instance, the lithography patterns onto integrated circuits or three-dimensional micro and nanodevices. In the field of micromachining, the etching is

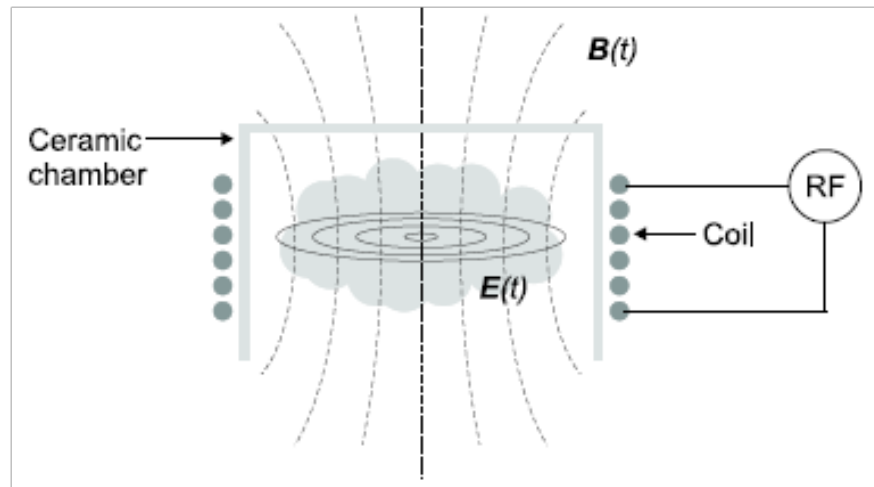


Figure 4.9: In an ICP the axial magnetic field induces an azimuthal electric field [42]

widely used as subtractive technique and can be described as pattern transfer by chemical and/or physical removal of material from a substrate. Generally the pattern is defined in a protective masking layer such as a suitable polymer (so-called resist), an oxide or a metallic film, which has to be more resistant than the substrate to the etching. The etching techniques include gas and vapour phase dry etching processes, etching in liquid phase and technologies for material removing without mask (e.g. Focus Ion Beam FIB).

The dry etching processes are employed for the etching of a wide range of materials such as silicon, polymers and oxides, using several tools, like Reactive Ion Etching (RIE), Inductively Coupled Plasma (ICP), Ion Beam Milling (IBE). This kind of processes are characterized by the etching of a solid surface in a gas or vapour phase, physically by a ion bombardment, chemically by a chemical action through a reactive species at the surface, or by a combined physical and chemical mechanism. Specifically, the material is removed from the solid surface directly into the gas phase by changing in a physical or chemical process into single atoms or molecules, radicals and clusters of a few atoms that can desorb from the surface; the reaction products must be removed from the gaseous phase in order to avoid reactions producing chemical species slightly volatile which can redeposit on the surface. A dry etching process is chosen on the basis of the desired shape of the etching profile (e.g. isotropic, directional or vertical etching profiles) and the selectivity, that is obtained comparing the etching rate of the mask and the substrate.

Physical etching

The physical etching is obtained bombarding the surface with inert ions (e.g. argon ions). The result of the bombardment is determined by the kinetic energy of the in-

coming particles.

- $3 < \text{Ion energy (eV)} < 5 \rightarrow$ particles are reflected or physisorbed;
- $4 < \text{Ion energy (eV)} < 10 \rightarrow$ surface is damaged;
- $\text{Ion energy (eV)} > 10$ (between 10 and 5 KeV) \rightarrow substrate is heated, surface is damaged and material is ejected \rightarrow sputtering and ion etching;
- $\text{Ion energy} > 10keV \rightarrow$ ion implantation.

The ions are accelerated towards the cathode due to the gradient in the potential distribution; therefore, a substrate placed on the electrode is subjected to a bombarding in a direction normal to the surface. The physical nature of the process determines main characteristics:

- the volatility of the etching products is not as critical as for dry chemical etching;
- the ion energy applied to eject material is higher than the energy of the chemical bonds involved; therefore the process has a low degree of selectivity and the difference in etching rates for various materials is not large;
- generally, physical etching is a suitable option if specific chemical reactions are not available;
- the etching rates are slow (i.e. few hundred angstrom per minutes) if they are compared with chemical etching; the use of a magnetron can improve the speed of erosion;
- the non selectivity of the process makes critical the choice of the mask;
- low gas pressure are required to obtain sufficiently high impact energy (decreasing in the mean free path (λ_i) of the ions);
- large ions currents can be obtained increasing the pressure, at the price of a reduced anisotropy due to the randomization of ion direction by collisions.

General aspects of the physical etching

The fidelity in the pattern transfer into the substrate is determined by phenomena due to the plasma conditions. The phenomenon of faceting of the mask corner occurs at the angle of maximum etching rate for the mask. The ions etch faster at the corner resulting in rounded corner even if the mask edges are vertical. It is due to the sputtering yield reliance on the angle at which ions are directed at the surface; for instance the etching rate for the resist has a maximum at an incident angle of 60° . The faceting can be

transferred to the substrate with a different angle that depends on the material; therefore it is minimized increasing the thickness of the mask (Fig. 4.10).

The ditching or trenching occurs if the edges of the mask are not completely vertical due to faceting or redeposition; the ions, colliding at a glancing angle with the sloping edges, produce a local increasing in the etching rate, leading to ditches next to the walls of the trench.

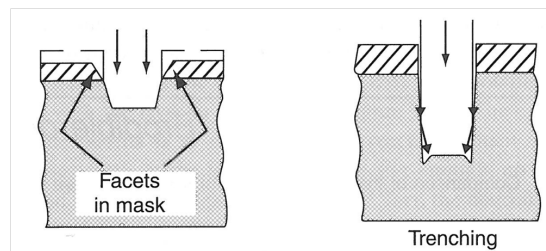


Figure 4.10: Phenomenon of Faceting and Trenching during etching a physical etching [41].

In the case of the sputtered materials are not suitably removed from the gas phase or they are not sufficiently volatile, a redeposition is observed on the sidewall of the mask and the etched trenches. The phenomenon is mainly localized on sloped sidewalls and becomes problematic in the case of high aspect ratios structures, which need adding reactive gasses for removing the material redeposited on the sidewalls (Fig. 4.11).

The collisions between the particles removed from the substrate and the gas phase species entail a specific material redeposition, that becomes significant at high pressure; moreover, it may involve contaminants from the walls of the vacuum chamber. Events of scattering in the sheath and nonuniformities in the field produce a distribution of impingements angles, which modifies the wall trenches obtaining the so-called hourglass shape.

Besides, some differences are observable between the etching of conductors and insulators. In the first case, the bending of electric field lines due to the surface topography enhances the ion flux at feature edges and produces the phenomenon of ditching. Charging effects appear processing insulators causing ion fluxes to the sidewall of the trenches and consequently a lateral etching and the hourglass shape are observed.

General aspects of the chemical etching

Differently from the physical etching, in the chemical etching processes the erosion of the material is obtained by chemical reactions of the different chemical species in the plasma with the substrate. The reaction products must be volatile in order to desorb easily from the surface to the gas phase. The process of chemical etching is summarized in the following steps (Fig. 4.12):

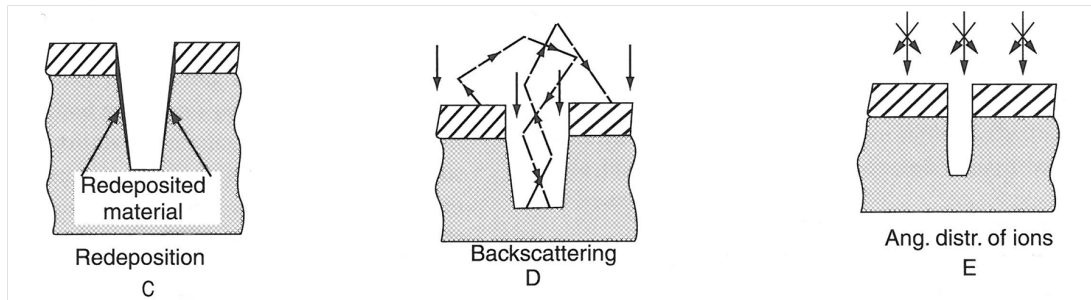


Figure 4.11: Redeposition, backscattering and angular distribution of incident ions phenomena during a physical etching [41].

- the formation of reactive chemical species by the collision of plasma electrons with gas molecules;
- the diffusion of the reactive species through the plasma, following by the adsorption on the surface;
- the reaction with the surface material;
- the desorption of the reaction products from the surface and diffusion in the gas phase.

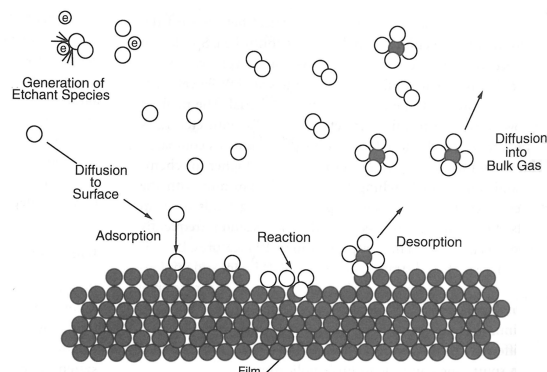


Figure 4.12: Process of chemical etching at the substrate surface due to the reactive species in the plasma [41].

The reactive species such as radicals are more abundant in the plasma than charged particles because of their higher generation rate due to a lower threshold energy (e.g. $< 8 \text{ eV}$); generally, they have a longer lifetime compared to the charged particles. The radicals and uncharged particles reach the surface by diffusion whereas the ions are accelerated towards the surface by the potential applied to the electrode underneath; therefore, the chemical etching does not entail the sputtering or milling of the surface and the damage of the surface is reduced. In dry etching, the number of the radicals in the plasma is in the same range as the number of atoms to be removed from the

substrate; therefore the supply of reactants limits the etching rate and small variations in flow rate or gas distribution uniformity may lead to etching rate nonuniformities. The so-called *microloading effect*, which is the dependence of etching rate on the size of the features, occurs either when the concentration of reactive species decreases because of the reactions with the surface material or when the area exposed to the etching increases. The loading effect entails a variation in the etching rate and it is more significant in the case of purely chemical etching; while it becomes smaller at lower plasma pressures. In order to avoid this phenomenon it is opportune to process substrate with similar surface area and to optimize the flow of gas species in the reactor. Two parameters must be controlled: the factor (U) and the residence time (τ).

- U ratio of rate of etching products formation to the rate of etching gas flow ($U \geq 0.1$ suggested for uniform etching);
- $\tau = PV/F$; V reactor volume in litres, P steady state pressure in Torr, F flow rate of the feed gas in Torr-Litres.

All these aspects have to be well present in mind when a process needs to be finally optimized, typically SEM inspections results fundamental to develop an etching process.

Chapter 5

Fabrication of the samples

In the introduction of this thesis it has been explained that for the planned wetting studies there was the need to fabricate substrates characterized by extended nanostructured surface areas with a high uniformity. To test the recent theoretical predictions (remind to chapter 2) concerning the capillary condensation in capped capillaries it has been developed a fabrication methodology that relies on UV-lithography, thermal nanoimprint lithography (NIL), wet etching and plasma etching in an inductively coupled plasma (ICP). These lithography techniques allow to pattern an area of about 1 cm^2 with a high density of rectangular channels of high aspect-ratio and to obtain many substrates for the measurements, which were different for the width and depth of the channels.

In this chapter the nanostructured silicon substrates are classified according to their different period $4 \mu\text{m}$, 500 nm , 180 nm and the fabrication methodology will be explained in detail.

5.1 Rectangular channels with a period of 4 micron

UV-lithography was used to pattern a photoresist deposited on a silicon substrate of surface area higher than 1 cm^2 and then to transfer the pattern into the substrate by dry etching using the resist as mask. This solution was not the optimal choice for our purpose because the resolution of the proximity UV-lithography tool available in the laboratory is close to $1 \mu\text{m}$ while the width of channels had to be much smaller than that limit. Furthermore, the selectivity of the process and the dimensional control of the fluorine based plasma etching process with resist mask could not ensure a good pattern transfer with lines with vertical sidewalls of 500 nm height. Therefore, the patterned polymer was not used to obtain directly the samples for the wetting measurements; it was required the fabrication of an intermediate stamp with narrow lines. The transfer of the stamp features by thermal nanoimprint lithography and the following plasma etching produced silicon surfaces patterned with rectangular channels of 500 nm width

and $1\ \mu\text{m}$ depth that were mounted in the wetting measuring system.

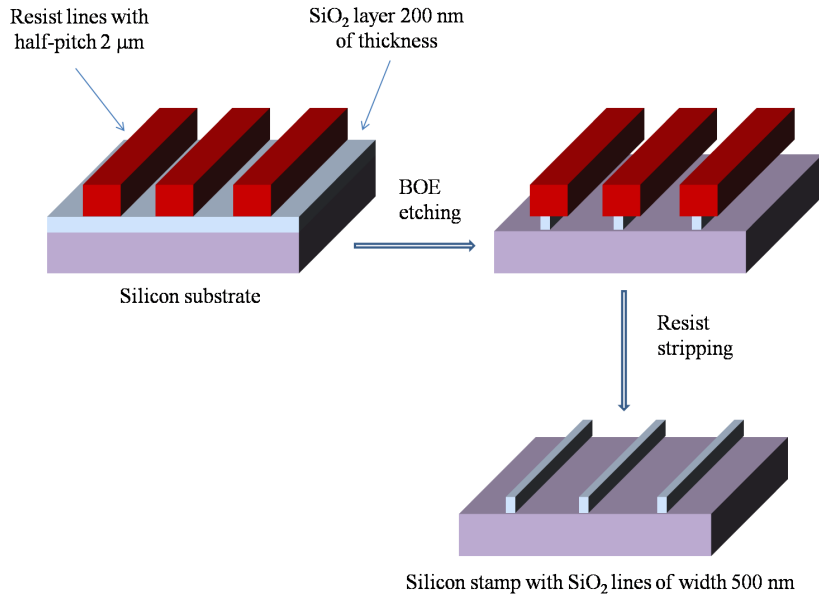


Figure 5.1: The figure outlines schematically the fabrication process of the silicon stamps narrowing the width of the SiO_2 lines on the surface by dipping in BOE etching solution.

The fabrication of the stamp started with the deposition by spin coating of a UV positive resist named S1813 (Rohm and Haas) on the substrate surface. The substrate was silicon with a silicon dioxide layer (200 nm of thickness) thermally grown (see Fig. 5.1); its surface had been previously dehydrated on a hot plate for 30 min at 200°C and a hexamethyldisiloxane (HMDS) layer was spun on the surface in order to improve the resist adhesion. After the baking on hot plate at 115°C for 1 min, the polymer layer was exposed to UV-light through a photolithography mask (area $2 \times 2\text{ cm}^2$) with a grating of chromium lines with a half-pitch of $2\ \mu\text{m}$. After developing the photoresist in MF 319 solution (Rohm and Haas), lines in polymer resulted on the surface and the following baking in oven at 115°C for 30 min was introduced to improve the adhesion of polymer to SiO_2 surface during the dipping in the so-called BOE solution (Buffered Oxide Etch solution). The samples were dipped in BOE solution for 10 min to narrow the silicon dioxide lines using the resist as wet etch mask; the etching was precisely calculated in order to obtain lines of a well defined width. The solution etches isotropically the SiO_2 with a rate of $80\text{ nm}/\text{min}$, while the dissolution rate of silicon was not significant considering the brief time of dipping. The resist stripping in acetone revealed a grating of silicon dioxide lines with an optimal uniformity on the overall surface; the width of the lines was of $500 \pm 50\text{ nm}$ and the thickness was 200 nm. The Fig. 5.1 is the scheme of the stamp production process and the table 5.1 outlines the process in detail.

Substrate	SiO_2 layer of 200 nm on silicon
Dehydration on hot plate	30 min at 200° C
Adhesion layer	HMDS coating
Photoresist	S1813
Layer thickness	1 μm
Baking on hot plate	1 min at 115° C
Lithography mask	grating of lines with half-pitch 2 μm
Exposure time	16 sec
Developing time	80 sec in MF319 developer
Baking in oven	30 min at 115° C
BOE etching	10 min

Table 5.1: Steps for the fabrication of silicon stamps with a grating of SiO_2 lines on the surface. The lines were 500 nm wide and 200 nm high with a period of 4 μm .

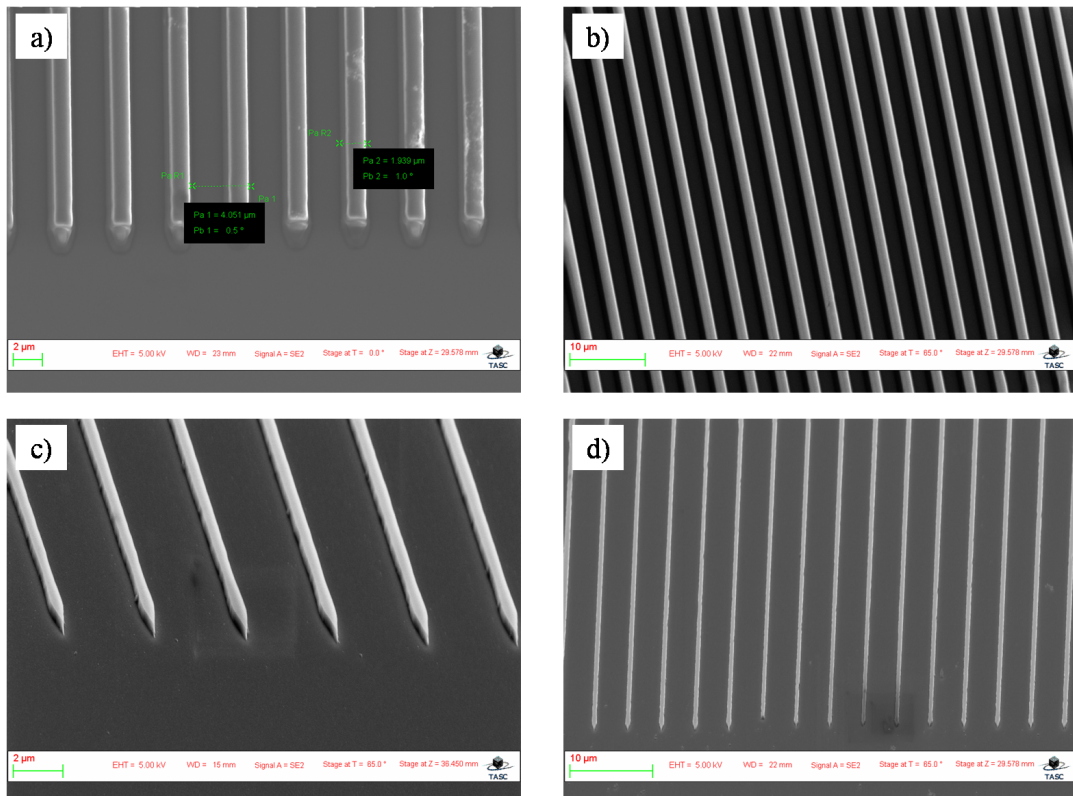


Figure 5.2: (a,b), SEM images of photoresist S1813 patterned by UV-lithography through a photomask with a grating of lines with a half-pitch of 2 μm . (c,d), SEM images of the SiO_2 lines obtained after the underetching in BOE solution using the resist of (a,b) as mask.

The Figures 5.2(a,b) show SEM images of the resist lines with half-pitch of $2\ \mu\text{m}$ produced by UV-lithography, while the Figures 5.2(c,d) are SEM images of the silicon dioxide lines obtained by dipping in BOE etching solution. The lines in this stamp were greater than $500\ \text{nm}$ of width because the etching time was lower than $10\ \text{min}$ and were obtained during the process development. The best result regarding the width, the uniformity and roughness of the lines was achieved with the stamp we identify with the name *Q* that is shown in Fig. 5.3. The oxide lines was obtained by isotropic etching

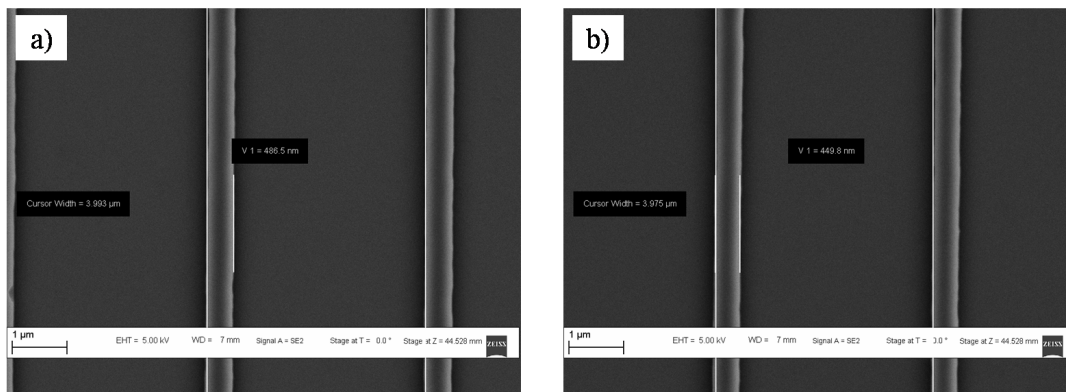


Figure 5.3: Silicon stamp of area $4\ \text{cm}^2$ named *Q*. SiO_2 lines, $500 \pm 50\ \text{nm}$ of width, $200\ \text{nm}$ of thickness and $4\ \mu\text{m}$ of period were fabricated on the surface.

in BOE, but since the lateral etching was much larger than the height of the lines, the resulting walls could with good approximation be assimilated to straight vertical walls. Further the coating of HMDS and the polymer hard baking at $30\ \text{min}$ were fundamental for the adhesion of resist lines to the surface during the dipping in etch solution allowing to obtain oxide lines with a low degree of roughness.

The *Q* stamp was used in a thermal nanoimprinting process to transfer the pattern into a resist and then into the silicon substrate below by plasma etching process in ICP. The stamp was cleaned in Piranha solution ($7\text{H}_2\text{SO}_4 : 3\text{H}_2\text{O}_2$) and coated with an anti-adhesive layer of Self-Assembled monolayer (SAM) in liquid phase by dipping in a $5\ \text{mM}$ solution of octadecyltrichlorosilane (OTS) in dodecane for 1 hour. A chromium layer of $100\ \text{nm}$ thickness was deposited by thermal evaporation on a silicon substrate with an area of $3 \times 3\ \text{cm}^2$. A resist for nanoimprint, MR-I 7020 E (Microresist), was spun on the substrate and baked for $2\ \text{min}$ at $140^\circ\ \text{C}$. Nanoimprinting process was performed with a hot press (P/O/Weber) at $140^\circ\ \text{C}$ for an imprinting time of $15\ \text{min}$ at a pressure of 50 bar. In Table 5.2 is described the imprinting process that was developed and adopted. The result was a polymeric grating characterized by rectangular channels $200\ \text{nm}$ deep and $500\ \text{nm}$ wide with a period of $4\ \mu\text{m}$.

Then, the samples were placed in an inductively coupled plasma (ICP STS-Surface Technology System) for a process in oxygen plasma in order to remove the polymer (i.e. residual layer) on the bottom of the channels revealing the chromium beneath

Substrate	silicon of area $3 \times 3 \text{ cm}^2$ with an evaporated chromium layer
Dehydration on hot plate	30 min at 200° C
Resist	MR-I 7020E
Layer thickness	250 nm
Baking on hot plate	2 min at 140° C
Stamp	Q
Imprinting temperature	140° C
Pressure	50 bar
Time at maximum temperature	15 min
Release temperature	40° C

Table 5.2: Steps for the imprinting of the silicon stamp Q into the MR-I 7020E polymer layer coated on a silicon substrate with a chromium layer on the surface.

(Table 5.3). Next, a dip in a chromium etch solution 200 g of $(\text{NH}_4)_2\text{Ce}(\text{NO}_3)_6$ + 600 ml of H_2O + 35 ml of CH_3COOH for 80 sec (etch rate of 80 nm/sec) removed the metal layer. After stripping the resist in acetone, the substrates were etched by a

Process		O2Strip
Coil	W	200
Platen	W	10
O_2	sccm	40
Etch rate	nm/sec	3
Pressure	mT	4
Valve	%	—
BIAS	V	—

Table 5.3: Plasma process developed in ICP based on oxygen gas for the etching of the polymer residual layer after imprinting.

fluorine based plasma in the ICP to transfer the pattern into the silicon using the metal as mask. The recipe developed for the etching (identified as 45MOD3) (Table 5.4) produced rectangular channels larger than 500 nm and depth $\approx 800 \text{ nm}$ as seen in Fig. 5.4. The final channel width was different in size with respect to the imprinted lines of polymer due to the additional enlargement of the feature of 100 nm on both sides of the channels caused by wet isotropic etching of chromium. Furthermore, a prolonged dip in the etch solution entailed the increase line edge roughness as seen in Fig. 5.4.

To avoid those problems (i.e. the enlargement of the channels and the increasing of the roughness), a new methodology was developed in order to provide samples of higher quality for the adsorption studies. In fact surface roughness introduces a morphologic component difficult to control that could entail wetting behaviors difficult to be taken into account by theory.

Process		45MOD3
Coil	W	400
Platen	W	50
SF_6	sccm	20
C_4F_8	sccm	40
O_2	sccm	30
Ar	sccm	0
Etch rate	nm/min	350
Pressure	mT	4
Valve	%	71
BIAS	V	175

Table 5.4: Test 45MOD3, fluorine based plasma process, used to transfer the pattern from the metal layer into the silicon.

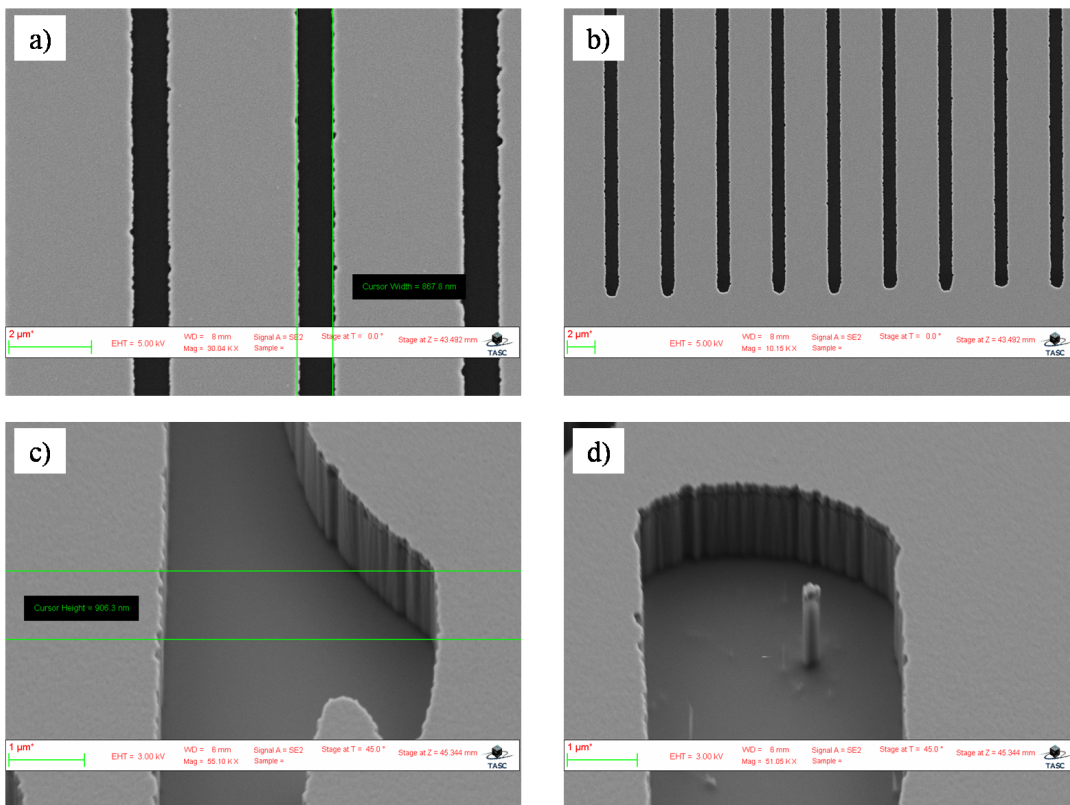


Figure 5.4: (a,b) top view of the silicon substrate patterned with rectangular channels using the method outlined in the Table 5.2; the roughness due to the wet etching process strongly affected the edge roughness of silicon. (c,d) show the characteristics of the wall surface; the roughness at the few nanometer scale of the chromium mask edge is transferred all the way down to the bottom of the feature in silicon from the mask to the bottom of the channel.

First of all, a chromium layer of thickness 20 nm was used as surface, then the imprinting process was performed again as described in table 5.2.

The difference from the previous method was in the process of residual layer removal by oxygen plasma. The samples were baked in oven for 5 min at 80°C, a temperature close to the T_g of 60°C in order to cause the smoothing of the resist lines and, at the same time, their lowering and enlargement. After the residual layer etching in oxygen plasma, the substrates were baked at a temperature of 90°C for 5 min to modulate the size of the resist lines. To etch the chromium layer they were dipped in the wet etching solution for a time of 30 sec; then by the test 45MOD3 the pattern was transferred into the silicon. As seen in Fig. 5.5(a,b) the metallic mask is patterned with channels of width less than 500 nm (size of the stamp features) because the width was modulated by the processes of polymer baking which also improved the adhesion to the metal surface. The optimal adhesion added to the minor thickness of the mask entailed a decreasing of the line roughness.

The samples shown in Fig. 5.5(c,d) depth \approx 800 nm were mounted on the measuring system and the collected adsorption isotherms will be described in the following chapter. A surface roughness of the walls close to the surface clearly visible in Fig. 5.5d was due to the minor etch resistance of the metallic mask in respect to the previous samples (Fig. 5.4) because the thickness was one-fifth (20 nm) of the previous mask.

5.2 Rectangular channels with a period of 500 nm and 180 nm

The fabrication methodology based on the use of thermal nanoimprint lithography and plasma dry etching was improved to fabricate gratings with smaller period and line width in respect to those of the first samples. For the fabrication of samples with gratings of high resolution lines of high aspect ratio, commercial gratings produced by interference lithography, purchased from AMO GmbH, have been employed as nanoimprint stamps. This choice has been made after many attempts with different types of stamps and processing conditions, that led to samples with rather large line edge roughness, which was judged as unacceptable for the purpose of accurate measurement of wetting phenomena and of an accurate comparison with the predictions of theoretical models. In particular two new types of grating stamps with lines of 250 nm in width, 500 nm period and 300 nm height (see Fig. 5.6(a,b)) the first and lines of 90 nm in width, 180 nm of period and 140 nm of height (see Fig. 5.9(a,b)) the second were employed. The technique of interference lithography allows to produce very uniform periodic patterns on large areas typically from few centimeter to up to 6 in in size.

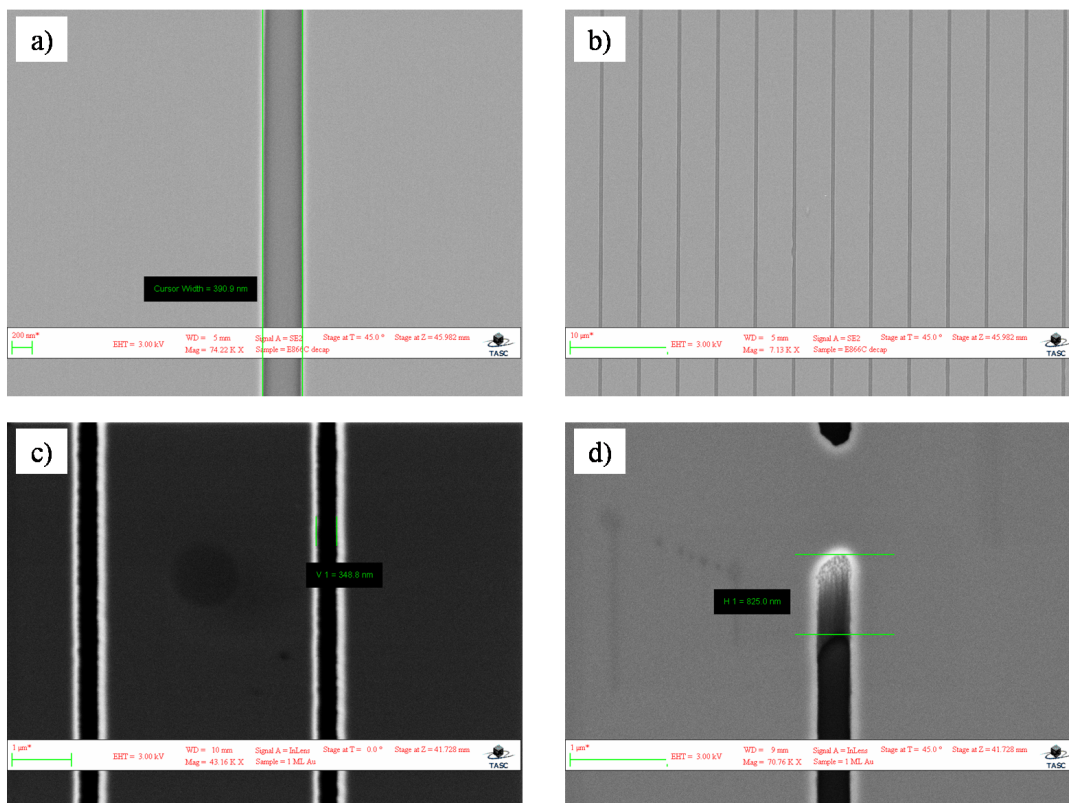


Figure 5.5: (a,b) metallic mask patterned with channels of width $400 \pm 30 \text{ nm}$ obtained by stamp *Q* imprinting and baking process to modulate the size of the channels. (c,d) the rectangular channels of depth $\approx 800 \text{ nm}$ were obtained by dry etching of the (a,b) samples with the 45MOD3 recipe. The surface roughness of the walls close to the surface is due to a not sufficient etch resistance of the chromium mask.

Rectangular channel with a period of 500 nm

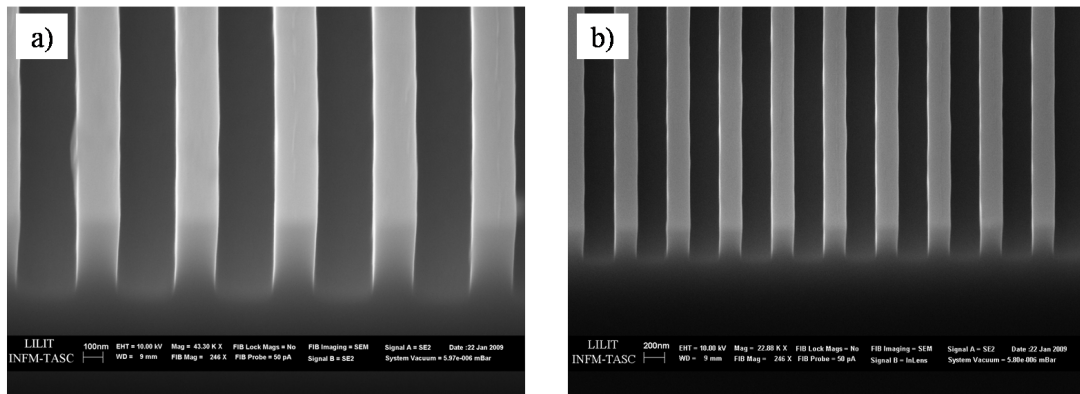


Figure 5.6: Silicon stamp *S500* made by interference lithography by the company AMO GmbH. The pattern consists of a grating of lines of 250 nm of width, 500 nm of period and 300 nm of height.

The main process steps for the fabrication of gratings with 250 nm lines and spaces (L/S) are briefly described below. An interference grating with 500 nm period on a surface area of $3 \times 3\text{ cm}^2$ was soaked in Piranha solution at 90°C for 30 min . After cleaning the sample, the stamp was rinsed in deionized water and dried in nitrogen stream. An anti-adhesive layer of Self-Assembled monolayer (SAM) was deposited in liquid phase by dipping the grating into a 5 mM solution of octadecyltrichlorosilane (OTS) in dodecane for 1 hour in inert atmosphere (nitrogen).

A double side polished silicon wafer was dehydrated for half an hour on a hot plate at 190°C . Then a first layer of lift-off resist PMGI SF3 (Microchem) was spin coated to a thickness of 70 nm and baked for 5 min at 190°C . A second layer of resist, specifically developed for nanoimprint lithography, the MR-I 7020E (Microresist) with a thickness of 170 nm was spun on the PMGI and baked for 2 min at 140°C . The imprint process of the stamp 500 nm was performed at the same conditions used for stamp *Q* as reported in Table 5.5.

After the release of the stamp, samples with grating pattern indented in the top MR-I 7020E layer were etched for 45 sec in a oxygen plasma (with process name *O2strip*) in the ICP for the removal of MR-I 7020E residual layer and vertical etching of PMGI-SF3 bottom layer (in Table 5.3 *O2strip* process parameter). The Fig. 5.7 shows the imprinted polymer lines after release of the stamp. Due to the good anisotropy of the plasma etching, the residual layer at the bottom of the imprinted channels and the PMGI SF3 underneath were etched without measurable reduction of the lateral size of the resist lines.

The rationale for adopting a double layer resist system in the preparation of the final samples for wetting measurements is to enable a reliable process of metal lift-off

Substrate	silicon of area $3 \times 3 \text{ cm}^2$
Dehydration on hot plate	30 min at 200° C
Resist	PMGI-SF3
Layer thickness	70 nm
Baking on hot plate	5 min at 190° C
Resist	MR-I 7020E
Layer thickness	170 nm
Baking on hot plate	2 min at 140° C
Stamp	S500
Imprinting temperature	140° C
Pressure	50 bar
Time at maximum temperature	12 min
Release temperature	40° C

Table 5.5: Sequence of steps for the imprinting of the silicon stamp S500 into a double layer resist system with a first layer of PMGI-SF3 and a second top layer of MR-I 7020E resist spun afterwards.

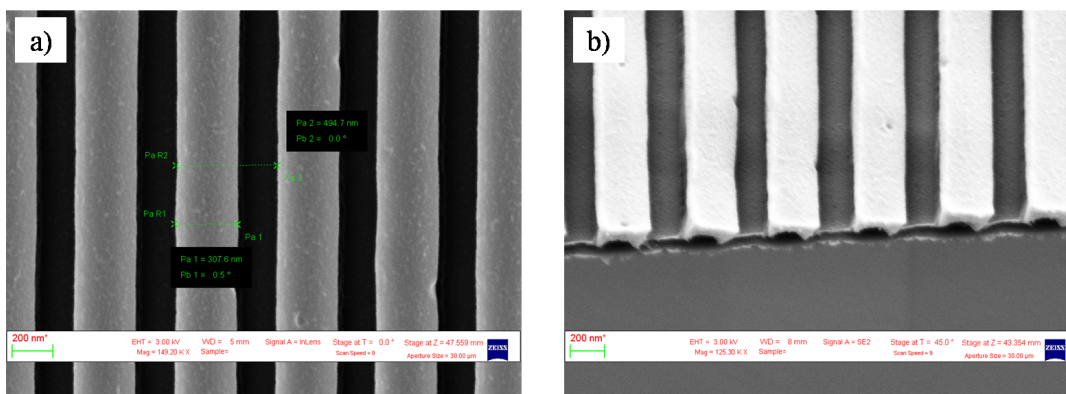


Figure 5.7: top (a) and tilted angle (b) SEM images of the indented MR-I 7020E on a bottom layer of PMGI-SF3, which remains unaffected by the process of imprinting due to the large difference in their glass transition temperature (65° C and 190° C , respectively).

in very narrow constrictions with metal thickness of 20 – 30 nm. Such thickness is required for masking the silicon substrate for anisotropic etching of trenches of 1 – 2 μm depth. Given the resolution of the features (below 100 nm), the Bosh process, based on the switching of the chemistry of the plasma to alternate sidewall passivation and etching, and suitable for very deep etching, was not suitable in our case, due to the formation of the so-called scallops, that would be detrimental for the measurements. The double layer resist system consists of a top layer acting as imaging layer (i.e. the layer that is directly patterned by nanoimprint lithography) and a second one acting as transfer layer (i.e. patterned through a process of pattern transfer from the top layer). Typically, the transfer layer is patterned during the wet development, which starts from the access regions represented by the areas from which the top layer has been removed. Such wet development in the case of the samples with high resolution structures required for wetting measurements was not feasible. The reason is that as a practical rule, for a reliable lift-off process the thickness of the transfer layer needs to be more than twice the thickness of the metal layer deposited. This corresponds to 60 – 70 nm of transfer layer. However, this represents a problem, for the specific case of the samples with 250 nm L/S and even more for those with 90 nm L/S , since developing the transfer layer in wet phase until break-through entails the formation of an undercut of 60 – 70 nm on both sides below the lines of the top layer. This means that the 90 nm wide lines would be lifted already during the development of the transfer layer. For this reason the break-through in that layer was obtained with an anisotropic oxygen plasma, followed by a few seconds of wet development, in order to perform reliably the lift-off process.

A nickel layer was deposited after the break-through of residual layer, to deposit a patterned hard metal mask as required for the silicon etching. In the case of samples with 250 nm L/S the undercut was obtained with a dip in the MF 319 solution for a maximum of 12 sec, which is the good compromise to produce a sufficient undercut of the PMGI without causing the collapse of the top layer. After rinsing with DI water and drying with nitrogen, the samples were introduced in an evaporator or, alternatively, in a RF-Sputtering for the deposition of a layer of nickel. The thickness of the metal layer was 20 nm. The metal lift-off was obtained by dipping the sample in the MF 319 solution leaving on the silicon surface a grating of metal lines. Finally, samples were placed in the ICP chamber for etching with a fluorine based plasma. At first, a milling process in an argon plasma was employed to improve the metal mask; then 400 W RF power was applied to the coil and 20 W to the platen for sustaining a plasma of a mixture of SF_6 , CF_8 , O_2 and Argon gases at a pressure of 8.0 mT. The silicon etch rate was 150 nm/min. Samples with different depths were obtained adjusting the etching time. The parameters of the etching process are outlined in detail in Table 5.6.

The subsequent cleaning in Piranha solution for 30 min resulted in the removal of

Process		Argon milling	MOD10AR4
Coil	W	400	400
Platen	W	30	20
SF_6	sccm	0	22
C_4F_8	sccm	0	45
O_2	sccm	0	10
Ar	sccm	30	5
Etch rate	nm/min	–	150
Pressure	mT	4	8
Valve	%		86
BIAS	V		95

Table 5.6: Test Argon milling for the improvement of the metal lines shape and test MOD10AR4 fluorine based plasma process, used to transfer the pattern from the metal layer into the silicon.

the metal mask. The images of Fig. 5.8 show the features produced in two substrates following used to measure adsorption isotherms.

Rectangular channels of period 180 nm

To replicate the pattern of the grating stamp S180 with 90 nm L/S and 140 nm height (Fig. 5.9) into silicon the same processes of NIL and plasma dry etching developed for the previous samples of period 500 nm were used. To obtain a nickel mask by lift off process was fundamental to calibrate the thickness of the polymer layers deposited and the time of dipping in MF 319 solution for the undercutting of the PMGI.

The PMGI SF2 GS was spun on the silicon surface and then it was coated with the MR I 7010E, both resists differ from those used for imprinting with the 259 nm L/S stamp grating for the lower concentration of polymer in the solvent. This allowed us to obtain polymer layers thinner as shown in Table 5.7. After the imprinting it was necessary to etch in oxygen plasma the residual layer of MR-I and also the PMGI beneath. The process time was reduced to 20 sec. Then, the dipping in MF 319 solution was drastically reduced to a maximum of 5 sec that was the limiting time for the formation of a sufficient undercut of the PMGI layer without lifting-off the lines. Also in this case the nickel layer was deposited by evaporation or sputtering. A metal layer of 10 nm showed a sufficient etch resistance in silicon plasma etching using the recipe MOD10AR4 to fabricate rectangular channels of depth of 1 μm . Some images of rectangular channels of width 90 nm and period 180 nm produced using the recipe MOD10AR4 are shown in Fig. 5.10.

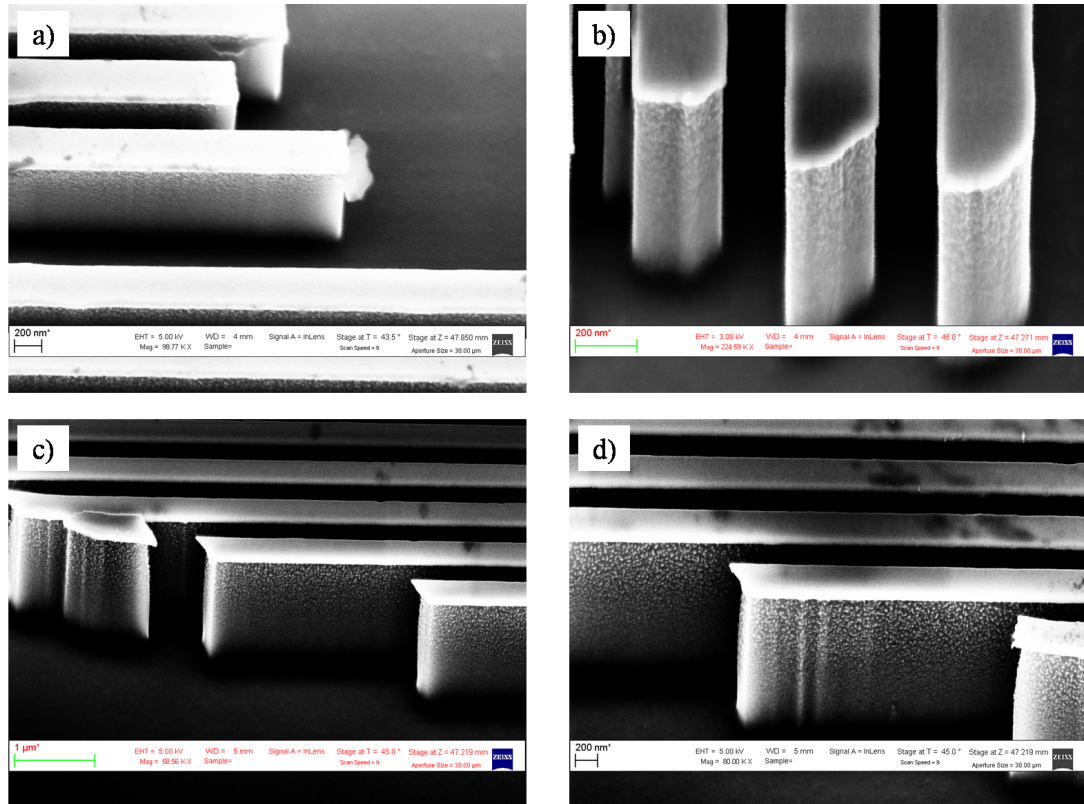


Figure 5.8: SEM images of two substrates patterned with rectangular channels of width 250 nm and period 50 nm fabricated using the recipe MOD10AR4; (a,b) the channels were depth 500 nm and in (c,d) the channel were depth 1, 2 μm.

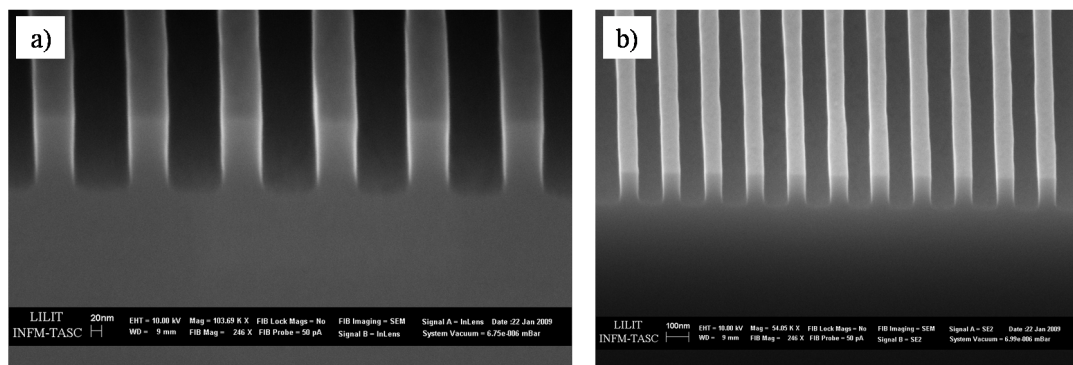


Figure 5.9: Silicon stamp named S180 made by interference lithography by AMO GmbH. The pattern consists of lines 90 nm of width, 250 nm of period and high 140 nm height.

Substrate	silicon of area $3 \times 3 \text{ cm}^2$
Dehydration on hot plate	30 min at 200°C
Resist	PMGI-SF2 GS
Layer thickness	50 nm
Baking on hot plate	5 min at 190°C
Resist	MR-I 7010E
Layer thickness	90 nm
Baking on hot plate	2 min at 140°C
Stamp	180 nm
Imprinting temperature	140°C
Pressure	50 bar
Time at maximum temperature	12 min
Release temperature	40°C

Table 5.7: Steps for the imprinting of the silicon stamp *S180* into a resist bilayer composed of a first layer of PMGI-SF2 GS coated on the silicon surface and a second top layer of MR-I 7010E resist spun afterwards.

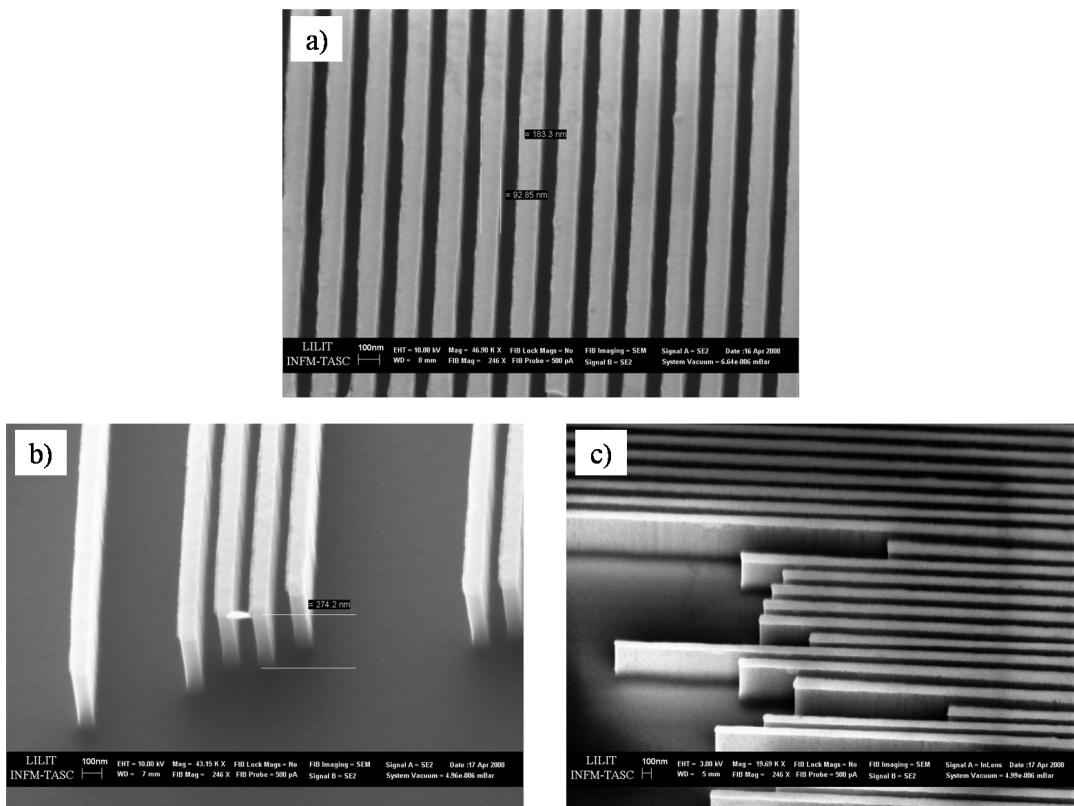


Figure 5.10: SEM images of two substrates fabricated with rectangular channels of width 90 nm, period 180 nm and depth 250 nm fabricated using the recipe MOD10AR4.

Critical issues in processes development

To develop the process methodology for the fabrication of the substrate patterned with rectangular channels with a period of 500 and 180 nm some critical issues have been faced and understood. We summarize them here:

- the preference of using a metal as etch mask for silicon plasma etching;
- the fabrication of the metal mask by lift off process;
- the difference between the properties and processing of metal mask by evaporation and by RF-sputtering;
- the improvement of the metal mask obtained by argon plasma milling;
- the use of argon in the mixture of gasses for the silicon etching(see Table 5.6).

The polymer of series MR-I 7000E used for thermal nanoimprint lithography did not withstand a prolonged silicon etching without loss of critical dimension and damages of the features. The argon in the mixture of gasses of recipe MOD10AR4 used to transfer the pattern into the silicon and a BIAS close to 100 V entailed a high degree of milling of the surface and consequently the damaging of the polymer mask.

The metal mask was produced by lift off process in order to avoid the wet etching of a metal layer deposited on the surface before the NIL process. As seen for the channel of period 4 μm chromium was used as hard mask because the wet etching solution did not contain reactants which could etch the polymer mask. Instead the wet etching solution for nickel contains $\text{HNO}_3 : \text{CH}_3\text{OOH} : \text{H}_2\text{SO}_4$; sulphuric acid decomposes the polymer and therefore cannot be used for pattern transfer with polymer mask.

A thin layer of nickel showed a better resistance in respect to chromium in the recipe for silicon etching; therefore it was decided to use nickel as mask material and a lift off process for the pattern mask definition.

A double layer of resists was used to create undercuts and facilitate the lift off process by ensuring that the metal coatings on top of the polymer and on the bottom of the trenches are disconnected. In Fig. 5.11a in a defective area the features in MR-I resist and the PMGI layer under the imprinted polymer are shown; the Fig. 5.11b is a SEM image of the polymer lines after stamp release. To obtain a well defined nickel mask by lift off the oxygen plasma was not limited to the removal of the residual layer, but was extended down to the full bottom layer of PMGI. By doing that, we could avoid the development of the total thickness of PMGI in its developer (MF 319), which entailed typically in the case of extremely narrow lines the lifting of the structures in the top layer. By anisotropic plasma etching of the full PMGI layer a sufficient undercut of few nanometers could instead be obtained by a final dip of few seconds in the developer solution.

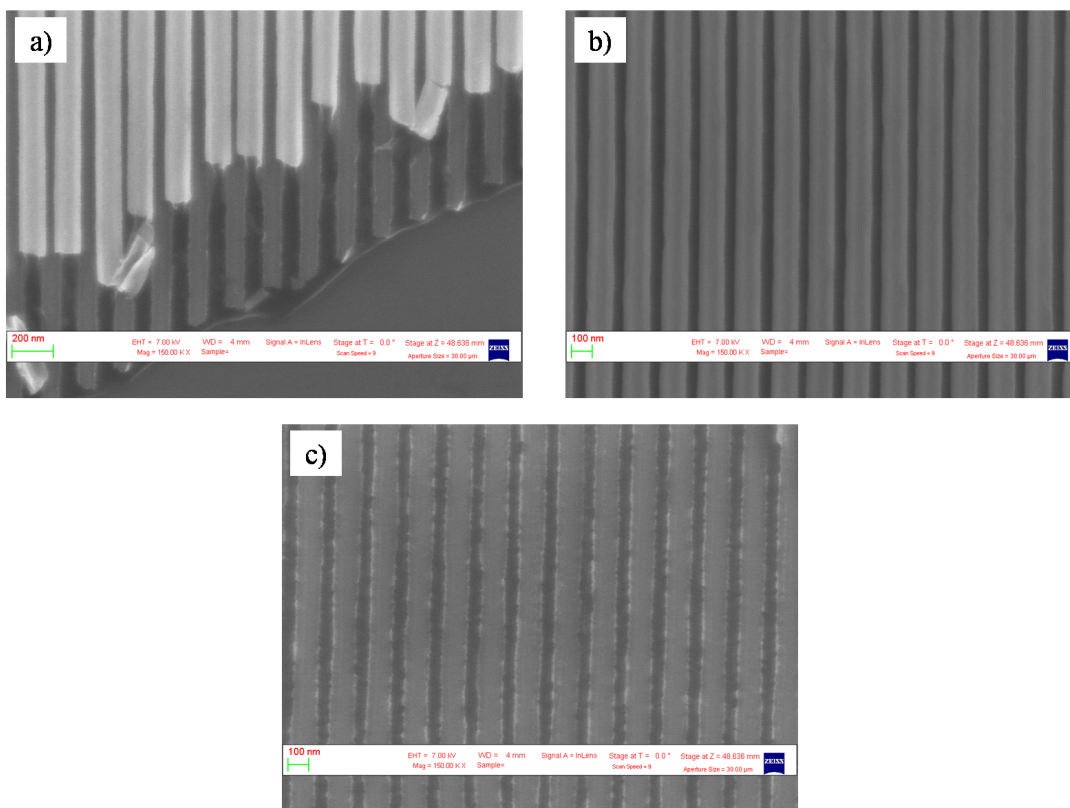


Figure 5.11: (a,b) SEM images of the MR-I imprinted lines of period 180 nm, in fig. (a) the underlayer PMGI is visible; in (c) the metal lines produced by sputtering evaporation and lift off performed in sonicator are shown.

Two different ways for depositing the nickel layer on the bottom of the rectangular channels were tested and both resulted in viable technological solutions. The first choice consisted in the use of an E-gun Evaporator and the second choice was the use of a RF-Sputtering. About the result of the processes, the main differences that we had observed were the following:

- The directionality of the deposition was controlled better in a process by evaporator than by RF-Sputtering (the mean free path of the atom in the deposition by evaporator was much longer). As a consequence, by evaporation, the metal line deposited on the bottom of the channel, even in presence of an undercut, does not spread out from the region of the geometrical shadow defined by the top layer of MR-I; on the contrary, with the RF-Sputtering we observed an enlargement of the nickel line with decreasing thickness from the center to the borders, due to the undesired deposition outside the geometrical shadow of the resist.
- The metal mask deposited by RF-Sputtering showed a roughness of the lines greater than the evaporated lines due to the larger size of the grains (Fig. 5.11). However, one reason that motivated also the use of sputtering instead of evaporation was the better adhesion of the film, which allowed to employ sonication.

The roughness observed in the case of lines with a period of 180 nm was less than that of the lines of period 500 nm; therefore sputter deposition was often chosen considering the difficulty to realize a lift off of lines width 90 nm without employing sonication that required a strong adhesion to silicon surface.

Moreover, by a first step of milling in argon plasma (see Table 5.6), it was possible to clean the region of penumbra from metal residuals, resulting in metal lines with well defined vertical edges. The milling process in the argon plasma, before the silicon etching, reduced the width of the metal lines removing the thinner borders, obtaining lines with an uniform thickness and a sharp vertical edge. In several tests, the metal mask fabrication by RF-sputter deposition and argon plasma milling maintained the critical dimension of the stamp features, with a bias of 10 nm at most in the lines width.

Finally, the silicon etching process was developed with the presence of argon in the gas mixture in order to increase both the effect of ion-bombardment of the surface and the fluorine radicals concentrations [43, 44].

Operating in the conditions of the recipe MOD10AR4, with a BIAS of ≈ 100 V, the anisotropic etching resulted in channels with a clean bottom, without the presence of the nasty effect that is known as grass formation and an improved surface roughness of the walls, as shown in Fig. 5.12. Figures (a,b) are rectangular channels of depth of 750 nm and (c,d) rectangular channels of depth of 1 μ m. The images are taken in defective areas to show the high degree of anisotropy of the etching. It is observed an increasing of the surface roughness in respect to the walls of the the features in Fig

5.10 because of the prolonged etching process, 7 *min* for the etching depth of 1 μm in respect to 3 *min* and 30 *sec* for the etching depth of 500 *nm*. The influence of surface

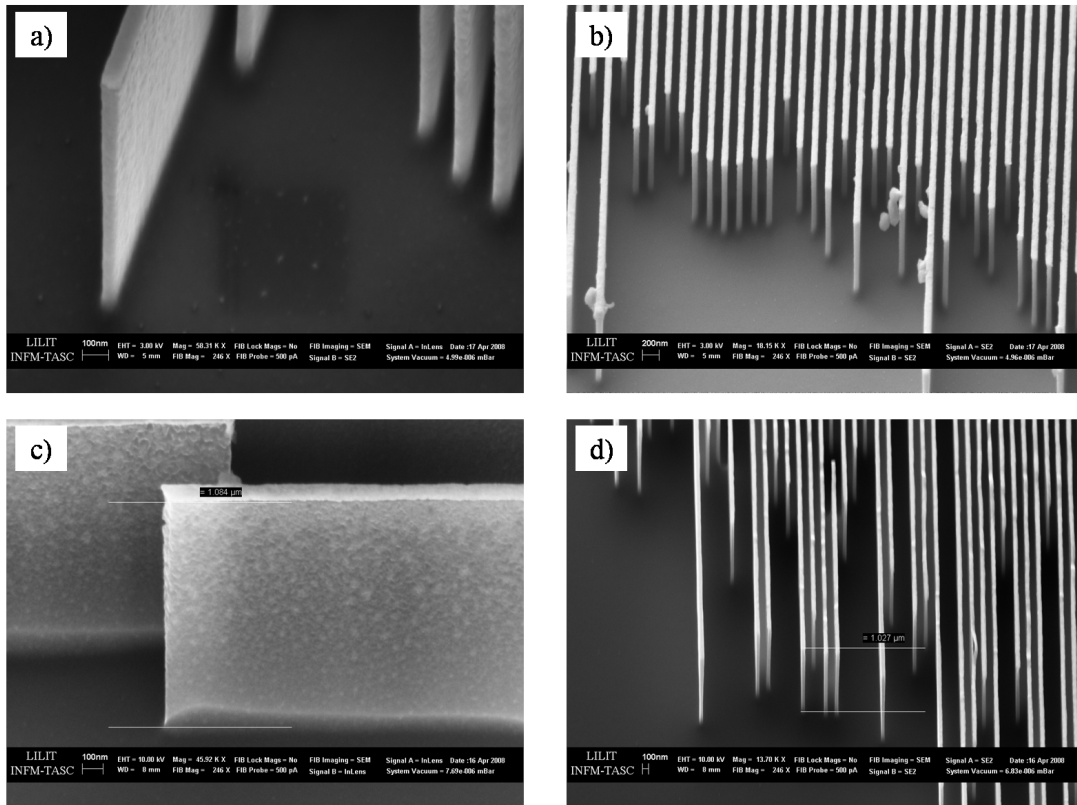


Figure 5.12: Rectangular channels produced by silicon etching with the recipe MOD10AR4; (a,b) channel depth is 750 *nm*, (c,d) channel depth is 1 μm .

roughness had been tested in the adsorption isotherms measurements, which will be described in the next chapter.

A critical issue of the fabrication process was the control of the features dimension. The motivation of that was the non uniformity of the lines width over all the 5 *in* area of the silicon stamp due to the process of fabrication. The width of the lines could vary of 10 *nm* in stamp areas at a distance of about 5 *cm*. Moreover the processes of lift off, as described, could induce an enlargement of the mask metal lines and consequently a reduction of the channels width. The processes of argon milling allowed to modulate the size of the metal lines cutting the thinner border produced by sputtering obtaining channels wider than that of the metal pattern. The best results about lines uniformity and roughness were obtained by evaporation of nickel ad argon milling of the metal pattern. The evaporated mask allowed deep etching of silicon without loss of critical dimension during the silicon etching obtaining features with aspect ratio of ≈ 11 as seen in Fig. 5.13(c,d). In the four images of Fig. 5.13 it is visible the poor degree of line roughness due to the evaporation of the metal and also the high uniformity of the features fabricated.

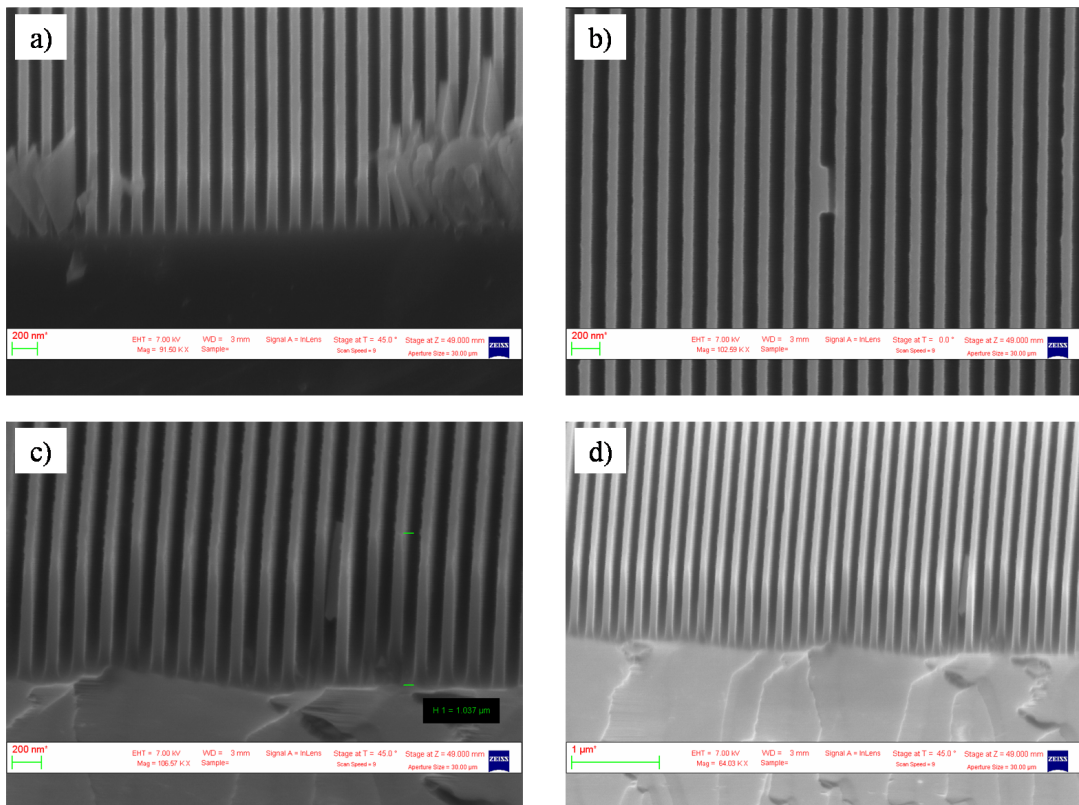


Figure 5.13: The small roughness and the high anisotropy of the etching process are shown by the SEM images of rectangular channel fabricated by evaporated nickel lift off and silicon plasma etching with the recipe MOD10AR4. (a,b) channels depth 500 nm, (c,d) channels depth 1 μm. The period and width of the features were well controlled during the lithography processes.

Chapter 6

Experimental results

The patterned substrates produced during this thesis have been used to verify the theoretical predictions concerning the phenomenon of capillary condensation (CC) introduced in the chapter of wetting. The substrates have been morphologically characterized by scanning electron microscope (SEM) in order to determine the width and depth of the rectangular channels fabricated. Then, the samples have been mounted on a torsional microbalance to measure adsorption isotherms which show the growth of the film mass condensed in the substrate wedges as a function of the pressure of the vapour in equilibrium with the film.

In this chapter the experimental setup is briefly introduced, the experimental data are presented and analyzed.

6.1 The experimental setup

The adsorption isotherms have been measured with a torsional oscillator [3]. The sample is attached using epoxy resin to the extremity of a hardened steel rod and is driven to the torsional resonant frequency of the system,

$$\nu = \frac{1}{2\pi} \sqrt{\frac{K}{I}} \quad (6.1)$$

where K is the elastic constant and I the total moment of inertia. A schematic drawing of the torsional disk oscillator used in the measurements is shown in Fig. 6.1.

As the substrate is exposed to a gas of density ρ and viscosity η , the resonance frequency changes because of a variation in the moment of inertia, ΔI . If I_0 and ν_0 indicate the moment of inertia and the resonance frequency in vacuum, respectively, then

$$\frac{\Delta I}{I_0} = \left(\frac{\nu_0}{\nu}\right)^2 - 1 \approx 2 \frac{(\nu_0 - \nu)}{\nu_0} \quad (6.2)$$

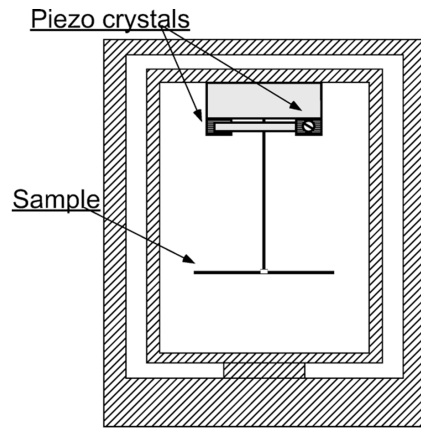


Figure 6.1: Schematic drawings of the torsional oscillator housed in the double-wall copper cell [3].

where the linearization is justified by the small relative frequency change during the measurements (typically much less than 0.1%). The relative increase $\Delta I/I_0$ is caused by the mass of the adsorbed film and by the hydrodynamic contribution due to the mass of the dynamically displaced fluid. In the case of a uniform disk of radius R , it is expected [45] that the frequency decrease due to this viscous coupling is equal to

$$\nu_0 - \nu = \frac{R^4}{4I_0} \sqrt{\pi \rho \eta \nu} \equiv C \sqrt{\pi \rho \eta \nu} \quad (6.3)$$

where C is a geometric factor independent of temperature. This correction has been evaluated by taking extensive vapour pressure adsorption isotherms of various rare gases at room temperature, where the only contribution of these substances to the frequency is caused by viscous coupling to the vapour.

In the case of the Si square substrates, the experimental points do not display a linear behavior, indicating that formula 6.3 does not provide an accurate description of the data. Therefore it has been used an extension of that formula:

$$\nu_0 - \nu = C \sqrt{\pi \rho \eta \nu} + c(\pi \rho \eta \nu) \quad (6.4)$$

where c depends on the gas investigated and may be temperature dependent.

The results of the some squares fits to the data according to 6.4 are indicated in the Fig. 6.2. The value of these constants deduced from these squares fittings of the experimental data for the three gases is in good agreement with each other (within 10%). Finally, it is made the reasonable assumption that in equilibrium conditions a homogeneous film covers the substrate, then $\Delta I_{film}/I_0$ is proportional to the film mass

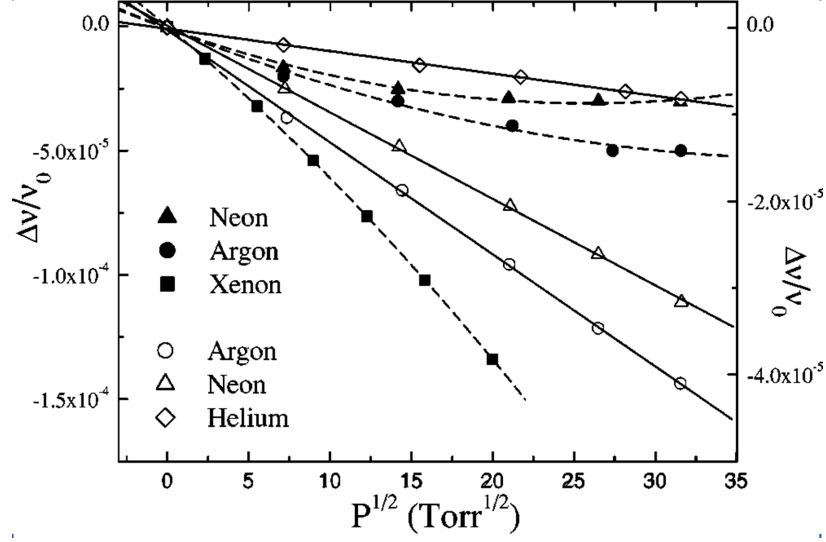


Figure 6.2: Isotherms of rare gases measured at 303 K in order to show the effect of the vapour on the resonant frequency of the oscillator. Full symbols represent the data taken with silicon squares while the empty are referred to metallic disks [3].

m_l . Therefore, in general, apart a multiplicative factor,

$$m_l \sim \frac{\nu_0 - \nu - C\sqrt{\pi\rho\eta\nu} - c(\pi\rho\eta\nu)}{\nu_0} \equiv \frac{\nu_0 - \nu^*}{\nu_0} \quad (6.5)$$

where ν^* represents the vapour corrected oscillator frequency.

The torsional mode is excited by means of a small piezoelectric crystal acting onto the extremity of a stainless steel arm hard soldered to the torsion rod (see Fig. 6.1). The oscillations are detected by a similar piezo mounted in a symmetric way with respect to the other one. The induced voltage is amplified by a low noise homemade amplifier and a lock-in technique locks the electronic circuit onto the resonant frequency of the microbalance.

The torsional oscillator is soldered onto a heavy brass disk 3 cm in diameter, which acts as a low-pass mechanical filter. The microbalance is mounted inside a double-wall copper cell to reduce thermal gradients. The maximum temperature difference between the top and bottom parts inside the inner copper cell is estimated to be less than a few μK . The temperature stability is better than 1 mK. To eliminate the pressure variations due to the daily oscillations in the temperature of the lab, we have placed the capacitance pressure gauge right before the cryostat. The open volume of the cell and of the sensor, which is kept at a constant temperature, can be sealed off from the gas system by means of a valve. In this way, the pressure reading is maintained stable within ± 0.05 Torr for many days.

The isotherms have been obtained measuring the adsorption of a liquid argon film at constant temperature of 85 K [4]. Argon was chosen as adsorbate because it com-

pletely wets most solid surfaces due to its low polarizability. Further it is very pure, characterized by simple van der Waals interactions and easy to thermocontrol by using a conventional liquid nitrogen cryostat.

6.2 Data analysis

The measured samples have been classified as seen in Tab. 6.1; the samples 4A and 4B were fabricated during my master thesis and were characterized by a period of $4 \mu m$ a channel width of 1.6 and $1.4 \mu m$ respectively and a depth of 7 and $5 \mu m$. The others samples have been fabricated during this PhD thesis as described in the previous chapter of fabrication.

Sample classification	Period	Channels width SEM characterization	Channels Depth
4A	$4 \mu m$	$1.6 \mu m$	$7 \mu m$
4B	$4 \mu m$	$1.4 \mu m$	$5 \mu m$
500	$500 nm$	$194 nm$	$500 nm$
180A	$180 nm$	$94 nm$	$750 nm$
180B	$180 nm$	$96 nm$	$750 nm$
180C	$180 nm$	$106 nm$	$1 \mu m$

Table 6.1: Substrates used for adsorption isotherms measurements. The samples classified as *4A* and *4B* have been produced during the master thesis [46] while the other ones have been produced in this PhD thesis as described in the chapter of the samples fabrication. The error of the SEM characterization of width and depth of channels has been estimated on the order of 4 %.

The adsorption isotherms measurements have been performed in the same conditions for each substrate. In the following we describe how the raw data frequency vs. pressure measured with the torsional microbalance are analyzed. The data refer to the sample classified as *500*.

In Fig. 6.3 the measured resonance frequency ν is plotted (black points) as a function of the argon vapor pressure P . As described in the previous section, the resonance frequency must be corrected by the hydrodynamic contribution of the vapour. The correction is obtained interpolating the measured data according to the equation 6.4 for $P \leq 200 Torr$. Below this value the contribution due to the adsorbed layer film can be neglected. Therefore the frequency variation is only due to the viscous coupling of the vapour. The continuous line shows the estimated vapour correction. The circles instead indicate the resulting frequency after the vapour correction.

The relative moment of inertia ($\Delta I/I_0$) is calculated using the equation 6.2 and the result is plotted (see Fig. 6.4) as a function of the relative pressure defined as the ratio between the measured pressure and the corresponding pressure for bulk saturation.

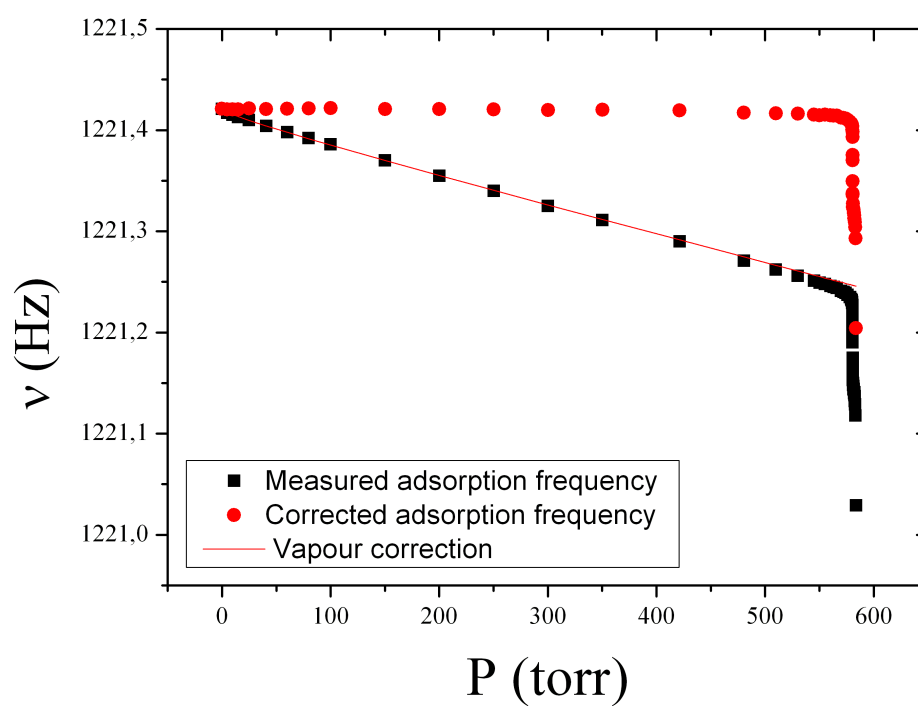


Figure 6.3: Adsorption isotherm (black squares) of argon measured at a temperature of 85 K on the substrate classified as 500, characterized by a surface patterned with rectangular channels of width 194 nm and depth of 500 nm. The red line represents the estimated vapour correction and the red circles are the resulting frequency after vapour correction.

The isotherm measured adding gas to the cell (adsorption) and removing gas from the cell (desorption) is fully reversible and a sharp rise is observed very close to bulk saturation. That jump is due to capillary condensation in the rectangular wells.

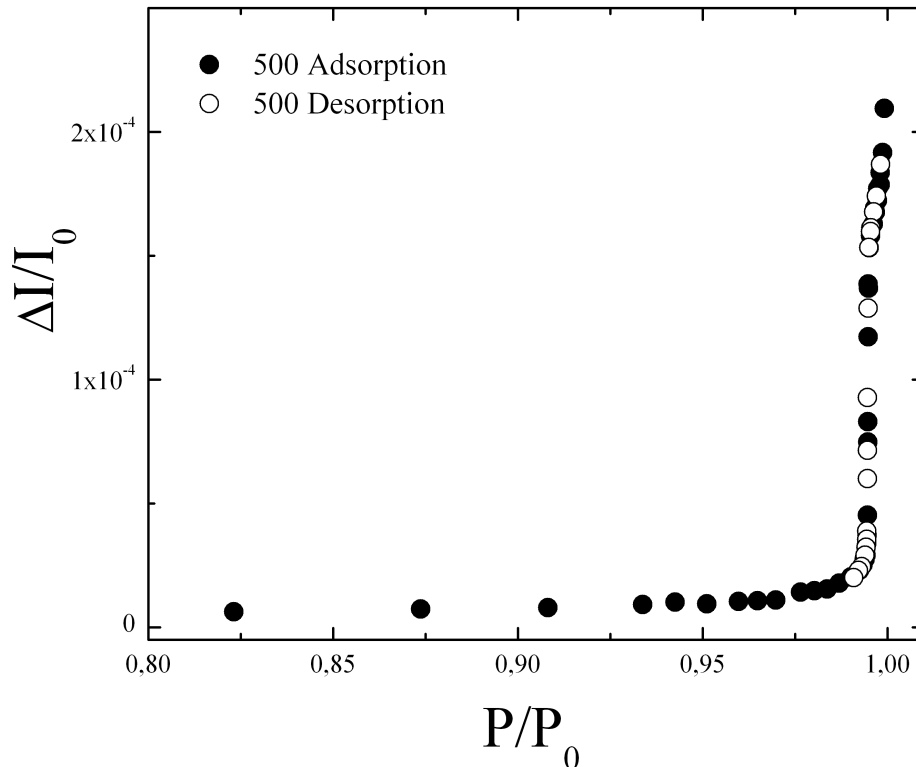


Figure 6.4: Adsorption and desorption isotherms measured on the sample 500. The relative moment of inertia is plotted as a function of the relative pressure. There is not any visible hysteresis loop.

In fact, Fig. 6.5 shows representative isotherms measured in samples of three different widths : 106 nm , 194 nm and $1.6\ \mu\text{m}$ for the samples *180C*, *500*, *4A* respectively.

It appears evident how the position of the capillary rise is strongly dependent on the channels width: as the width becomes smaller, the jump occurs at lower relative pressures. The observed pronounced difference in the size of the jump (seeing the vertical axis) is due to the different mass adsorbed in the substrates and simply reflects the different depth of the channels. The sample *4A* patterned with the deepest channels ($7\ \mu\text{m}$) adsorbed more mass than the other ones.

Fig. 6.6 shows an enlargement of the capillary rises observed on samples patterned with rectangular channels of nominal width $1.6\ \mu\text{m}$ and $1.4\ \mu\text{m}$ respectively. However, the fact that the two jumps are practically coincident suggests that the mean width of

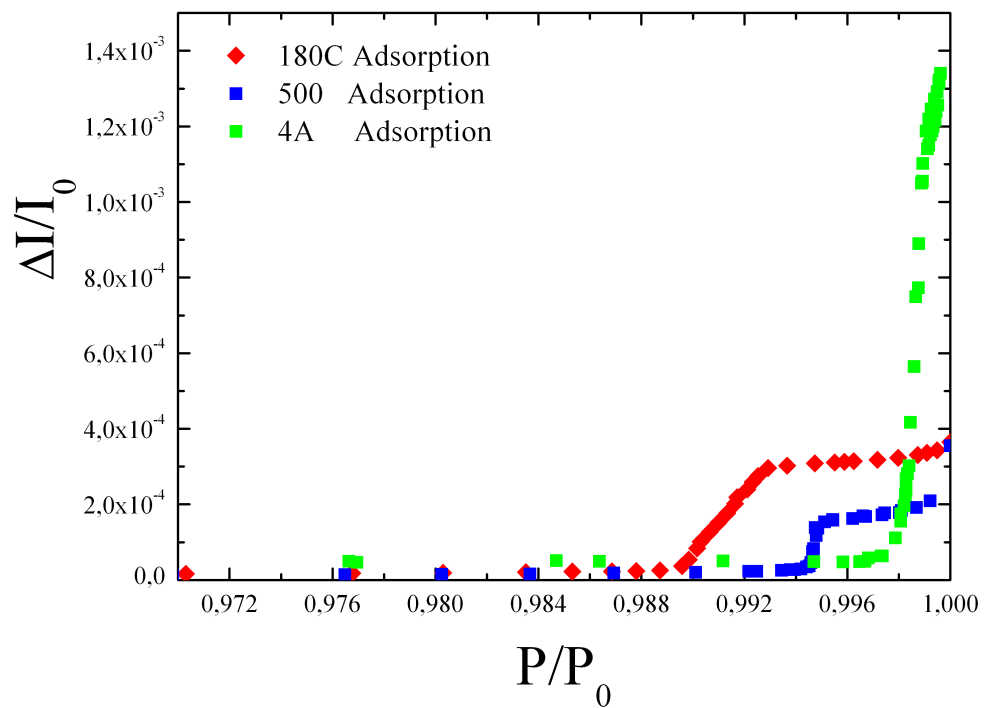


Figure 6.5: Adsorption isotherm on three different substrates: 4A (channel width $1.6 \mu\text{m}$), 500 (width 194 nm) and 180C (width 106 nm). The condensation occurred in different position due to the different width of the rectangular channels. Further, the greater jump of the sample 4A is due to the depth of the features, which were at least 7 times deeper than the other ones.

the two samples is practically the same, in contrast to the local determination carried out with the electron microscope which probes only a very limited area of the sample.

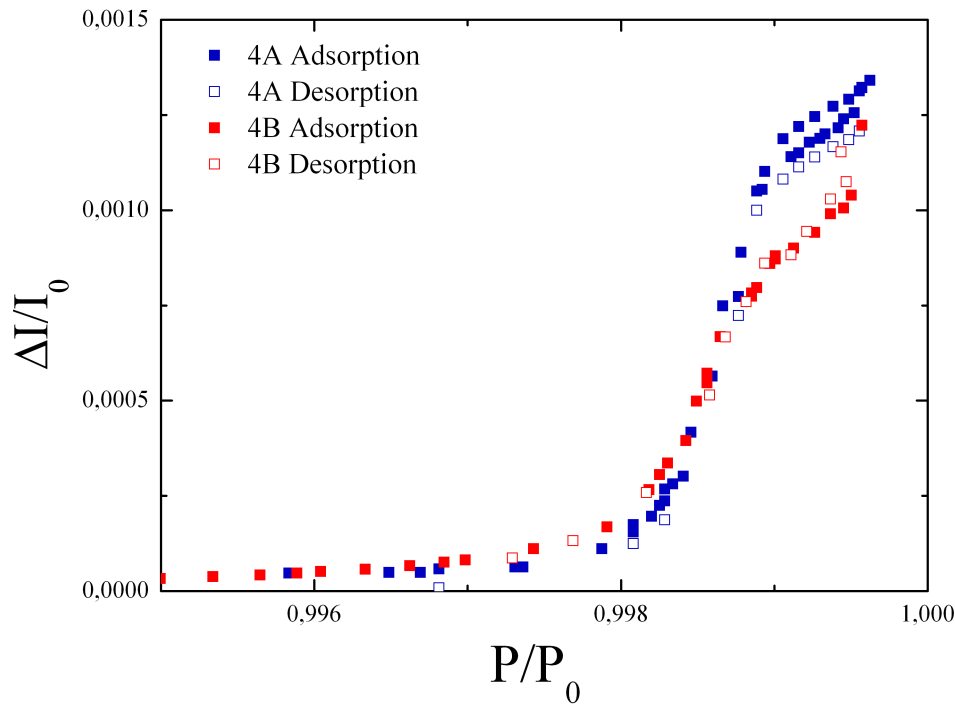


Figure 6.6: Adsorption isotherms measured on the samples 4A and 4B characterized by a surface patterned with rectangular channels of width 1.6 and 1.4 μm micron respectively.

Fig. 6.7 shows in detail as the position of the frequency jump is related to the width of the fabricated channels. In the sample 500 having the largest channels the capillary condensation occurs closest to the bulk saturation. Again, there is a nice overlap of curves belonging to the substrates 180A and 180B, an indication of a good control in the fabrication process reproducibility, as also confirmed by SEM measurements. The jump of sample 180C is larger because the wells are deeper.

In Fig. 6.8 the curves have been normalized to the value just above the completion of the capillary step to facilitate a direct comparison. The curves taken with the samples classified as 180 do present some differences. The most evident is a slight horizontal shift between the two curves taken on the samples 180A and 180B, due to the different width. There are also some strange features whose origin is still unknown. The curve measured on the sample 180A shows a change of slope, somewhat of a saddle point in the middle of the step, but no hysteresis between adsorption and desorption. Instead, the rise of the 180B isotherm is smoother and on this scale, it resembles a linear curve;

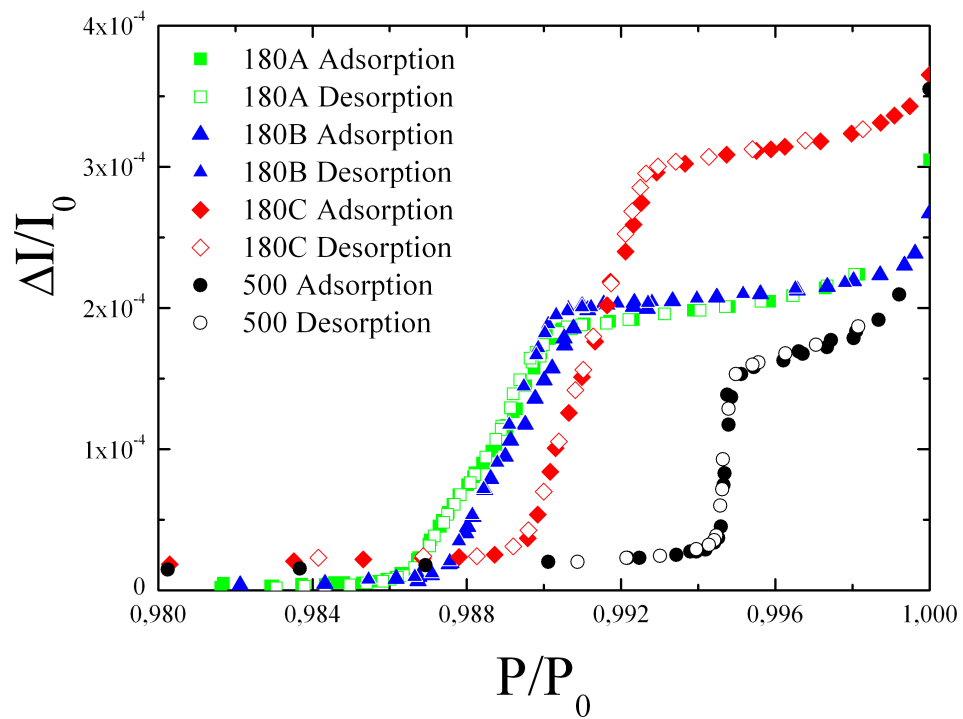


Figure 6.7: Adsorption and desorption isotherms measured on the samples so-called *180A*, *180B*, *180C* and *500*. They are patterned with rectangular channels of width 194 nm, 94, 96, 106 nm respectively (SEM characterization).

but the adsorption and desorption branches have different slopes, thus producing a small hysteresis loop.

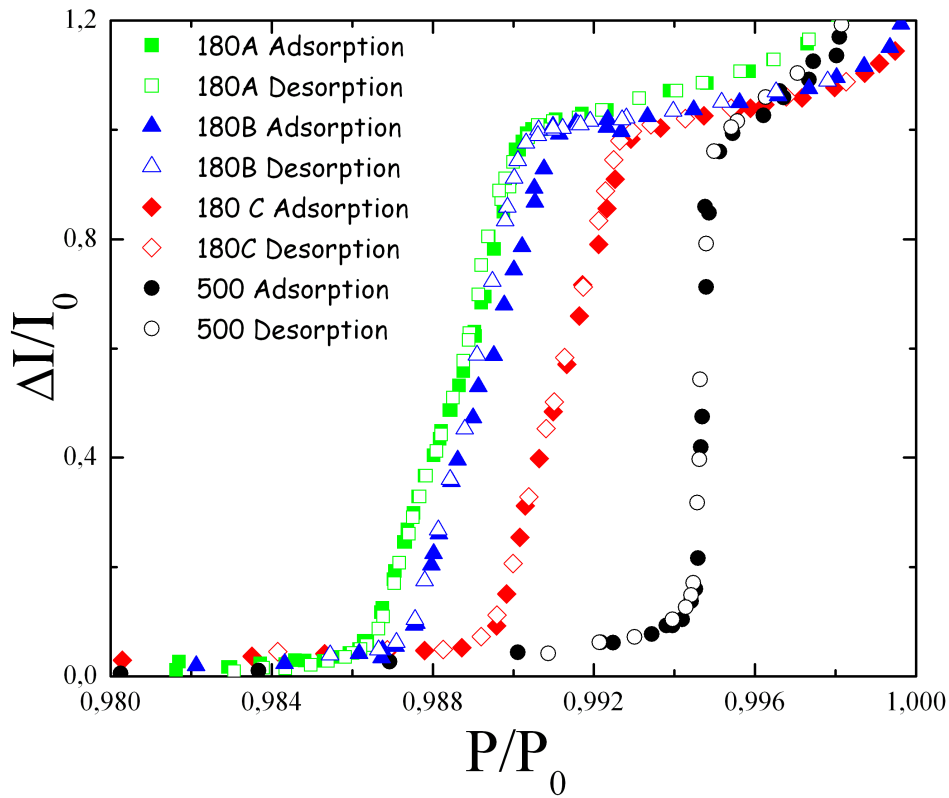


Figure 6.8: The adsorption and desorption isotherms measured on the samples classified as 180A, 180B, 180C and 50 have been normalized in order to allow a better analysis.

These tiny features are reproducible so that they cannot be ascribed to instrumental artifacts during the measurement. They are more likely caused by some morphological defects in the samples, like the presence of rough walls near the top of the wells or differences in the pore width. Further, the curves show a very steep capillary rise, but not vertical, may due to a finite pore size distribution.

The curves taken on the samples classified as 180 and 500 have been analyzed in terms of the classical Kelvin equation [47]:

$$\Delta\mu \equiv \mu - \mu_{sat} = K_B T \ln \left(\frac{P}{P_0} \right) = - \frac{2\sigma}{(n_l - n_g)W} \quad (6.6)$$

Where μ_{sat} the chemical potential for the bulk saturation K_B is the Boltzmann's constant, $\sigma = 11.3 \text{ dyna/cm}$ is the surface tension of liquid argon at the temperature of

$T = 85 \text{ K}$, $n_l = 2.1 * 10^{22} \text{ atoms/cm}^3$ is the corresponding liquid number density and the n_g is the density of the gas argon. As a pressure P for the capillary condensation is chosen the value at half jump.

Sample classification	500	180A	180B	180C
SEM characterization	194	94	96	106
Channels W (nm) classical Kelvin's equation	175	81	84	100
Channel W (nm) corrected Kelvin's equation literature Hamaker constant	190	90	93	109
Channel W (nm) corrected Kelvin's equation experimental Hamaker constant	185	93	96	112

Table 6.2: The width of the channels is derived from the adsorption isotherms data applying the classical Kelvin's equation 6.6 or the corrected Kelvin's equation 6.7, which takes into account the thickness of the adsorbed layer onto the vertical walls. The thickness is calculated with the FHH equation 6.8 and depends on the Hamaker constant for the system silicon-argon. The Hamaker constant was obtained either from the analysis of adsorption isotherms on a flat silicon surface (experimental constant) or in literature [48].

The width of the channels can be obtained also using the corrected Kelvin equation which takes into account the thickness t of an adsorbed layer onto the vertical walls:

$$\Delta\mu \equiv \mu - \mu_{sat} = K_B T \ln \left(\frac{P}{P_0} \right) = - \frac{2\sigma}{(n_l - n_g)(W - 3t)} \quad (6.7)$$

The latter quantity $W - 3t$ can be derived by the Frenckel-Halsey-Hill isotherm equation:

$$- \delta\mu = \frac{H}{t^3} \quad (6.8)$$

Where H is the Hamaker constant of the system silicon-argon. The Hamaker constant value can be taken from the literature, $H = 2.0 * 10^{-36} \text{ erg cm}^3$ [48]. Further the Hamaker constant can be estimated directly by measuring an adsorption isotherm of argon on a flat silicon sample which underwent the same surface treatment of the patterned silicon samples. In our case, to this purpose, double side polished silicon wafers were treated on both sides with the same plasma etching process and Piranha cleaning in order to mimic the final chemical physical conditions of the surface of the nanostructured substrates.

The modification to the Kelvin equation was proposed by Cohan [49, 50]. It was

considered the presence of an adsorbed film onto the vertical walls; these layers tighten the size of the channel and, consequently, the capillary condensation occurs at a lower pressure. Therefore, considering the presence of this layer, the real width of the channels must be higher of that calculated with the classical Kelvin equation as seen in Table 6.2.

The film thickness can be estimated by the formula:

$$t = \sqrt[3]{\frac{H}{K_B T \ln\left(\frac{P_0}{P}\right)}} \quad (6.9)$$

We have estimated experimentally an Hamaker constant higher than the value taken in literature, although it is affected by a consistent degree of uncertainty due to the analyzing of the data. Indeed in the table 6.2 we show the channel width calculated with the corrected Kelvin equation using both Hamaker constants, that experimentally estimated by us and that taken from the literature.

The results show that the values calculated with the corrected Kelvin equation nicely agree with those obtained by SEM characterization. Therefore it can be suitable considering the influence of the adsorbed film layer onto the walls on the capillary condensation phenomenon, in particular for channels of width ranging to $\approx 200 \text{ nm}$.

Chapter 7

Conclusions and perspectives

The goal of this Ph.D. thesis was the study of capillary condensation in nanostructured surfaces. To test recent scaling theories dealing with the capillary filling, several substrates patterned on the surface with rectangular channels of different width and depth have been fabricated. The fabrication of these samples has required the development of a suitable methodology which relied on nanoimprint lithography (NIL), wet etching, (Buffered Oxide Etch solution) and plasma etching in an Inductively Coupled Plasma (ICP). With our optimized process we were able to pattern extended surface areas of about 1 cm^2 with a regular array of rectangular channels or hemispherical holes of nanometric size. In particular, we realized channels of two different widths (90 and 200 nm) and characteristic depths varying from 0.5 to 2 μm . With a torsional microbalance we have measured Argon adsorption isotherms on these patterned samples. The curves showed pronounced and sharp jumps related to the capillary condensation in the wells. The jumps display the following features:

- the condensation occurs at a pressure lower than the value corresponding at bulk liquid-vapor saturation;
- the condensation pressure depends on the width of the channels ($P_{co}(L)$) and is found to agree with the predictions of the Kelvin equation;
- the jump is reversible, i.e. no pronounced hysteresis is observed during adsorption and desorption.

This study represents the first experimental confirmation of the validity of the macroscopic Kelvin equation for rectangular wells of nanometric size. The curves are currently under analysis by Prof. Parry and co-workers to see whether they confirm his theoretical predictions. Another interesting result of this study was the demonstration that adsorption isotherms can be a powerful method to characterize the morphology of patterned surfaces on extended areas, much more efficient than any electron microscopy, which necessarily probes only limited areas. An important follow-up of this

work is the study of capillary condensation in cylindrical pores of nanometric to verify a recent geometrical covariance scaling law and in hemispherical cups, where the spatial confinement is expected to show interesting and new adsorption phenomena.

Appendix A

Curriculum vitae

Appendix A

Curriculum vitae

05th October 1978 Born in Dolo, Italy.

24th November 2004 "Laurea" degree in Material Science.

2009 Ph.D. in Materials Science and Engineering.

Publications

A. Pozzato, S. Dal Zilio, G. Fois, D. Vendramin, G. Mistura, M. Belotti, Y. Chen, and M. Natali
Superhydrophobic surfaces fabricated by nanoimprint lithography.
MICROELECTRONIC ENGINEERING, 83:884, 2006

A. Qazi, D. Nonis, A. Pozzato, M. Tormen, M. Lazzarino, S. Carrato, and G. Scoles.
Asymmetrical twin cantilevers for single molecule detection.
APPLIED PHYSICS LETTERS, 90:173118, 2007

L. Brigo, M. Natali, M. Pierno, F. Mammano, C. Sada, G. Fois, A. Pozzato, S. dal Zilio, M. Tormen, and G. Mistura.
Water slip and friction at a solid surface.
JOURNAL OF PHYSICS-CONDENSED MATTER, 20:354016, 2008

V. Toffoli, F. Esch, M. Melli, F. Cataruzza, A. Pozzato, S. Carrato, G. Scoles, M. Tormen, and M. Lazzarino.
Intrinsically aligned chemo-mechanical functionalization of twin cantilever structures.
NANOTECHNOLOGY, 19:445502, 2008

Publications in press

A. Pozzato, S. Dal Zilio, L. Bruschi, G. Mistura, and M. Tormen.

Fabrication of substrates with extended nanostructured surface areas for wetting studies.

MICROELECTRONIC ENGINEERING, SPEC. ISS., 2008

V. Toffoli, F. Esch, M. Melli, A. Pozzato, M. Tormen, and M. Lazzarino.

Chemical functionalization of atomically flat cantilever surfaces.

MICROELECTRONIC ENGINEERING, SPEC. ISS., 2008

G. J. Bakeine, J. Ban, G. Greci, A. Pozzato, S. Dal Zilio, M. Prasciolu, L. Businaro, M. Tormen, and M. E. Ruaro.

Evaluation of nano-scale surface topography as a tool in directing differentiation of embryonic stem cell derived neural precursors.

MICROELECTRONIC ENGINEERING, SPEC. ISS., 2008

G. J. Bakeine, A. Bertolotti, C. Zennaro, G. Greci, A. Pozzato, S. Dal Zilio, M. Prasciolu, L. Businaro, M. Alessiani, R. Nano, and P. Dionigi.

Design and fabrication of large area nano-structured substrates for use in pancreatic beta-cell engineering.

MICROELECTRONIC ENGINEERING, SPEC. ISS., 2008

Posters

September 16 - 19, 2008, MNE 2008 conference Athens (Greece). Poster titled: **Studies of wetting behaviour on nanostructured surfaces.**

A. Pozzato, S. Dal Zilio, G. Mistura, L. Bruschi and M. Tormen.

September 16 - 19, 2008, MNE 2008 conference Athens (Greece). Poster titled: **Local chemical functionalization of self-aligned twin cantilever structures with sub-nanometric control.**

V. Toffoli, F. Esch, M. Melli, A. Pozzato and M. Lazzarino.

September 16 - 19, 2008, MNE 2008 conference Athens (Greece). Poster titled: **Design and fabrication of large area nano-structured substrates for use in pancreatic beta-cell engineering.**

G. J. Bakeine, A. Bertolotti, C. Zennaro, G. Greci, A. Pozzato, S. Dal Zilio, M. Pras-

ciolu, Luca Businaro, M. Alessiani, R Nano, P. Dionigi.

September 16 - 19, 2008, MNE 2008 conference Athens (Greece). Poster titled: **Evaluation of nano-scale surface topography as a tool in directing differentiation of embryonic stem cell derived neural precursors.**

G. J. Bakeine, J. Ban, G. Greci, A. Pozzato, S. Dal Zilio, M. Prasciolu, L. Businaro, M. Tormen, M. E. Ruaro.

Schools

II scuola sui materiali molecolari per fotonica ed elettronica

Arbatax (Italy) - June 18 - 21, 2006.

PANAMA summer school (NaPa Project)

Toulouse (France) - July 3 -14, 2006.

NordForsk summer school: Polymer micro- and nano-fabrication

Parkhotell Palmse (Estonia) - August 31 to September 6, 2007.

ISOPHOS 2007 International School on Organic Photovoltaics

Ventotene Island (Italy) - September 23-27, 2007.

Bibliography

- [1] M. Tasinkevych and S. Dietrich. Complete Wetting of Nanosculptured Substrates. *Physical Review Letters*, 97:106102, 2006.
- [2] C. Rascón and A. O. Parry. Geometry-dominated fluid adsorption on sculpted solid substrates. *Nature*, 407:986, October 2000.
- [3] L. Bruschi, A. Carlin, A. O. Parry, and G. Mistura. Crossover effects in the wetting of adsorbed films in linear wedges. *Physical Review E*, 68:21606, 2003.
- [4] L. Bruschi, G. Fois, G. Mistura, M. Tormen, V. Garbin, E. di Fabrizio, A. Gerardino, and M. Natali. Complete wetting of curved microscopic channels. *The Journal of Chemical Physics*, 125:144709, 2006.
- [5] A. O. Parry, C. Rascón, N. B. Wilding, and R. Evans. Condensation in a capped capillary is a continuous critical phenomenon. *Physical Review Letters*, 98:226101, 2007.
- [6] L. Bruschi, A. Carlin, and G. Mistura. Complete Wetting on a Linear Wedge. *Physical Review Letters*, 89:166101, 2002.
- [7] T. Young. An Essay on the Cohesion of Fluids. *Philosophical Transactions Series I*, 95:65, 1805.
- [8] G. Mistura. *Multilayer growth and wetting of helium and hydrogen on alkali metals*. PhD thesis, Pennsylvania State University, 1993.
- [9] J. W. Cahn. Critical point wetting. *The Journal of Chemical Physics*, 66:3667, 1977.
- [10] R. Pandit, M. Schick, and M. Wortis. Systematics of multilayer adsorption phenomena on attractive substrates. *Phys. Rev. B*, 26:5112, 1982.
- [11] M. Kardar and J. O. Indekeu. Adsorption and wetting transitions on rough substrates. *EPL (Europhysics Letters)*, 12:161, 1990.
- [12] R. Netz and D. Andelman. Roughness-induced wetting. *Physical Review E*, 55:687, 1997.

- [13] U. Marconi, B. Marini, and F. Van Swol. Microscopic model for hysteresis and phase equilibria of fluids confined between parallel plates. *Phys. Rev. A*, 39:4109, 1989.
- [14] G. A. Darbellay and J. M. Yeomans. An interface potential approach to capillary condensation in a rectangular groove. *Journal of Physics A: Mathematical and General*, 25:4275, 1992.
- [15] Y. Xia, X.-M. Zhao, and G. M. Whitesides. Pattern transfer: Self-assembled monolayers as ultrathin resists. *Microelectronic Engineering*, 32:255, 1996.
- [16] C. M. S. Torres. *Alternative Lithography: Unleashing the Potential of Nanotechnology*. Plenum Publisher corporation, 2003.
- [17] R. D. Piner, J. Zhu, F. Xu, S. Hong, and C. A. Mirkin. Dip-pen nanolithography. *Science*, 283:661, 1999.
- [18] S. Hong and C. A. Mirkin. A nanoplotter with both parallel and serial writing capabilities. *Science*, 288:1808, 2000.
- [19] J. Brugger, J. W. Berenschot, S. Kuiper, W. Nijdam, B. Otter, and M. Elwenspoek. Resistless patterning of sub-micron structures by evaporation through nanostencils. *Microelectronic Engineering*, 53:403, 2000.
- [20] C. M. S. Torres, J. Zankovych, Sand Seekamp, A. P. Kam, C. C. Cedeño, T. Hoffmann, J. Ahopelto, F. Reuther, K. Pfeiffer, G. Bleidiessel, G. Gruetzner, M. V. Maximov, and B. Heidari. Nanoimprint lithography: an alternative nanofabrication approach. *Materials Science and Engineering C*, 23:23, 2003.
- [21] M. Hecke and W. K. Schomburg. Review on micro molding of thermoplastic polymers. *Journal of Micromechanics and Microengineering*, 14:R1, 2004.
- [22] S. Y. Chou, P. R. Krauss, and J. Renstrom. Imprint of sub-25 nm vias and trenches in polymers. *Applied Physics Letters*, 67:3114, 1995.
- [23] H. C. Scheer, H. Schulz, T. Hoffmann, and C. M. Sotomayor Torres. Problems of the nanoimprinting technique for nanometer scale pattern definition. *Journal of Vacuum Science Technology B*, 16:3917, 1998.
- [24] D. Eisert, W. Braun, S. Kuhn, J. Koeth, and A. Forchel. Metal wire definition by high resolution imprint and lift-off. *Microelectronic Engineering*, 46:179, 1999.
- [25] K. Pfeiffer, G. Bleidiessel, G. Gruetzner, H. Schulz, T. Hoffmann, H. C. Scheer, C. M. S. Torres, and J. Ahopelto. Suitability of new polymer materials with adjustable glass temperature for nano-imprinting. *Microelectronic Engineering*, 46:431, 1999.

- [26] A. Lebib, Y. Chen, J. Bourneix, F. Carcernac, E. Cambriil, L. Couraud, and H. Launois. Nanoimprint lithography for a large area pattern replication. *Microelectronic Engineering*, 46:319, 1999.
- [27] D. Y. Khang and H. H. Lee. Wafer-scale sub-micron lithography. *Applied Physics Letters*, 75:2599, 1999.
- [28] H. Schiff, R. W. Jaszewski, C. David, and J. Gobrecht. Nanostructuring of polymers and fabrication of interdigitated electrodes by hot embossing lithography. *Microelectronic Engineering*, 46:121, 1999.
- [29] B. Heidari, I. Maximov, E. L. Sarwe, and L. Montelius. Large scale nanolithography using nanoimprint lithography. *Journal of Vacuum Science Technology B*, 17:2961, 1999.
- [30] H. Schiff. Nanoimprint lithography: An old story in modern times? a review. *Journal of Vacuum Science Technology B*, 26:458, 2008.
- [31] L. J. Guo. Nanoimprint lithography: Methods and material requirements. *Advance Materials*, 19:495, 2007.
- [32] R. W. Jaszewski, H. Schiff, P. Gröning, and G. Margaritondo. Properties of thin anti-adhesive films used for the replication of microstructures in polymers. *Microelectronic Engineering*, 35:381, 1997.
- [33] R. W. Jaszewski, H Schiff, B. Schnyder, A. Schneuwly, and P. Gröning. The deposition on anti-adhesive ultra-thin teflon-like films and their interaction with polymers during hot embossing. *Applied Surface Science*, 143:301, 1999.
- [34] A. Kristensen. Nanoimprint lithography. Presentation at NordForsk summer school in Palmse, Estonia, 2007.
- [35] G.-Y Jung, Z. Li, W. Wu, Y. Chen, D. L. Olynick, S.-Y Wang, W. M. Tong, and R. S. Williams. Vapor-phase self-assembled monolayer for improved mold release in nanoimprint lithography. *Langmuir*, 21:1158, 2005.
- [36] D.-Y. Khang and H. H. Lee. Sub-100 nm patterning with an amorphous fluoropolymer mold. *Langmuir*, 20:2445, 2004.
- [37] D.Y. Khang, H. Kang, T.I. Kim, and H.H. Lee. Low-Pressure Nanoimprint Lithography. *NANO LETTERS*, 4:633, 2004.
- [38] Y. Hirai, S. Yoshida, and N. Takagi. Defect analysis in thermal nanoimprint lithography. *Journal of Vacuum Science & Technology B: Microelectronics and Nanometer Structures*, 21:2765, 2003.

- [39] M.A. Lieberman and AJ Lichtenberg. *Principles of Plasma Discharge and Materials Processing*. Wiley, New York, 1994.
- [40] A. Bogaerts, E. Neytsa, R. Gijbelsa, and J. van der Mullenb. Gas discharge plasmas and their applications. *Spectrochimica Acta Part B*, 57:609, 2001.
- [41] M.J. Madou. *Fundamentals of Microfabrication: The Science of Miniaturization*. CRC Press, 2002.
- [42] S. Jensen. *Inductively Coupled Plasma Etching for Microsystems*. PhD thesis, MIC, 2004.
- [43] H.C. Liu, Y.H. Lin, and W. Hsu. Sidewall roughness control in advanced silicon etch process. *Microsystem Technologies*, 10:29, 2003.
- [44] X. Wang, Y. Chen, L. Wang, and Z. Cui. Fabrication of nanoimprint template in Si with high etch rate by non-switch DRIE process. *Microelectronic Engineering IN PRESS*, 2008.
- [45] L. Bruschi, A. Carlin, and G. Mistura. Wetting on a geometrically structured substrate. *The Journal of Chemical Physics*, 115:6200, 2001.
- [46] A. Pozzato. Realizzazione di superfici microstrutturate mediante fotolitografia e wet etching per misure di adsorbimento di fluidi. Master's thesis, University of Padova, 2004.
- [47] R. Evans and M. B Marconi. Fluids in narrow pores: Adsorption, capillary condensation and critical points. *The Journal of Chemical Physics*, 1986.
- [48] L. W. Bruch, M. W. Cole, and E. Zaremba. *Physical Adsorption: Forces and Phenomena*. 1997.
- [49] L.H. Cohan. Sorption Hysteresis and the Vapor Pressure of Concave Surfaces. *Journal of the American Chemical Society*, 60:433, 1938.
- [50] R. Evans. Fluids adsorbed in narrow pores: phase equilibria and structure. *Journal of Physics: Condensed Matter*, 2:8989, 1990.